INFORMATION TO USERS

The most advanced technology has been used to photograph and reproduce this manuscript from the microfilm master. UMI films the text directly from the original or copy submitted. Thus, some thesis and dissertation copies are in typewriter face, while others may be from any type of computer printer.

The quality of this reproduction is dependent upon the quality of the copy submitted. Broken or indistinct print, colored or poor quality illustrations and photographs, print bleedthrough, substandard margins, and improper alignment can adversely affect reproduction.

In the unlikely event that the author did not send UMI a complete manuscript and there are missing pages, these will be noted. Also, if unauthorized copyright material had to be removed, a note will indicate the deletion.

Oversize materials (e.g., maps, drawings, charts) are reproduced by sectioning the original, beginning at the upper left-hand corner and continuing from left to right in equal sections with small overlaps. Each original is also photographed in one exposure and is included in reduced form at the back of the book. These are also available as one exposure on a standard 35mm slide or as a 17" x 23" black and white photographic print for an additional charge.

Photographs included in the original manuscript have been reproduced xerographically in this copy. Higher quality 6" x 9" black and white photographic prints are available for any photographs or illustrations appearing in this copy for an additional charge. Contact UMI directly to order.

U·M·I

University Microfilms International
A Bell & Howell Information Company
300 North Zeeb Road, Ann Arbor, MI 48106-1346 USA
313/761-4700 800/521-0600

Order Number 9000020

Studies of Cu-Al interfaces using glancing angle X-ray reflectivity and EXAFS

Chen, Huaiyu, Ph.D.

City University of New York, 1989

Copyright ©1989 by Chen, Huaiyu. All rights reserved.

U·M·I
300 N. Zeeb Rd.
Ann Arbor, MI 48106

STUDIES OF Cu-Al INTERFACES USING GLANCING ANGLE X-RAY REFLECTIVITY AND EXAFS

by

HUAIYU CHEN

A dissertation submitted to the Graduate Faculty in Physics in partial fulfillment of the requirements for the degree of Doctor of Philosophy, The City University of New York.

1989

©1989

Huaiyu Chen

All Rights Reserved

This manuscript has been read and accepted for the Graduate Faculty in Physics in satisfaction of the dissertation requirement for the degree of Doctor of Philosophy.

2/3/89	Arthur C. Damask
Date	Chair of Examining Committee
2/3/89	Joel I. Gersten
Date	Executive Officer
	Steve M. Heald
	Yi-Han Kao
	Leonard O. Roellig
	Myron Strongin
	Supervisory Committee

The City University of New York

Abstract

STUDIES OF Cu-Al INTERFACES USING GLANCING ANGLE X-RAY REFLECTIVITY AND EXAFS

by

Huaiyu Chen

Advisor: Professor A. C. Damask

Synchrotron radiation measurements using glancing angle X-ray reflectivity and fluorescence EXAFS were used to study Cu-Al thin film interfaces. The technique can detect small amounts of interfacial reaction ($\sim$ 10 to 20 Å), which conventional techniques have difficulty detecting. The reflectivity data contain information about film morphology, and the EXFAS data give atomic bond types and distances. A combination of the two sets of data provides a picture of an interface. A major effort of this thesis is to convert the glancing angle EXAFS into a quantitative tool from a qualitative one. The first step is to develop analysis routines for the reflectivity data to extract a model of the concentration profile and roughness. Then the crucial step towards the goal can be made: The correction for the anomalous dispersion effect on the EXAFS data. Results obtained from Cu-Al interfaces prepared in an UHV environment with and without exposure to oxygen before Al deposition, are compared. The reactions caused by thermal annealing at temperatures ranging from 65 to 200°C are also studied. The width of the interface region for the UHV(O) sample is estimated to be 35±25 Å as prepared, and 75±25 Å after the 140°C anneal; for the UHV sample the width is estimated to be 110±30 Å as prepared, and 175±40 Å after the 140°C anneal. Within the sensitivity of analysis, it was shown that the mixed region of both samples is not a single-phase compound, indicating the simultaneous growth of several phases. The low levels of reaction observed in this work are difficult to detect by other techniques, such as X-ray diffraction. Thus, the sensitivity of the glancing angle EXAFS technique is demonstrated and it should have many applications to other interface systems.

Acknowledgement

I wish to thank Steve Heald for being my mentor, and for monitoring closely all phases of this thesis project in the past four years, including such details as my writing and presentations. His guidance and involvement were crucial to this work as well as to my personal growth[1]. Professor Arthur Damask's concern with my education made all this possible and is greatly appreciated. I am honored to have obtained advice from Yi-Han Kao, Leonard Roellig, and Myron Strongin. I thank John Tranquada for contributing his programs and assistance, which were extremely beneficial to the early phase of this work. I enjoyed my interactions with X-11 PRT members which have broadened my horizons. I also wish to thank Bob DiNardo for preparing the HV samples, and Reed Corderman, Bob Sabatini, and Ai Hanson for their repeated help in characterizing samples. Jack Scrofani, Larry Fareria, and the technical staff in Building 480 are thanked for their kindly assistance over the years. I had valuable discussions with Mark Ruckman and Don DiMarzio, especially about the photoemission part of the work. I will remember the synchrotron trips and overnight runs with Steve, John, Gerry, Don, Mark, and Jay, as well as the pizza meetings and the good times with the people of the interface group. Alison, Mark, Jay and Dr. Woodhead read and revised my manuscripts; I appreciate their efforts very much. My special thanks go to Rulon Mayer who gave me constant encouragement, advice, and support. Professor Hua-Zhong Li is thanked for his help to me prior to and during my study in the United States. Finally, I am most grateful to my parents who prepared me for life.

This work is supported by the U. S. Department of Energy, Basic Energy Sciences, Division of Materials Sciences under contract Nos. DE-AS05-80-ER10742 and DE-AC02-76CH00016.

[1]See Appendix E.

Contents

1 INTRODUCTION **1**

1.1 Metal Bilayers And The Cu-Al Interface 2

1.2 Comparison Of Techniques For Interfacial Characterization . . . 3

1.3 Historical Development Of The Glancing Angle EXAFS Technique 5

2 THEORETICAL ASPECTS **7**

2.1 X-ray Optics, Glancing Angle Reflectivity 7

2.2 X-ray Absorption And EXAFS 12

2.3 X-ray Fluorescence 14

3 EXPERIMENTAL **18**

3.1 Measurement Of Glancing Angle EXAFS 18

3.1.1 Synchrotron Radiation Facilities 18

3.1.2 The Monochromator 19

3.1.3 Detectors and Computer Interfacing 19

3.1.4 Dimensions of the Sample 22

3.1.5 Experimental Procedures 22

3.2 Preparation Of Samples 25

3.2.1 Thermal Evaporation 27

3.2.2 Sputtering 29

3.2.3 Samples and Previous Results 29

4 **REFLECTIVITY DATA AND FITTING** **38**

4.1 Fitting Procedures 39

4.2 Discussion Of Fitting Results 47

4.2.1 As Deposited 47

4.2.2 Annealing Behavior 51

4.2.3 Comparision of Three Samples from Various Preparations 53

4.3 Estimation Of Error Bars Of Fitting Parameters 55

5 **EXAFS DATA AND ANALYSIS** **57**

5.1 Indirect Measurement of EXAFS 57

5.2 EXAFS Data 58

5.2.1 EXAFS Data from Unannealed Samples 58

5.2.2 EXAFS Data As A Function of Annealing 62

5.2.3 Standard Analysis Procedure for EXAFS 62

5.3 Anomalous Dispersion Correction (ADC) 68

5.3.1 The Anomalous Dispersion 68

5.3.2 The Correction Procedure 69

5.3.3 An Example of ADC: EXAFS from An Au Thin Film . . 71

5.3.4 ReflEXAFS 73

5.4 Quantitative Results 73

6 **STUDIES USING COMPLEMENTARY TECHNIQUES** **81**

6.1 Rutherford Backscattering Spectroscopy (RBS) 81

6.2 Transmission Electron Microscopy (TEM) 83

6.3 Auger Electron Spectroscopy (AES) 84

6.4 X-ray Photoemission Spectroscopy (XPS) 86

7 **DISCUSSION** **90**

7.1 An Average Position Of The Interface 90

7.2 Errors Caused By Various Factors 94
7.2.1 Consideration of GB Cu-Al Bonds 96
7.2.2 Consideration of Large-Angle Scattering 96
7.2.3 Consideration of The Validity of The Single-Bond Assumption 98
7.2.4 Consideration of Deviation in Density Profile 101
7.2.5 A Corrected Interface Location 104
7.3 Growth Kinetics, Oxygen Effect, And A Picture Of Cu-Al Interfaces 109
7.3.1 The UHV Sample 109
7.3.2 The UHV(O) Sample. Difference in Grain Sizes? 112
7.3.3 More Comparison on Annealings 114
7.3.4 Bond Lengths, Phases 114

8 SUMMARY **117**

A PROGRAMMING NOTES **122**
A.1 SUM and AX: Estimation Of The Interface Locations 122
A.2 FITING2: A Fitting Routine For Reflectivity Data 123
A.3 FLCORR: Corrections To Ion Chamber Response 124
A.4 FLUCOR: Manipulating UW binary data files in XMU format . 125
A.5 COR: ADC procedures 125
A.6 CALLFLU 129
A.7 IDPLIS 130

B SOME CALCULATIONS **131**
B.1 Notes From James: Model For X-ray Absorptions 131
B.2 Calculations Of X-ray Reflectivity For Multilayers 134
B.3 Calculations Of X-ray Fluorescence For A Thin Film 134

C DATA ANALYSIS PROCEDURES **136**

C.1 Procedures For EXAFS Data Analysis 136

C.2 Procedures For Reflectivity Data Analysis 137

D ANALYSIS OF REFLECTIVITY EXAFS **141**

E A STORY **143**

Bibliography **144**

List of Figures

2.1 (a) Calculated reflectivity vs the incident angle on 1000 Å Al/Cu. (b) Calculated X-ray intensity vs depth at the angle indicated by an arrow in (a). 9

2.2 The model for calculating the reflectivity of a multilayer. 10

2.3 The fluorescence signal from a thin film. 16

3.1 Glancing angle experiment setup: The sample stage (shaded area, see bottom drawing for details) is controlled by a stepping motor. A: Sample holder. B: Flexial pivots. C: Adjusting screws. D: Micrometer and PZT. E: Couple between the motor shaft and the micrometer. F: Motor. 20

3.2 Fraction of the beam absorbed by He, N_2, Ar, and Kr in a six-inch ($\sim$ 15 cm) chamber. $\mu(E)$ is the absorption coefficient at E, the beam energy, and $l = 15$ cm. 21

3.3 Exposure of the reflected X-ray beam (top) and the direct beam (bottom) for angle calibrization 24

3.4 EXAFS scans without (dashed line) and with (solid line) the angle correction. Note the elimination of the background. 26

3.5 The UHV chamber for evaporation. A: Rotary for the sample holder. B: Thermocouple. C: Viewport (also for mounting/dismounting samples). D: Rate monitor. E: RGA head. F: Leak valve. G,I: Evaporator leads. H: Venting valve. J: Valve to ion pumps. K: Liquid nitrogen for TSP. L: TSP. M: Ion pump. . 28

3.6 TEM pictures of (a) the HV-evaporated sample, with different time of exposure emphasizing the Cu layer (left) and the Al layer (right), and (b) the sputtered sample. The Cu-Al interfaces are marked by arrows. Difference in grain size and the sharpness of the interface are shown. 30

3.7 Comparison of the reflectivity data obtained from the HV-evaporated sample and from the sputtered sample 32

3.8 Comparison of the EXAFS data obtained from the HV-evaporated sample and from the sputtered sample 33

3.9 The arrangement of the evaporators. 36

4.1 First step of fitting: Reflectivity as a function of angle, at a shorter range. 41

4.2 Reflectivity as a function of angle, at various annealing temperatures for the UHV sample. Lines: data, points: fitting. 43

4.3 Construction of the Cu concentration profile. Dashed lines: Densities following a Complementary Error Fuction for each interface; Solid line: The overall density. 45

4.4 Models from fitting: Cu concentration depth profile. From left to right: HV, UHV(O), UHV. 46

4.5 Reflectivity as a function of the X-ray energy: a: Data taken at 2.5mrad on sample UHV annealed at 120 degrees; b: Calculation assuming only GB Cu contributes; c: Calculation assuming a thin surface Cu layer in addition to GB Cu. 48

4.6 Illustration of estimation of the grain size. 50

4.7 Arrhenieus plot of the interface growth on the HV, UHV(O), and the UHV samples. 52

5.1 Reflectivity as a fucntion of the incident angle, from the UHV sample after annealing at 120°C. V1, P1 and P2 are the angles at which EXAFS was measured. 59

5.2 Model calculation of the fluorescence as a function of the depth into the sample (b), based on the model from the fitting to the reflectivity (a). 60

5.3 EXAFS from the UHV and UHV(O) samples as deposited, compared to the Cu and $CuAl_2$ standards 61

5.4 EXAFS taken at angle V1 from the UHV and UHV(O) samples, at various anneals. 63

5.5 EXAFS taken at angle P1 from the UHV and UHV(O) samples, at various anneals. 64

5.6 EXAFS taken at angle P2 from the UHV and UHV(O) samples, at various anneals. 65

5.7 Standard EXAFS analysis procedure: (1) Raw data, (2) Background subtracted and converted to k-space, (3) Fourier-transformed, and (4) Backtransformed first shell data. From Reference [52]. . 66

5.8 fluoEXAFS from a Au thin film, before (solid line, smaller amplitude) and after (solid line, larger amplitude) ADC, compared to the standard from a transmission measurement of an Au foil (dashed line). 72

5.9 Examples of Al/Cu UHV(O) sample first shell data (unannealed) at V1 before and after the ADC. 74

5.10 EXCURVE fitting results of the data shown in the previous figure. Solid line: data, dashed line: fitting. 75

5.11 EXCURVE fitting results of the data, UHV(O) 120 degrees annealed, at angle V1 76

5.12 EXCURVE fitting results of the data, UHV(O) 120 degrees annealed, at angle P1 77

5.13 EXCURVE fitting results of the data, UHV(O) 120 degrees annealed, at angle P2 78

6.1 RBS on UHV unannealed sample 82

6.2 AES on HV sample 85

6.3 XPS data for the Al/Cu and Al/O/Cu valence bands as a function of Al evaporation time 87

6.4 XPS data for the Al/Cu and Al/O/Cu core levels 88

7.1 Areas on either side of the interface location, based on model calculations discussed in Chapter 5 91

7.2 Movement of the interface as a function of anneals. 95

7.3 Change of the interface location due to the exsistence of the other type of bond. (a): Effects of the relative amount of the other type of bond, (b): effects of different incident angles. 100

7.4 Change of the areas due to the deviation in the model of the density profile 102

7.5 Movement of the interface as a function of anneals for the UHV sample, considering the GB effect. 106

7.6 Movement of the interface as a function of anneals for the UHV(O) sample, considering the GB effect 107

7.7 Movement of the interface as a function of anneals, considering GB effect and varying the Al/Cu-Al boundary as temperature increases 108

7.8 A sketch describing the kinetics of interface reation for the (a) UHV and (b) UHV(O) sample. In (b), smaller grains near the interface join to make larger grains towards the surface. 110

7.9 A-, B-, and C-type of GB diffusion model, based on reference [45]. 111

List of Tables

4.1 Model fitting results of the reflectivity as a function of the annealing temperature for the UHV sample. D is the thickness, ρ the relative density, σ the roughness, ϕ the correction for the incident angle, and n the normalization. 44

4.2 Estimated errors of the fitting parameters. 56

5.1 Fitting results of the EXAFS first shell data 79

7.1 Location of the interface at various anneals obtained from the EXAFS ratio at angle V1, P1, and P2. 93

7.2 Location of the interface at various anneals obtained from the EXAFS ratio at angle V1, P1, and P2, considering the GB effect 105

7.3 Bond lengths of stadard compounds between Cu and Al 115

Chapter 1

INTRODUCTION

This thesis applies a new technique for interface studies, namely, the glancing angle X-ray reflectivity and fluorescence Extended X-ray Absorption Fine Structure (the glancing angle EXAFS, for short). The glancing angle EXAFS technique is used to investigate Cu-Al thin film interfaces. This technique is sensitive to interfacial reactions in a small region ($\sim$ 30 Å) and can provide structural information about the region. Some unique features of the reaction at Cu-Al interfaces were observed, which might lead to an improved understanding of the mechanisms controlling interfacial reactions.

This thesis begins with an introductory chapter discussing earlier investigations of the Cu-Al interface, and proceeds as follows:

Ch2: Theorectical aspects of the glancing angle EXAFS technique

Ch3: Technical and experimental details of the technique

Ch4: Reflectivity studies on various Cu-Al thin film interfaces

Ch5: EXAFS data analysis for a buried Cu-Al interface, and a discussion of the anomalous dispersion effect on the data

Ch6: Comparison of the results with those of other techniques

Ch7: Discussion of the physical significance of the results and speculation on the mechanisms for the reaction at the Cu-Al interface

Ch8 Summary and conclusions

1.1 Metal Bilayers And The Cu-Al Interface

In this study, an interface refers to the boundary between two thin films, of the order of 100 to 1000 Å thick. Films below (ultra-thin films) and above (thick films) this order of thickness are not of the main concern of this thesis, but will be mentioned when relevant.

Interfacial reactions are of interest to both pure and applied sciences. As more and more techniques for thin film fabrication are discovered, the industrial application of thin film technology and the scientific research on interfaces are becoming mutually beneficial. The understanding of interface reactions plays an important role in practical applications, ranging from traditional anti-corrosion coatings to modern electronic devices. From the scientific point of view, thin films may have different mechanical, structural, and thermodynamic properties from bulk materials. For example, for most bulk materials, intermetallic compounds predicted by phase diagrams have been observed. However, in thin films, all the phases predicted by the phase diagram may not exist at the same time. Usually one phase dominates the compound growth and then switch over to the next phase [1]. It is even possible to have a phase that is not predicted by the phase diagram and not observed in bulk materials. Questions like these have made studies of interface studies interesting and exciting.

Al-Cu is one of the alloy systems that have been well studied in the bulk form. Reactions caused by thermal treatments (such as solidification and quench hardening) have been extensively examined [2]. For example, the precipitating behavior of dilute Cu in Al has been studied: The reaction starts with a solid

solution, goes through three metastable phases (GP I, GP II, and θ') and finally reaches an equilibrium phase, $CuAl_2$ (θ phase). Descriptions like this can not always be given for a thin film system. Interface reactions occur mainly through interdiffusion, which is affected by factors such as the quality of the film and thermal conditions. So far phase diagrams can not adequately predict film reactions, because of the complexity of the interfaces, and the need for tools with high depth resolution to probe a very confined region where the initial phases exist. Several authors have studied Cu-Al thin films, particularly the kinetics of interface reactions after the first 200Å of compound formation (e.g., [3]-[5]). They agree that at later stages of the reaction, the growing phases at a thin film interface proceed predominately one at a time. The new phase grows as the old one shrinks. There are disagreements on the initial stage – whether θ-$CuAl_2$ is the first phase at the interface, or whether it is one of the several simultaneously growing phases. Whether there are intermediate phases below this scale is unknown. It is desirable, therefore, to introduce a new tool with higher sensitivity than the conventional ones.

1.2 Comparison Of Techniques For Interfacial Characterization

Most studies on interfaces have used by one or more of the following techniques: Transmission Electron Micrograph (TEM), Glancing Angle X-ray Diffraction (GXD), Auger Electron Spectroscopy (AES), and Rutherford Backscattering Spectroscopy (RBS). Each technique can provide compositional or structural information on a certain scale [6]. TEM has very good resolution (atomic layers), and it would be ideal for studying film qualities. The major difficulty in using TEM is the preparation of the sample. The preparation often requires mechanical milling and heating, which may cause uncalibrated modification of the

interface. In addition, although TEM is capable of making electron diffraction measurements, interfaces do not always have sufficiently ordered structures to permit examination at atomic level. A similar argument can be made for GXD, which suffers from the experimental difficulty of collecting weak signals. AES is a reliable tool for surface studies, but is less reliable for studies of buried interfaces, which require depth profiling with ion-beam sputtering. The sputtering ion-beam can carry atoms from the surface to the bulk, which seriously reduces the precision in determining compositions. The typical depth resolution of RBS is $\sim$ 200 Å, insufficient for detailed interface analysis. In spite of their deficiencies, all these techniques (except GXD) were used to characterize and compare some of the samples in this study. The results are discussed in more detail in Chapter 6.

Although GXD is difficult to use for disordered interfaces, the idea of using glancing angle X rays is attractive. A probe with good penetrating ability is essential for studying buried interfaces. An X-ray beam can penetrate samples without damaging them, which makes it superior to many other existing probes. With the rapid development of synchrotron radiation sources in recent years, X-ray sources with higher intensity and flexibility have become more accessible. Their most obvious advantage is a tremendous increase in the speed of data collection compared to using conventional X-ray sources. Synchrotron radiation also has helped the development of new approaches. One such new approach is described in this thesis – the glancing angle X-ray reflectivity and fluorescence yield measurements EXAFS (glancing angle EXAFS for short) – for interface studies. Unlike GXD, this technique does not require long-range order in the sample. It can be applied to solid-solid, solid-liquid, and solid-gas interfaces.

1.3 Historical Development Of The Glancing Angle EXAFS Technique

In 1954, Parratt pointed out that glancing angle X-ray techniques could be employed for surface and interface studies [7]. Since then, there have been numerous experiments using such techniques. Measurements involved specular reflectivity, scattering, diffraction, fluorescence, *etc.* (see, e.g. [8]-[15]). In some studies, the reflectivity data is measured over a large angle range (a few degrees) above the critical angle (the angle below which the total external reflection occurs) of the material, and the considerable changes in the intensities of the reflected beam require that the detector has a large dynamic range ($10^5 - 10^7$). By doing a Fourier transform of the reflectivity spectrum, the reflectivity data can be convoluted to extract the composition profile of thin films with one or two simple interfaces [16,17]. In the present work, the samples are bimetallic thin films deposited on substrate. The interfaces are more diffused and more complicated. High level of roughness would fail the Fourier trasform method. The reflectivity measurements in this work were taken at a smaller angle range is smaller (just above the critical angle). The X-ray signals can be detected in air, and less expensive ionization chambers can be used as a detector. A least-square fitting is developed to analyze the reflectivity data. The fitted parameters can be constructed to reveal the composition profile around the studied interface without the need for solving irrelevant ones (such as the interface of the substrate).

The composition information provided by the reflectivity data does not contain structural information at atomic level. One usually needs a complementary technique that provides such information. EXAFS is chosen for this study because of its sensitivity to the local atomic environment. Experimental evidence for EXAFS was presented in the 1940's, and its theory was developed even earlier (see [18]-[20] for further details). After almost 50 years of debating whether

long- or short-range order theory should be used, the argument was put to rest by Stern *et al.* in 1972 who explained the EXAFS phenomenon with a short-range order theory, and developed the well-known Fourier transformation technique for data analysis [21]. Their work not only ended the theoretical confusion, but, along with the development of synchrotron radiation, made EXAFS a powerful experimental tool for material studies.

Conventional EXAFS data is obtained by measuring the absorption coefficient in a transmission mode. Regarding the interface problem, the EXAFS in this work can be measured from the reflectivity or fluorescence yield. There has been much work using these schemes (e.g. [23]-[28]), most of which using reflectivity to obtain EXAFS. Fluorescence is used in this work. On systems with dilute concentrations of the absorbing element, data analysis is straight forward [22,30]. Dilute systems can also refer to monolayers of the absorbing atoms on the surface (such as those studied by SEXAFS [29]) or at the interface, or to a dilute concentration of atoms throughout the whole sample (such as biological and electrochemical samples in solution [31,32]). On concentrated systems, such as metal-metal interfaces, where one of the species studied is in a bulk form, qualitative EXAFS studies also have been carried out (e.g. [33]). However, quantitative analysis has not been made due to the complications caused by the anomalous dispersion effect. There have been suggestions for solving the anomalous dispersion problem by doing a Kramer-Kronig analysis [34,35]. This work suggests that a simpler approach may successfully attack the problem. Once a satisfactory solution is found, the glancing angle EXAFS data can be analyzed at a quantitative level to provide more detailed information on interfaces.

Chapter 2

THEORETICAL ASPECTS

The glancing angle EXAFS technique is based on three main concepts: (1) X-ray optics at glancing angles (total external reflection), (2) X-ray absorption and EXAFS, and (3) correlation of X-ray absorption to the fluorescence yield.

2.1 X-ray Optics, Glancing Angle Reflectivity

In the X-ray energy range, the index of refraction, r, which describes the interaction between matter and X rays, can be written as:

$$r = 1 - \delta - i\beta \tag{2.1}$$

where δ and β are small positive numbers [Appendix B]. According to Snell's law, X rays do not penetrate a surface when the incident angle θ (angle between the beam and the surface) is less than the critical angle, $\theta_c = (2\delta)^{1/2}$. In other words, the X rays are totally reflected from the surface except for an evanescent wave that travels along the surface. Since θ_c is proportional to the density of the matter, one way to study an interface is to put the lighter material above the heavier one. In this case, when $\theta_c(\text{top}) < \theta < \theta_c(\text{bottom})$, the X rays penetrate through the top layer, yet are totally reflected from the bottom layer. The X-ray intensity inside the bottom layer decays exponentially and reaches $1/e$ of the surface intensity at about ~ 30 Å below the surface.

Figures 2.1a and b illustrate a model calculation of the reflectivity and the penetration depth of X rays in a bilayer. The model consists of 1000 Å Al on Cu. The oscillations are due to the interference between the reflected and the incoming X rays, which causes standingwave-like patterns within the overlayer. The amplitude and the phase of the reflected beam are the result of such interference at the surface of the layers. When the incident angle varies, the length of the X-ray path also varies, as if the thickness of the layer changes. Consequently, sinusoidal oscillations occur (see Appendix B for details).

Considerations of self consistency are necessary when calculating the reflectivity from each interface. One can do a recursive calculation [7] or a matrix calcultation [36]. Figure 2.2 explains the notation used in the following discussion.

The reflectivity is the ratio of the reflected to the incident electric field intensity. The measured reflectivity is the result of the reflections from all the interfaces. Boundary conditions relate the normal and tangential components of the electric fields and give a recursive relation for the interface between layer n and $n+1$:

$$R_{n-1,n} = a_{n-1}^4 \frac{R_{n,n+1} + F_{n-1,n}}{R_{n,n+1} F_{n-1,n} + 1} \tag{2.2}$$

where,

$$R_{n,n+1} = a_n^2 (E_n^R / E_n)$$

$$F_{n-1,n} = \frac{f_{n-1} - f_n}{f_{n-1} + f_n}$$

and,

$$a_n = e^{-i f_n d_n / 2}$$

$$f_n = k_0 \sqrt{r_n^2 - cos^2\theta}$$

In the above expressions, n stands for the index of the layers, E_n the electric field of the X-ray beam in layer n, θ the incident angle and k_0 the wave vector

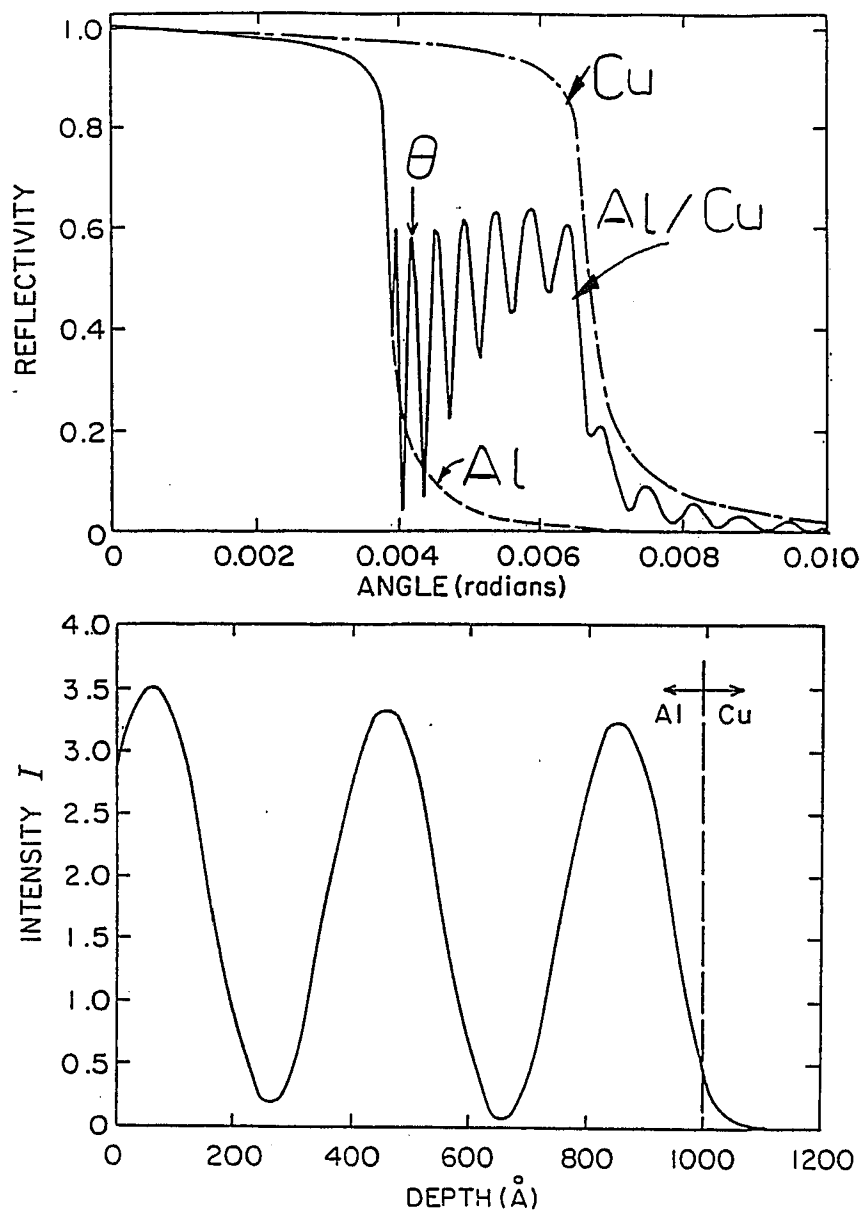

Figure 2.1: (a) Calculated reflectivity vs the incident angle on 1000 Å Al/Cu. (b) Calculated X-ray intensity vs depth at the angle indicated by an arrow in (a).

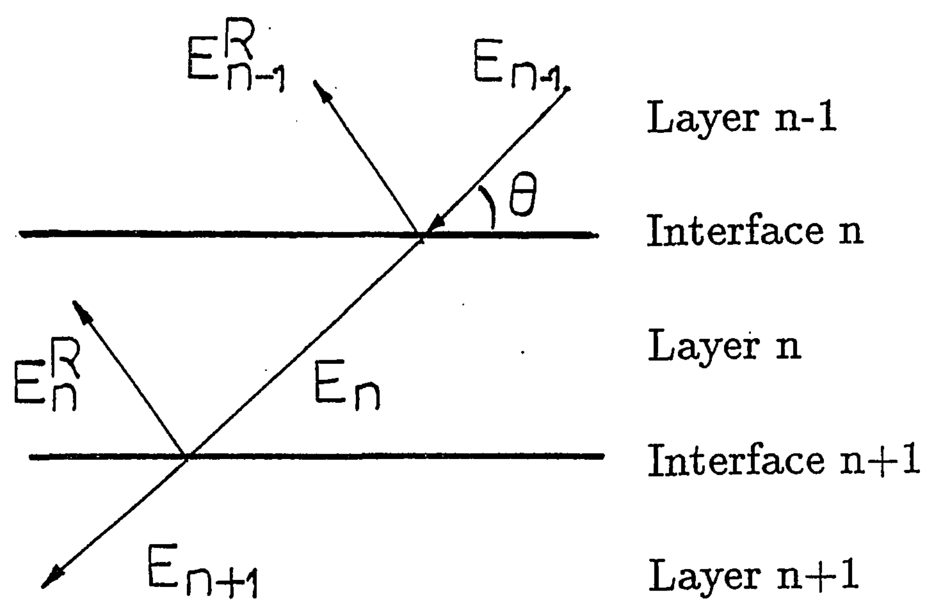

Figure 2.2: The model for calculating the reflectivity of a multilayer.

of the X rays in vacuum. Let N be the bottom layer and 1 be the vacuum, a given calculation starts at the bottom interface (between layer $N-1$ and N), assuming the thickness of the layer N is infinite (therefore no reflection at this interface, namely, $R_{N-1,N}=0$). Working upward from layer N (reducing n), the total reflectivity can be evaluated as:

$$\mathrm{R} = | R_{1,2} |^2 = | E_1^R / E_1 |^2 \tag{2.3}$$

Matrix calculations are based on the same principle, but are carried out more conveniently when it is necessary to add roughness to each interface rather than assuming a sharp one. Assuming that the roughness can be modeled by a random distribution (following a Guassian shape) of the density around the average interface postition, the roughness at each interface can be included in the reflection matrix R_n. Using the same notation as in Equation 2.2:

$$\begin{pmatrix} E_1 \\ E_1^R \end{pmatrix} = \mathrm{M} \begin{pmatrix} E_n \\ E_n^R \end{pmatrix} \tag{2.4}$$

where M is a product of a series of matrices:

$$\mathrm{M} = \mathrm{T}_1\mathrm{R}_1\mathrm{T}_2\mathrm{R}_2 \ldots \mathrm{R}_{n-2}\mathrm{T}_{n-1}\mathrm{R}_{n-1}$$

where T_n is the transmission matrix and R_n the reflection matrix. T_n and R_n are written as:

$$\mathrm{T}_n = \begin{pmatrix} a_n^{-2} & 0 \\ 0 & a_n^2 \end{pmatrix}$$

$$\mathrm{R}_n = \begin{pmatrix} b_n & b_n^R \\ b_n^R & b_n \end{pmatrix}$$

in which,

$$b_n = \frac{1}{2}\left(1 + \frac{f_{n+1}}{f_n}\right) e^{-(f_n - f_{n+1})^2 \frac{\sigma_n^2}{2}}$$

$$b_n^R = \frac{1}{2}\left(1 - \frac{f_{n+1}}{f_n}\right) e^{-(f_n + f_{n+1})^2 \frac{\sigma_n^2}{2}}$$

where σ_n is the RMS deviation of the interface from its average position. The total reflectivity can be calculated similarily from Equation 2.3.

The roughness evaluation can also be included in the recursion equation. Hence, these two methods produce identical results and a choice depends upon the programer's preference.

2.2 X-ray Absorption And EXAFS

When an X-ray photon of energy E strikes an atom, it excites an inner core electron (core level energy E_k) when $E > E_k$. The photon is then absorbed and the electron is ejected. The absorption process can be described as a transition of the absorbing atom from the initial to the final atomic state, due to the dipole coupling (to the first degree of approximation) between the electrons and the X rays. The absorption coefficient μ, which is proportional to the transition probability, is given by Fermi's Golden rule:

$$\mu \propto |< \text{initial state} \mid H \mid \text{final state} >|^2 \rho(E_f) \tag{2.5}$$

where H is the dipole potential in the external field, and $\rho(E_f)$ is the density of the final state. The initial and the final states can be written further as:

$$\text{initial state} = \psi_{i,atom}\psi_{i,core}$$

$$\text{final state} = \psi_{f,atom}\psi_{f,k}$$

where $\psi_{i,atom}$ and $\psi_{f,atom}$ stand for the wavefunctions for the atom with a core hole before and after the excitation, respectively. $\psi_{i,core}$ is the wavefunction for the localized electron before ejection, and $\psi_{f,k}$ is its wavefunction after ejection. By using the "sudden approximation", (namely, $\psi_{i,atom} = \psi_{f,atom}$) Equation 2.5 can be reduced to:

$$\mu \propto |< \psi_{i,core} \mid H \mid \psi_{f,k} >|^2 \rho(E_f) \tag{2.6}$$

where,

$$\psi_{f,k} = \begin{cases} \psi_k & \text{(monoatomic system)} \\ \psi_k + \psi_k^{sc} & \text{(otherwise)} \end{cases}$$

ψ_k describes the outgoing electron wave and ψ_k^{sc} describes the backscattered electron wave from the surrounding atoms. Both ψ_k^{sc} and ψ_k contain an e^{ikR} factor for the propagating plane wave. The square of the complex conjugate in Equation 2.6 contains a cross term:

$$< \psi_{i,core} \mid \mathrm{H} \mid \psi_k >< \psi_{i,core} \mid \mathrm{H} \mid \psi_k^{sc} >$$

which retains the e^{ikR} factor after the integral. This factor gives rise to oscillations in μ. It can be further understood by the following statements:

(1) the interference between ψ_k and ψ_k^{sc} causes constructive and destructive patterns in real space,

(2) the wavefunction $\psi_{i,core}$ is localized to the core region, and thus the overlapping of $\psi_{i,core}$ with the resulting wave of $\psi_k + \psi_k^{sc}$ near the core determines the transition probability, and

(3) the change of the photon energy (which, in turn, changes the electron wavelength) is analogous to a change of the observation point in space.

Therefore oscillations are expected. The oscillations in μ are known as the Extended X-ray Absorption Fine Structure, or EXAFS. The word "Extended" refers to the fact that the energy range is sufficiently far away from an absorption edge E_k (e.g. 40 electron volts above it), where the sudden approximation is valid and $\rho(E_f)$ should be featureless. Near-edge structures need a more complicated theoretical explanation, which is beyond the scope of this work. In a recent development, the International Conference on XAFS (**XAFS V, August 1988, Seattle, WA, USA**) felt that it was no longer necessary to emphasize the limit and E was dropped.

If we define EXAFS, oscillations in μ, as:

$$\chi(E) = \frac{\mu - \mu_0}{\mu_0} \tag{2.7}$$

where μ_0 is the smooth background of μ, and E the X-ray energy. Using the plane wave approximation and neglecting multiple scattering, Equation 2.6 leads to a simplified form of the EXAFS signal:

$$\chi(k) = \sum_j \frac{A_j(k)N_j}{R_j^2} e^{-2\sigma_j^2 k^2} sin(2kR_j + \phi_j(k)) \tag{2.8}$$

where k is the photoelectron wave vector ($k = \sqrt{2m_e(E - E_k)}/h$), $A(k)$ is an amplitude function which depends on the type of neighbor, R is the distance between the excited atom and its neighbors, N_j is the number of type j atoms at the distance R_j (shell j), and σ^2 is the mean squared variation of R. The functions $A(k)$ and $\phi(k)$ are usually determined with standard materials, allowing the structural parameters to be isolated. Each shell of atoms generates a particular frequency of oscillation, which, for well-separated shells can be distinguished by Fourier transform techniques. In more complex cases, as are encountered in this work, fitting procedures can be used to separate the contributions from the nearest neighbor shells. $A(k)$ and $\phi(k)$ have a k-dependence according to the atomic number Z, and this convenient feature can be used to separate the contributions from different types of neighbors. Since EXAFS is a local probe, long-range order is not required, and the technique is well suited for studying thin interface regions which may have considerable compositional or structural disorder.

The procedure for EXAFS data analysis is discussed further in Chapter 5 and Appendix C.

2.3 X-ray Fluorescence

When the inner shell electron is ejected, a core hole is created and is soon filled by an outer shell electron to lower the excitation state. The extra energy is released in the form of a fluorescent photon. The probability of creating a

fluorescent photon is proportional to the absorption coefficient, μ, and to other more complicated functions which are nearly independent of the energy of the incident photons. The fluorescent signal also contains EXAFS. Experimentally, it is sometimes convenient or necessary to obtain EXAFS by such an indirect measurement.

The overall X-ray fluorescence from a slab of sample (see Fig 2.3 and Appendix B for the derivation) is:

$$I_f = I_s \frac{\mu_a}{\mu_t}(1 - e^{-\mu_t d}) \tag{2.9}$$

where $\mu_a = \mu_A/sin\theta$, and μ_A denotes the absorption of the primary X rays by only the species under study, $\mu_t = \mu_a + \mu_b + \mu_f$ is the absorption of the primary and fluorescence X rays by all elements in the sample where $\mu_b = \mu_B/sin\theta$, μ_B describes absorptions due to all elements but the species under study, $\mu_f = \mu_F/sin\phi$, the absoption to the fluorescence exiting at angle ϕ, I_s is the surface intensity.

Equation 2.9 can be simplified for two limits:

A. Thin samples: When

$$\mu_t d \ll 1,$$

$$1 - e^{-\mu_t d} \simeq \mu_t d,$$

$$I_f = I_s \mu_a d \tag{2.10}$$

In this limit the linear relation between the fluorescence I_f and μ means that the extraction of EXAFS data is straight forward. Previous work by Heald *et. al.* [22] is a good example of the application of this limit.

B. Thick samples: When

$$\mu_t d \gg 1,$$

$$1 - e^{-\mu_t d} \simeq 1,$$

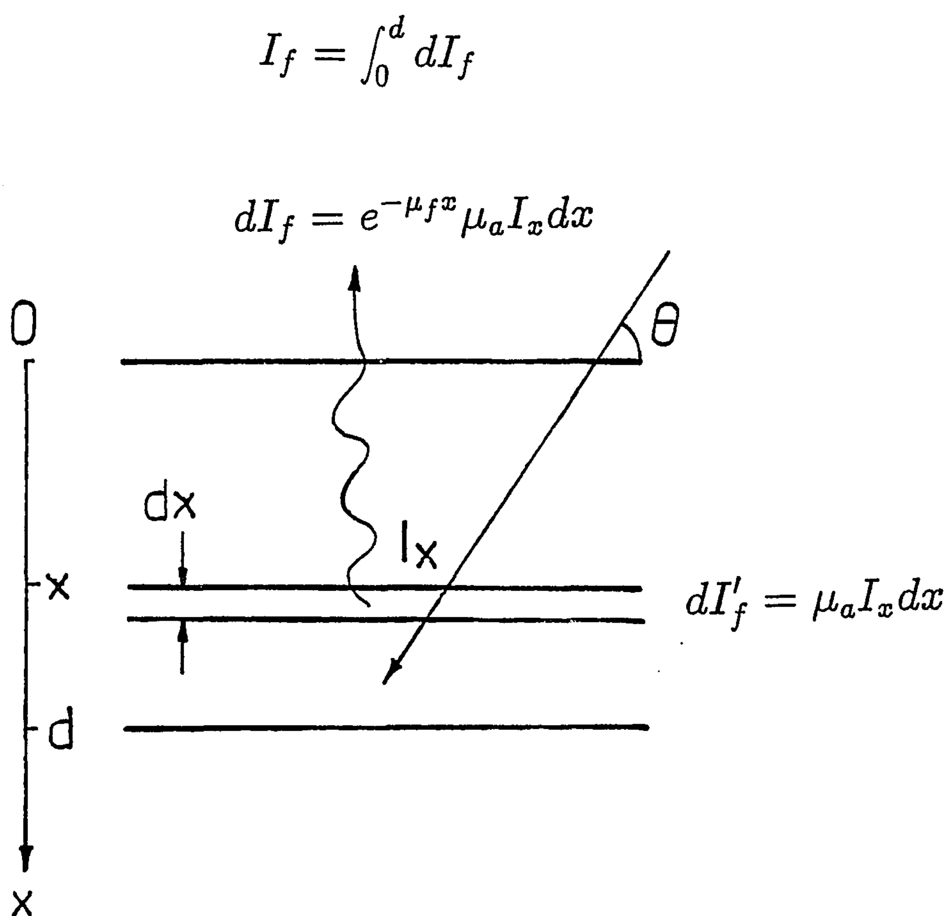

Figure 2.3: The fluorescence signal from a thin film.

$$I_f = I_o \frac{\mu_a}{\mu_t} \tag{2.11}$$

In a special case when the absorbing species is dilute (i.e. $\mu_a \ll \mu_t$), and changes in μ_a do not affect μ_t, μ_t can then be treated as a constant. This situation is essentially the same as in case (1), the thin sample limit. For the concentrated case, however, μ_a and μ_t are comparable in magnitude. The oscillations in I_f are reduced by a cancellation between μ_t and μ_a. This effect must be considered when extracting EXAFS from such a system.

Quite often the sample is between these two limits and Equation 2.9 must be used without simplification to calculate X-ray fluorescence.

Chapter 3

EXPERIMENTAL

This chapter describes the experimental equipment, procedures, and the preparation of the samples.

3.1 Measurement Of Glancing Angle EXAFS

3.1.1 Synchrotron Radiation Facilities

The X-ray experiments for this work were done on the synchrotron radiation facilities at the National Synchrotron Light Source (NSLS), Cornell High Energy Synchrotron Source (CHESS), and Stanford Synchrotron Radiation Laboratories (SSRL). A typical synchrotron facility consists of an orbital ring where electrons are accelerated. Beamlines are tangential to the electron orbit because synchrotron radiation is emitted tangentially when electrons are accelerated around a curved orbit. A beamline has a monochromator for energy selection and X-ray optics. The experimental station is located inside a radiation-shielded area (hutch) at the end of the beam line.

Synchrotron beamlines have different designs, according to the interest of the designer. Beamline X-11A, designed by Steve Heald [37] at the NSLS of Brookhaven National Laboratory, used in this work illustrates the typical features of X-ray beamlines designed for X-ray absorption experiments.

3.1.2 The Monochromator

The X-11A monochromator tank has four crystals; in this work, only the two-crystal scheme was used. The two crystals are mounted parallel to each other on a Huber goniometer. Both crystals rotate, and the second crystal has translational freedom. The energy is selected by the Bragg Diffraction condition. For the energy range of 3.5-22 kev, Si(111) crystals are used. The energy resolution (ΔE/E) is $\sim 2 \times 10^{-4}$. The full beam size is $\sim$ 10 x 0.5 millimeters. A typical photon flux is $\sim 1 \times 10^{10}$ photons/second at 10 keV with 100 mA current in the ring (see [38] for more information).

3.1.3 Detectors and Computer Interfacing

The design of the glancing angle experiment is shown in Fig. 3.1. Gas ionization chambers are used as photon detectors. The incident beam is monitored by the I_0 chamber (6 inch long), which absorbs $\sim$ 10% of the full beam. Pure nitrogen (or 90% N_2 + 10% Ar) is suitable for the energy around 10 keV. The reflected beam is monitored by the I_r chamber (6 or 12 inches long), which should have 90% absorption by using pure Ar (or a mixture of Ar and N_2) in the chamber. Fig. 3.2 shows the percentage of absorption by different gases as a function of energy. This chart can be used to determine what type of gas mixture should be selected for the ionization chambers.

A Stern-Heald chamber is used as the fluorescence detector I_f [39]. Pure Kr gas is used for Cu edge. The I_0 and I_r chambers are each biased by a 300 V DC power supply. The I_f chamber is biased by a 67.5 V battery. The output signal from each chamber goes into a Keithly current amplifier (with gains from 10^7 to 10^{10}), then into a voltage-frequency converter. The signals are integrated for $\simeq$ 2 sec/point. The output goes to the CAMAC Crate (which consists of a real-time clock, a hex scaler and a crate controller) for displaying and recording

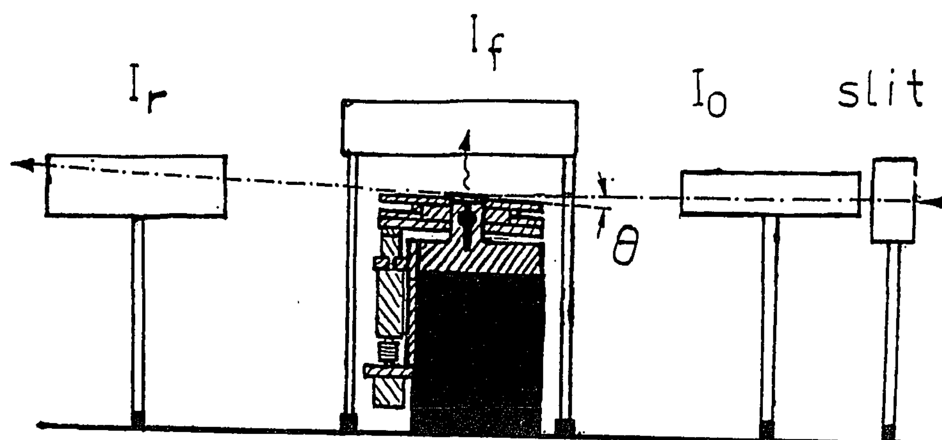

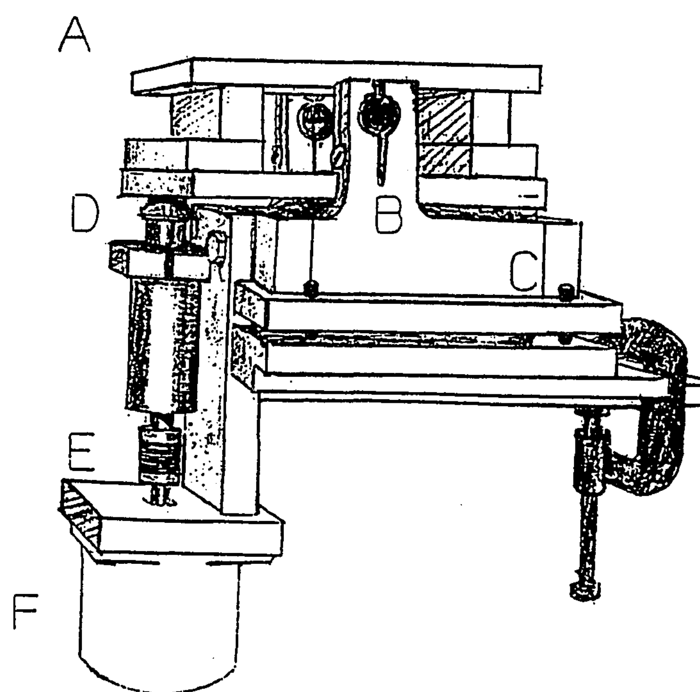

Figure 3.1: Glancing angle experiment setup: The sample stage (shaded area, see bottom drawing for details) is controlled by a stepping motor. A: Sample holder. B: Flexial pivots. C: Adjusting screws. D: Micrometer and PZT. E: Couple between the motor shaft and the micrometer. F: Motor.

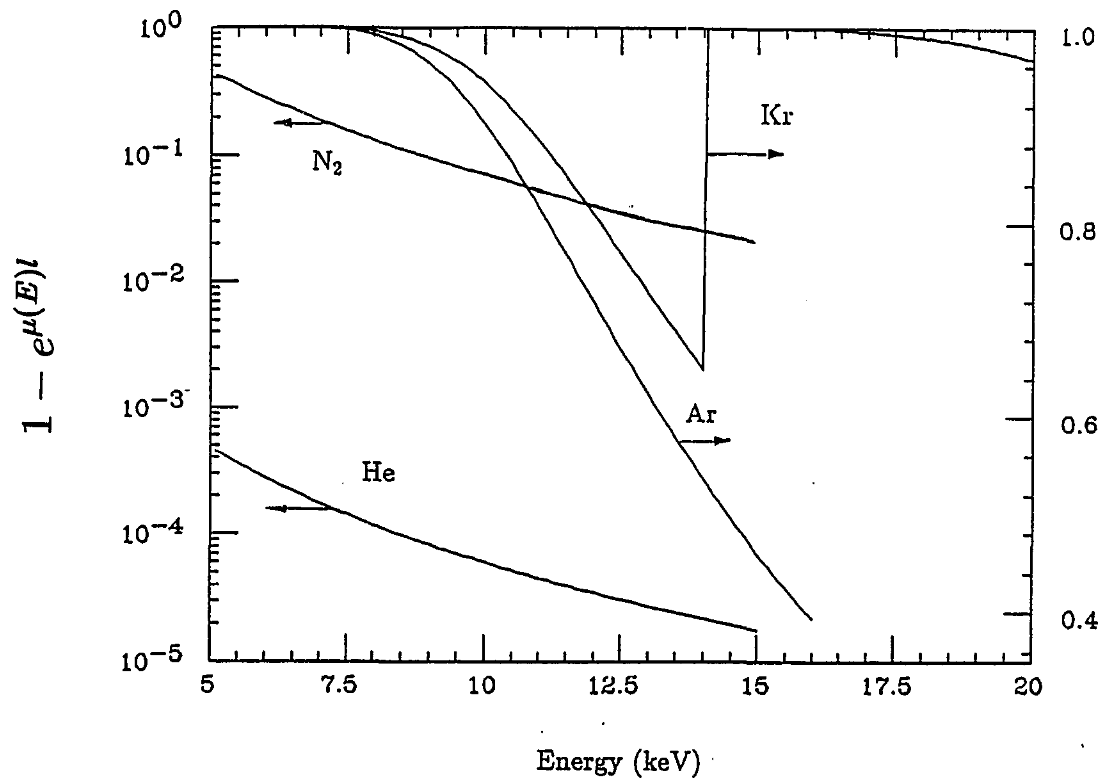

Figure 3.2: Fraction of the beam absorbed by He, N_2, Ar, and Kr in a six-inch ($\sim$ 15 cm) chamber. $\mu(E)$ is the absorption coefficient at E, the beam energy, and $l = 15$ cm.

the data.

The DEC PDP-11/34 computer, running the RSX-11M operating system, is used for interfacing with a motor controller unit, which sends pulses to the motors. Data acquisition software allows various types of scans, such as an energy scan (scanning the monochromator crystal) or a stepping motor scan, or both.

3.1.4 Dimensions of the Sample

Glancing angle experiments require samples with a sufficiently large surface area so that the beam does not "spill over" the sample edge. At an incident angle θ =0, the beam just grazes across the surface. As θ increases, a larger and larger portion of the beam is blocked by the sample until the whole beam is intercepted. The beam spreads across an area of d/sinθ when making contact with the sample surface, d being the vertical beam size which is limited by the vertical slits. To obtain the true value of the total reflection (the "flat top" on the reflection curve), it is desirable to have the whole beam fall onto the surface area before the critical angle is reached. For example, θ_c of Alumimum is ~4 mrad at 9 keV. The length of the sample should be greater than d/sin(4×10^{-3}). The full beam size is ~0.5 millimeter, and a feasible slit size is ~1/10 of the full size, or d=0.05 millimeter. Thus the sample's minimum length must be 15 mm. The horizontal dimension is less critical. A larger area provides a larger signal and is preferable, if it is not obtained at the expense of surface uniformity. A typical value is 10 mm, which is about the size of the windows of the ionization chamber.

3.1.5 Experimental Procedures

The reflectivity and the fluorescence signals are simultaneously monitored: so that these two data sets are available from one measurement. For clarity of

discussion, only one is mentioned at a time, depending on the situation.

(1) **Sample alignment.** After the chambers and the angle stage are set up and aligned along the beam, the stage is leveled in relation to the beam with a precision level (accuracy 30 arcsec) in both perpendicular and parallel directions. The slits must also be leveled. The sample then is set on the top of the stage, near the center. More accurate alignment is made by measuring the separation between the projections of the direct beam and the reflected beam at an arbitrary angle θ' with a polaroid film. This separation is divided by the distance from the sample to the film, usually 1 to 2 meters. The result equals twice the angle of incidence θ. Then, θ' must be recalibrated according to this value. The sample stage should then be brought to $\theta = 0$ and adjusted to such a height that it blocks half of the incident beam, to ensure that the whole beam is intercepted by the sample when θ increases. Figure 3.3 shows a picture of the projections of the direct and reflected beam exposed on a Polaroid film, with the reflected beam on top of the direct beam. The reflected beam also reveals the surface quality of the sample. A rough surface produces more diffused scattering and the reflected beam is less focused and weaker.

(2) **Angle scans.** The reflectivity as a function of the incident angle is measured at a selected energy, either below or above the absorption edge of the sample. A measurement right on the edge is usually avoided because of the complications caused by anomalous dispersion. A typical value of the energy is 200 eV or 300 eV away from the edge. Usually measurements with energies on both side of the edge are taken to facilitate data analysis (discussed further in Chapter 4). These data sets contain fruitful information concerning the sample's layer thickness and interface roughness.

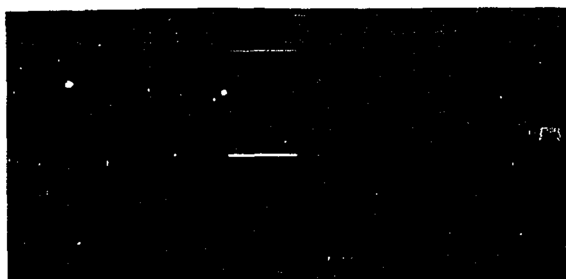

Figure 3.3: Exposure of the reflected X-ray beam (top) and the direct beam (bottom) for angle calibrization

(3) Energy scans. The fluorescence, as a function of the X-ray energy, is then measured at a particular incident angle. The goal is to extract EXAFS. (In Chapter 5, I show that the reflectivity as a function of energy also contains EXAFS.) The incident angle of the X rays determines the penetration depth. Therefore, the EXAFS measured at different angles comes from different depths of the sample. The angle scan described in (2) determines at what angles the EXAFS should be measured. To study the surface, an angle that causes total reflection from the surface should be used. To study the buried interface, the angle should be between θ_c(top) and θ_c(bottom). At a large angle, signals come from the bulk. By comparing the EXAFS from various angles, an in-depth structural profile can be constructed.

(4) The angle correction during an energy scan. When scanning energy at a fixed angle, the penetration depth is not a constant because the critical angle depends on the energy. An extra long-wavelength background makes extracting the EXAFS data difficult. The difficulty can be eliminated by ensuring that the ratio, θ/θ_c, is constant, which can be achieved by correcting the position of the angle stage for each energy step, ΔE, using a PZT on the stepping motor to change the angle. The amount of correction is $\Delta\theta/\theta = 1 - \Delta E/E$: Figure 3.4 shows an example of such a correction. This correction is sometimes deliberately omitted. As dicussed later, the correction can be done during data analysis. In addition, the long-wavelength background due to the variation of the penetration depth and the surface intensity is helpful in determining the error in angle calibration.

3.2 Preparation Of Samples

The samples were thin films deposited on float glass substrates (5 cm x 2.5 cm), or on Si wafers for non-X-ray measurements. Si wafers are not suitable for EX-

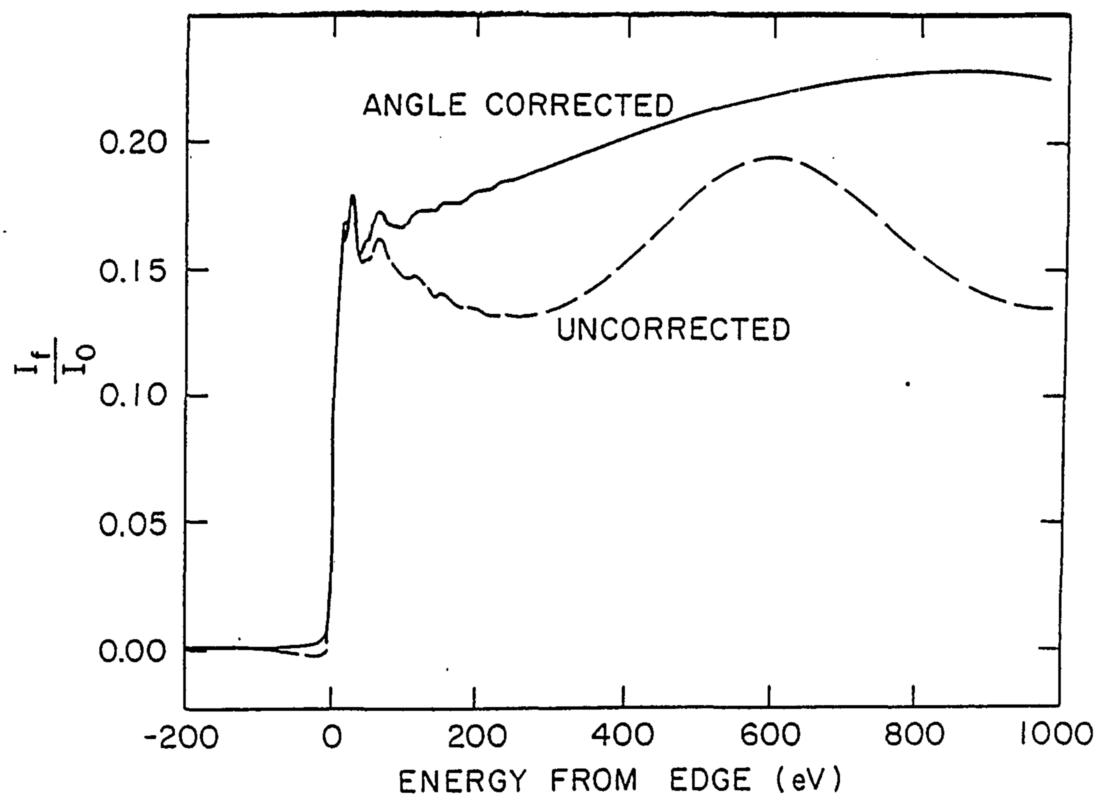

Figure 3.4: EXAFS scans without (dashed line) and with (solid line) the angle correction. Note the elimination of the background.

AFS measurement because of Bragg diffraction from the substrate. Thermal evaporation and RF sputtering were the primary methods of thin film deposition. Cu is deposited first (usually 1000 Å thick), and Al is deposited next, at thicknesses varying from 500 to 1000 Å. The thickness of Al affects the oscillations in the reflectivity curve as a function of the incident angle. When the layer is too thick, the oscillation frequency is too high, which adds too strong a background to the subsequent energy scans. A layer of 600-700 Å is most suitable.

3.2.1 Thermal Evaporation

Originally, a bell-jar system was used for evaporation, whose best base pressure was 1×10^{-6} torr. Considering the possible effects of impurities, we put together a second system at the Material Science Division – a UHV chamber with a base pressure of 4×10^{-10} torr (Figure 3.5). A main concern is the procedure for Al evaporation. Al tends to melt and short-out the W evaporator, which prevents normal Al evaporation. Therefore the heating current has to be applied slowly. An W boat was found to be a better evaporator. The deposition rates were in the order of 2-10 Å per second.

The heat dissipates poorly in the UHV chamber, which might affect interface diffusion: therefore, extra cooling has to be applied to the sample holder. A copper block was clamped around copper tubing through which LN_2 flowed, and the block was placed near the sample holder. Copper braids were attached to the block and the holder to form a heat passage. The flexibility of the copper braids enable the sample holder to rotate, so that multiple samples can be prepared in one pump-down. A thermocouple was mounted on the holder to monitor the temperature. Formation of the interface also might be affected by the ambient conditions. As a test of such effect, an oxygen bottle was attached to a leak

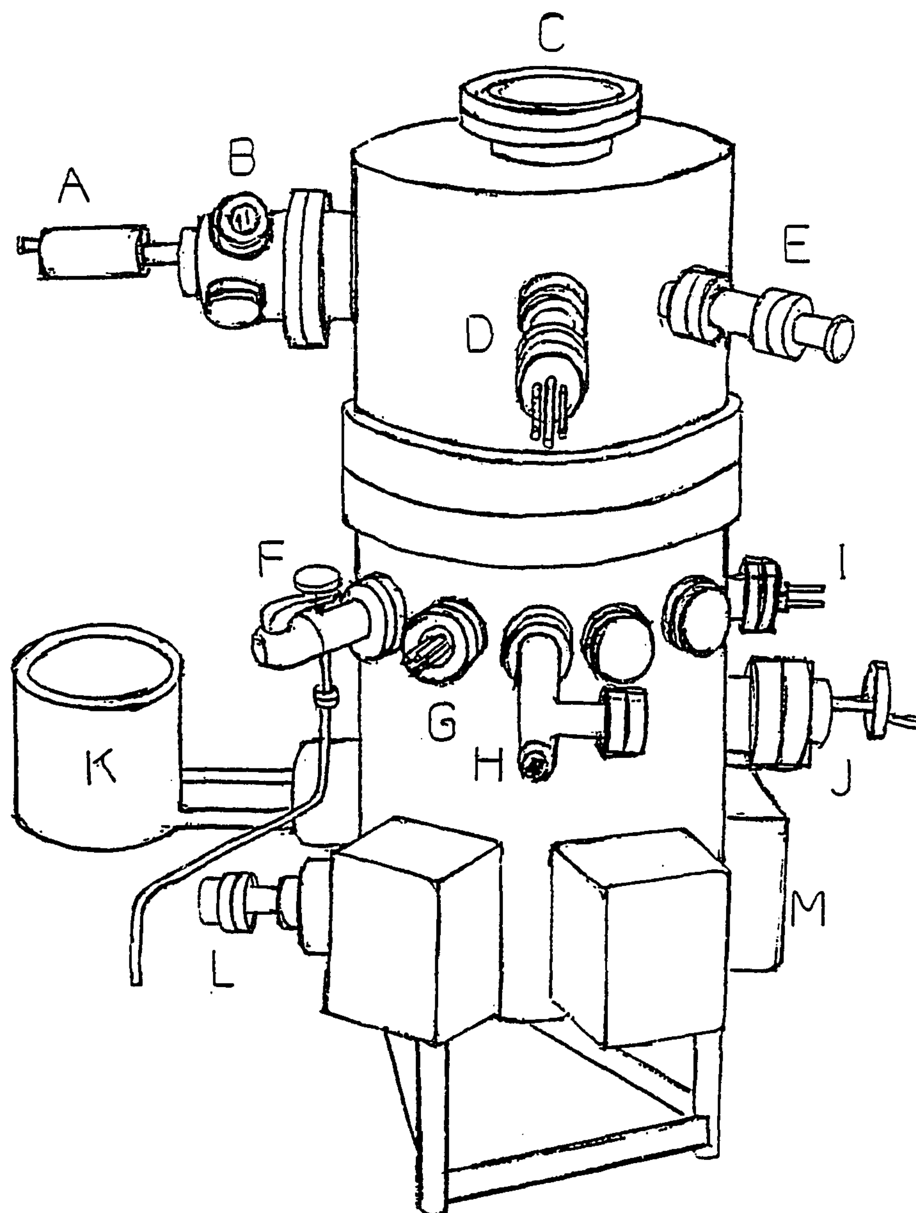

Figure 3.5: The UHV chamber for evaporation. A: Rotary for the sample holder. B: Thermocouple. C: Viewport (also for mounting/dismounting samples). D: Rate monitor. E: RGA head. F: Leak valve. G,I: Evaporator leads. H: Venting valve. J: Valve to ion pumps. K: Liquid nitrogen for TSP. L: TSP. M: Ion pump.

valve to allow controlled oxygen exposure. A mass spectrometer monitors the amount of impurities (typically the partial pressure of CO, one of the common residual gas components, is below 10^{-8}). Oxygen can be added before or during Al evaporation.

3.2.2 Sputtering

Thin films prepared by sputtering have different properties from their evaporated counterparts [40]. What causes these differences is not clear. To test the sensitivity of the glancing angle EXAFS technique, some films deposited by RF sputtering were studied. The sputtering system is a bell-jar system with base pressure $\sim$ 5x10^{-7} torr. Ar ions (pressure $\sim$ 10 millitorr) were used to bombard the targets. The substrates are mounted on a rotating platform to ensure a uniform coating. The rate of deposition and range of thickness are controlled, so that they are similar to those obtained by evaporation. The substrate temperature is also monitored by irreversable thermometers, which change colors at predetermined temperatures. The temperature was found to be lower than 100°C.

3.2.3 Samples and Previous Results

The samples used for this research are divided into the following categories:

(1) HV-evaporated. These samples were evaporated in the bell-jar system, and in general, the films have large grains (Fig.3.6a). Films prepared this way were the first ones made for the glancing angle reflectivity and EXAFS study initiated by Steve Heald. The experiments started by looking for changes at the interface after thermal annealing at 100°C (by dipping the sample in a sealed container into boiling water) for one hour. The thickness of the interface grows exponentially as a function of temperature, and as a

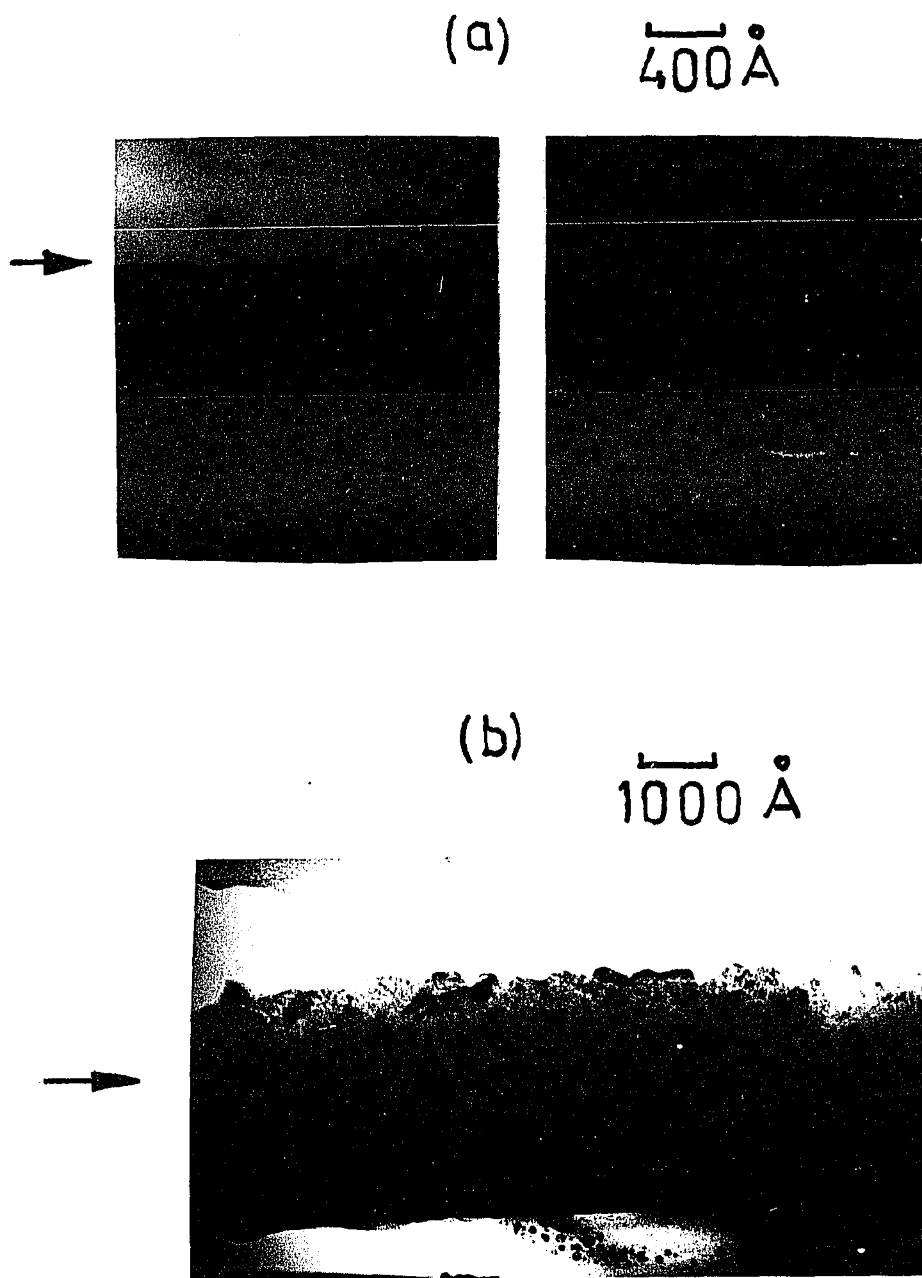

Figure 3.6: TEM pictures of (a) the HV-evaporated sample, with different time of exposure emphasizing the Cu layer (left) and the Al layer (right), and (b) the sputtered sample. The Cu-Al interfaces are marked by arrows. Difference in grain size and the sharpness of the interface are shown.

linear function of time by a diffusion controlled mechanism. According to literature [4], such annealing should generate ~ 50 Å thick mixed interface layer. No change from the unannealed sample was found. The annealing time then was increased to 4 hours, and there was still no change. Therefore, it seemed necessary to increase the temperature: we switched to an electrically heated oven controlled by a Variac transformer. The glancing angle measurements were repeated after annealing at 120°C for 5 minutes, and then we increased the temperature in steps of 20°C steps and measured again after each step. Changes were observed starting at 160°C. Not only was a change observed as a function of temperature, but also we detected a difference in various depths of the sample [41]. In this study, data analysis is carried out on a quantitative level.

(2) RF sputtered. These films have fine grains (Fig.3.6b). After preliminary results were obtained on samples of category (1), similar studies were done on the sputtered samples. The results revealed that the degree of reaction was higher compared to (1) at the unannealed state, and through out the whole range of annealing temperatures. Figure 3.7 and 3.8 from reference [42] shows such differences. Because of the highly mixed interface (represented by a large interface roughness when modeling), not all the reflectivity data from this sample were analyzed quantitatively. Nevertheless, a qualitative comparison still suggested a meaningful question. Since the irreversible thermometers showd that the temperature of the sample substrate was never higher than 100°C, we could think of the following explanations for why (2) was more reacted than (1):

The evaporation chamber was dirty, so impurities at the interface blocked diffusion; During the sputtering process, the sample was bombarded by energetic particles which caused the layers to form in a less ordered way,

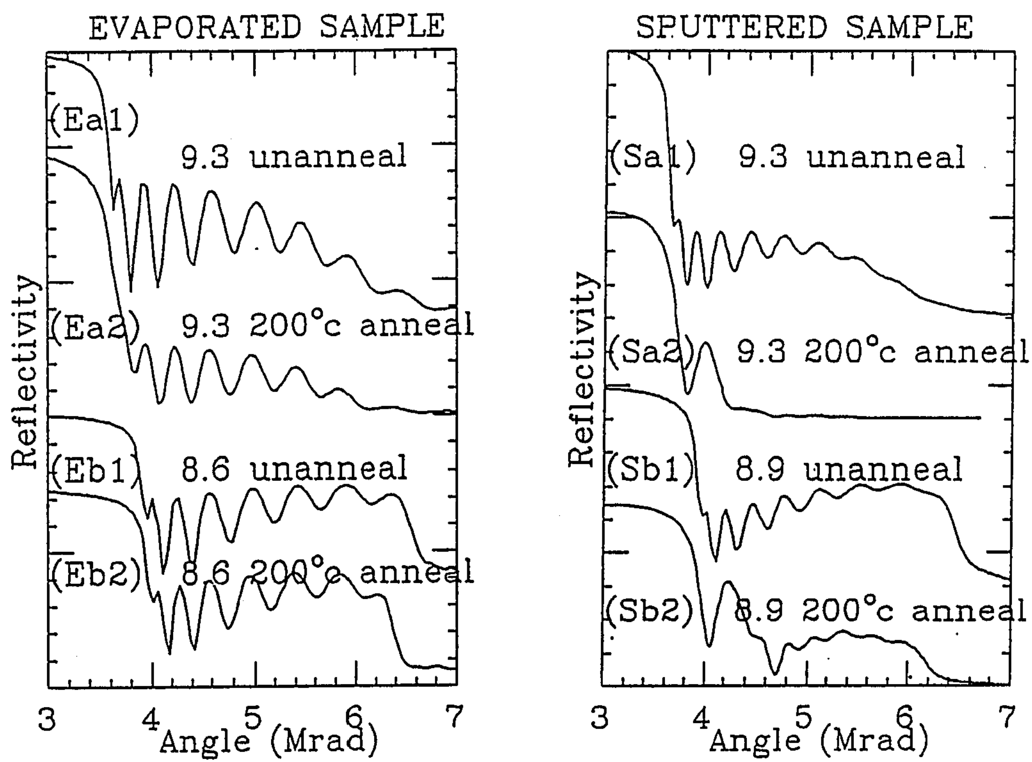

Figure 3.7: Comparison of the reflectivity data obtained from the HV-evaporated sample and from the sputtered sample

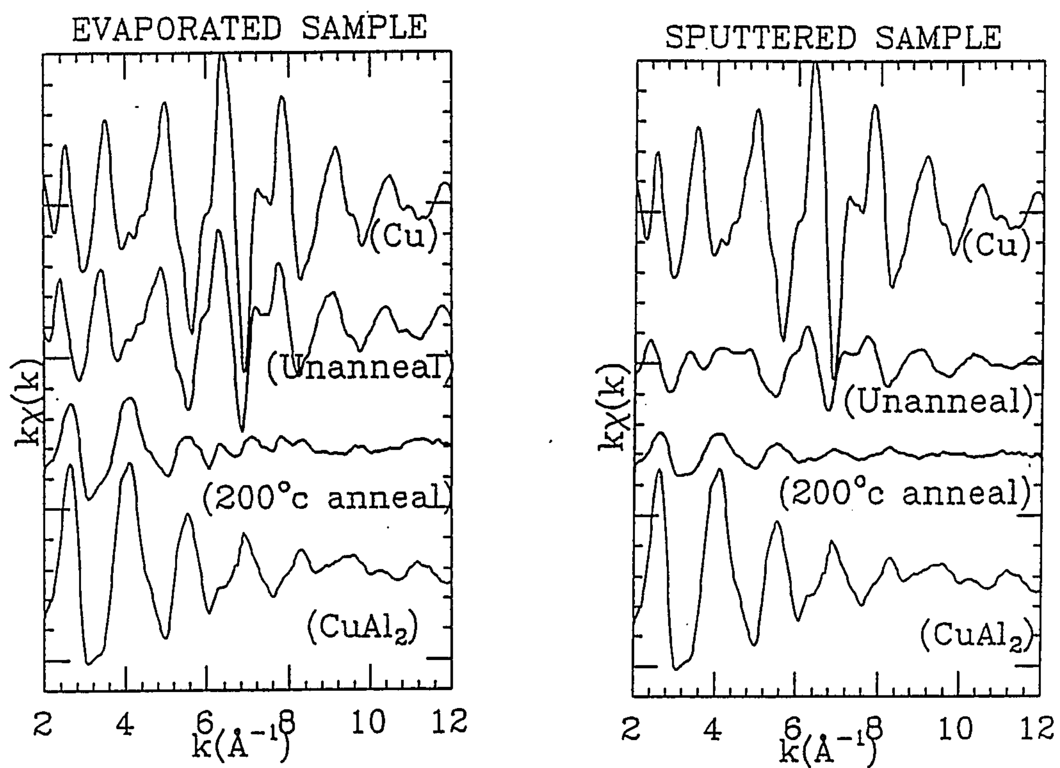

Figure 3.8: Comparison of the EXAFS data obtained from the HV-evaporated sample and from the sputtered sample

resulting in fine grains; The fine grain size in sample (2) enabled quicker diffusion and reaction; 100°C was sufficiently high to trigger diffusion in sample (2) whereas 160°C was needed for sample (1).

There were too many possible factors to be considered. Trying to simplify the problem, several new sets of samples were prepared under more stringent conditions: these are dicussed in category (3).

(3) UHV-evaporated. Sample were evaporated in the UHV chamber at a base pressure of 4×10^{-10} torr. The substrate temperature and ambient conditions were varied as listed below:

condition of	substrate T	O_2 exposure
I	RT	no
II	RT	yes
III	LT	no
IV	LT	yes

where RT and LT stands for room temperature and low temperature, respectively. The purpose of oxygen exposure was to simulate the conditions in the HV chamber. Controlling the temperature would help us to understand the effect of the substrate's temperature on grain size and on the initial reaction.

The UHV chamber was a simple system with thermal evaporators close to each other. The shieldings were not perfectly designed. There were reasons to believe that, on some occasions, the element that was first evaporated also adhered onto the evaporator holding the second element. For the Cu-Al system in this study, it would be the contamination by Cu in the Al. Since the melting point of Cu is higher than Al, it is likely that the Cu impurity is evaporated towards the end of the Al evaporation. The Cu mixed in the Al layer this way will cause a reaction near the surface. Three

out of five samples made under category (3) I and II suffered from such contamination (EXAFS measurement at glancing angles showed surface Cu-Al). At first we thought that it could also due to heating the substrate during evaporation (there was no cooling device in the earlier samples), causing the samples to react as the films were formed. A thermocouple mounted on the sample holder showed that the temperature was not higher than 60°C. It was unlikely that reaction would occur at this temperature, although it was uncertain whether, in an UHV environment, during the depostion process, reactions could take place at a much lower temperature. The answer became clearer when samples under category (3) III and IV were measured. Such mixing also occurred in the first two samples, which were cooled at -100°C and near RT respectively. The degree of mixing of these two samples was even greater than the two good samples under category (3) I and II, which were not cooled at all. The two Al evaporators are mounted on a four-armed feed-through, as shown in Figure 3.9. The geometry is slightly different for the two evaporators: one may be better shielded from the Cu evaporator than the other. We decided that heating the substrate at 60° was not the main factor that caused the premature reaction.

The other purpose of cooling the substrate was to study the grain size. Direct observation were made with an Electron Microscope. Attempts to prepare samples for the TEM study on the cross-section (which produced pictures shown in Fig.3.6) were not successful. We obtained pictures of the top view of the samples, but it was difficult to determine the grain size from them. The low temperature samples are not discussed in this thesis. Only the two good samples under (3) I and II are fully analyzed — UHV and UHV(O), respectively.

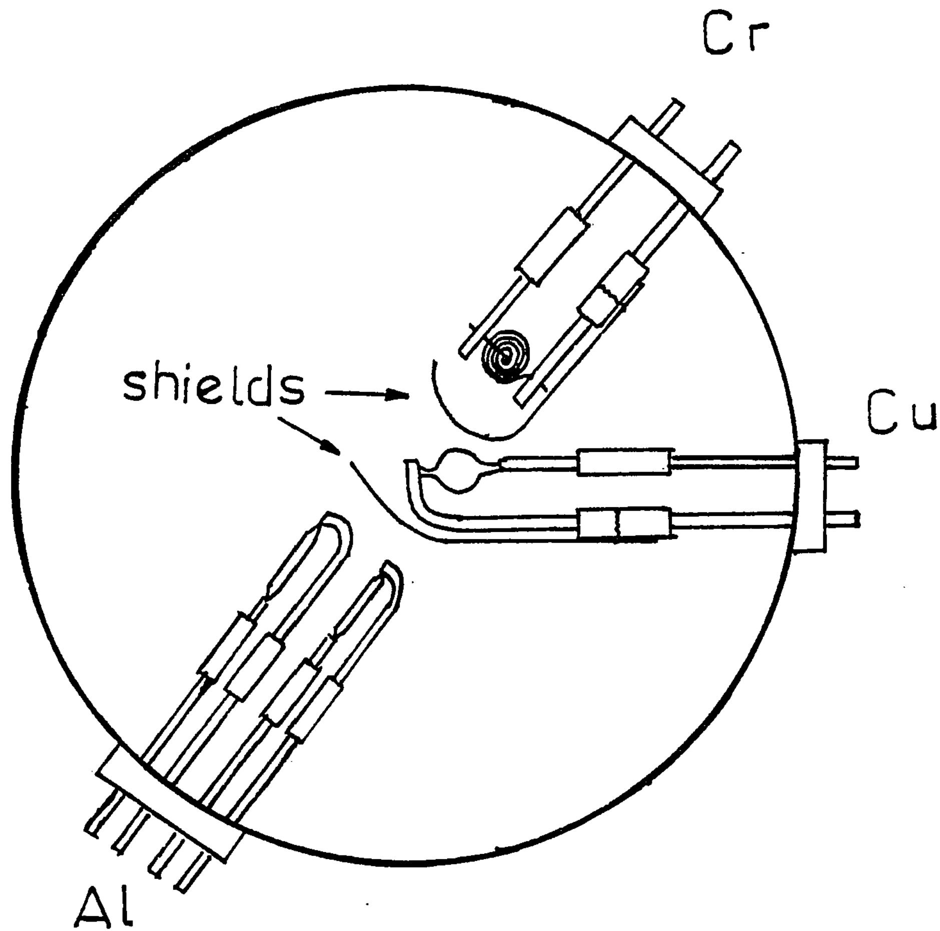

Figure 3.9: The arrangement of the evaporators.

Samples UHV and UHV(O) are free of possible surface Cu contamination, their initial interfacial reactions are not likely due to the heating of the substrates during evaporation. These are essential conditions for studying interfaces.

Other techniques were used to characterize these samples: the results are shown in Chapter 6.

Chapter 4

REFLECTIVITY DATA AND FITTING

The reflectivity, as a function of the incident angle, contains information such as the thickness of the layer and roughness of the interface. Interface reactions change the interface morphology and, therefore, the reflectivity. The reflectivity data is fitted by a theoretical calculation (based on Fresnel equation discussed in Section 2.1) using a model consisting of Al-Cu bi- or tri-layers. An IMSL minimum searching routine, ZXSSQ, is used for fitting. The fitting parameters are refined to reduce the χ^2 error between the data and the calculation. A typical angle scan contains 150 to 200 data points. There are three variables per layer: thickness, roughness, and composition. The reflectivity data consist of two scans, one taken with the incident X-ray energy at 8.6 keV, and the other taken at 9.3 keV (below and above the absoption edge of Cu, 8.98 keV, respectively). The reason of taking two scans is to put more constraints on the fitting parameters, since the data taken below the absorption edge are not sensitive to Cu distribution, whereas the data taken above the edge are. When fitting, it is a good practice to minimize the number of varying parameters. Therefore, instead of having the density of each element in a layer vary independently, the sum of the densities of all elements in a layer is constrained to one.

In this chapter, the reflectivity data from three samples prepared by different

conditions are discussed. For more detailed description of each preparation, readers are referred to Section 3.2. The three samples are listed as follows:

(1) the **HV** sample, evaporated in a HV chamber, 1000Å Al/1000Å Cu/float glass.

(2) the **UHV(O)** sample, evaporated in a UHV chamber, 500Å Al/1000Å Cu/float glass, with $\sim$ 1000L oxygen exposure at the interface.

(3) the **UHV** sample, evaporated in a UHV chamber, 600Å Al/1000Å Cu/float glass.

This chapter first gives a general explanation of the fitting procedures (the step-by-step procedures are summarized in Appendix C). Then, as an example, the procedures are applied to the reflectivity data obtained from sample (3) (the UHV sample). The fitting results for all three samples will also be compared.

4.1 Fitting Procedures

The fitting parameters can be divided into two categories: (A) the parameters that are determined by experimental conditions, such as the angle stage calibration, ratio of I_0 to I_r, and the angular resolution determined by the stepping motor and slit settings, and (B) those determined by the sample characteristics, such as layer thicknesses, roughnesses and densities. Some parameters are more likely to compensate other ones, in other words, some are more closely correlated. For example, the absolute angle calibration is correlated to the amount of Cu in the Al layer, which, in turn, is correlated to the normalization of the reflectivity. The sensitivity of the data to each parameter varies as the angle varies. The parameters mentioned in the example given above have stronger effect on the lower angle range (from below θ_c(Al), the critical angle of the Al

layer, to just above it) than on the range beyond. On the other hand, parameters such as the thickness of the Al layer and the density of the underlying layer, have little influence on the lower angle range yet play crucial roles on the higher angle range. Considering the time consumption by the computer, the number of varying parameters is restricted to six at a time. Therefore, it is important to organize the parameters in the right combinations.

Generally the fitting is done generally in two steps.

(1) Fit the low-angle part of the data (below and near θ_c(Al)), which is only sensitive to the surface feature of the sample. This is a short range, consisting of 20 or 30 points. The parameters determined from this fit are the experimental ones: the zero angle θ_0 and the normalization factor, and the surface-related model parameters: surface roughness and the amount of Cu near the surface. Figure 4.1 shows an example of the first-step fitting: how each parameter influences the curve. The normalization, NOR, is related to the response of the ionization chamber to the X rays at different energies. NOR is the only parameter which is not shared by the two scans, therefore has to be fitted individually.

(2) Once the surface-related parameters are determined from (1), fit the whole-range of data with the rest of the parameters. The goal is to obtain a reasonable fit with a minimum number of layers. The usual practice is to start with a bilayer model and adjust the three parameters associated with each layer. An increase in the roughness reduces the oscillations in the reflectivity, which represents an increase in the degree of mixing. When the mixing at the interface is so strong (e.g. a plateau forms in the average density) that the interface can not be modeled by increasing the roughness, a trilayer model is needed, and so on. Refine the parameters fitted in (1) if necessary.

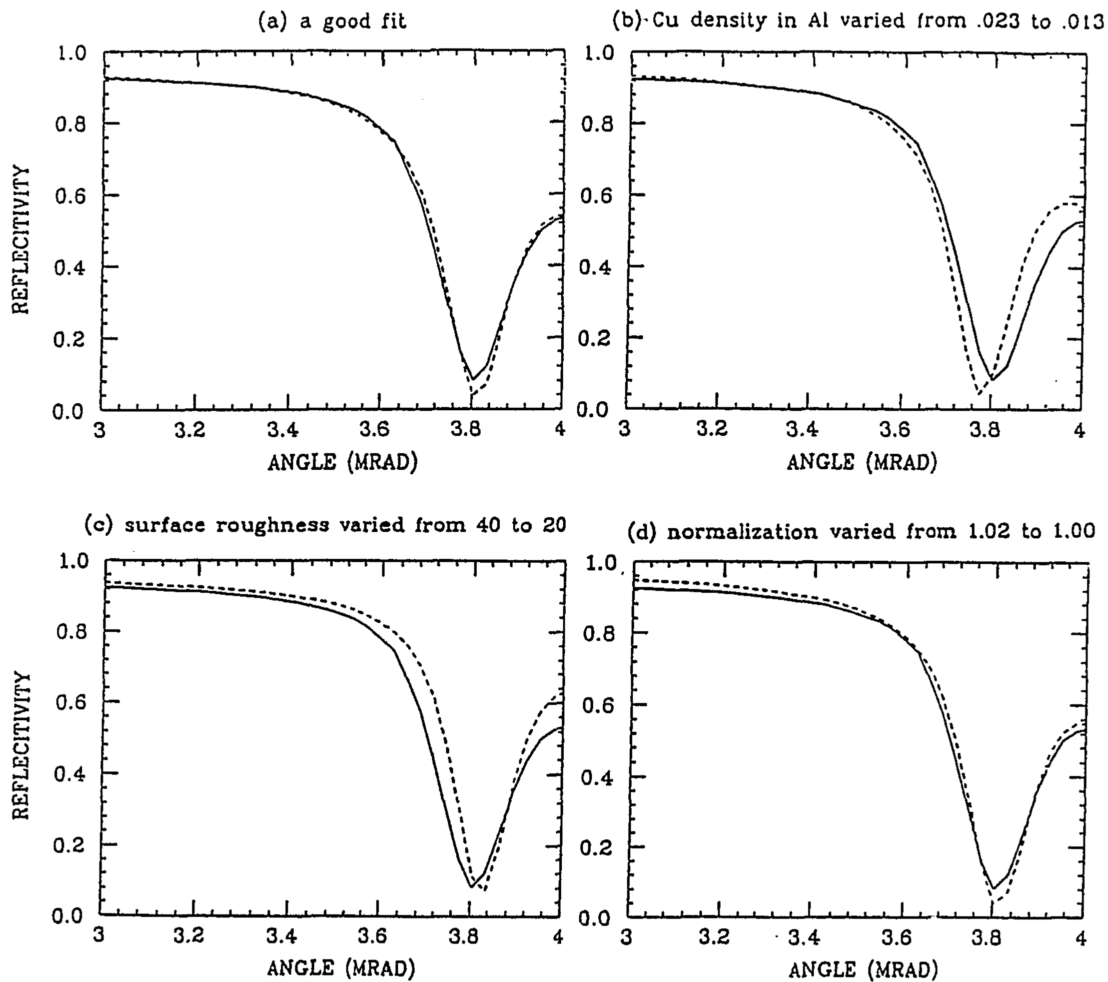

Figure 4.1: First step of fitting: Reflectivity as a function of angle, at a shorter range.

The reflectivity data from the UHV sample is used as an example for the analysis. The sample is annealed at 65°C for five minutes, then measured after cooling down to room temperature. Again, the sample is annealed at 80°C and the measurement repeated. The cycle goes on at 20° steps until 180°C. To start with, the reflectivity data are fitted with a three-layer model (Al layer/mixed layer/Cu layer). Above the Al layer, there is a thin layer of Al_2O_3 (~30Å). Within the Al layer, there is a small amount of Cu. The thickness of the Cu layer is assumed to be infinite, since within the temperature range, the annealing 1000 Å of Cu is far from being used up. Also, the Cu thickness only affects the data at the angle range above the critical angle of Cu, but the interface below the Cu layer is not of the concern of this study.

Figure 4.2 shows all reflectivity data and their fits at various annealings. Table 4.1 compiles the parameters obtained from the fitting. To reconstruct the compositional profile, the Cu density in each layer listed in Table 4.1 are plotted as a function of depth. At each interface, the densities are smeared by the roughness which follows the Gaussian distribution [36]:

$$\rho(z) = \rho_0 \frac{1}{\sqrt{2\pi\sigma^2}} \int_{-\infty}^{z} exp[\frac{-(z-z_0)^2}{2\sigma^2}]dz.$$

where σ is the RMS roughness. The integral is a form of the Complemetary Error Function:

$$\text{erfc}(x) = \int_{-\infty}^{x} e^{-x^2} dx.$$

Using $\text{erfc}(0) = 1, \text{erfc}(-\infty) = 2$, and $\text{erfc}(\infty) = 0$, the density of Cu can be expressed as:

$$\rho(z) = \rho_0(1 - 0.5\text{erfc}(\frac{z - z_0}{\sqrt{2}\sigma})).$$

ρ_0 is the nominal density of the layer. Putting all the layers together, a density profile can be constructed for the whole sample. This procedure is demonstrated in Figure 4.3. Figure 4.4 summarizes the composition profiles for all three sam-

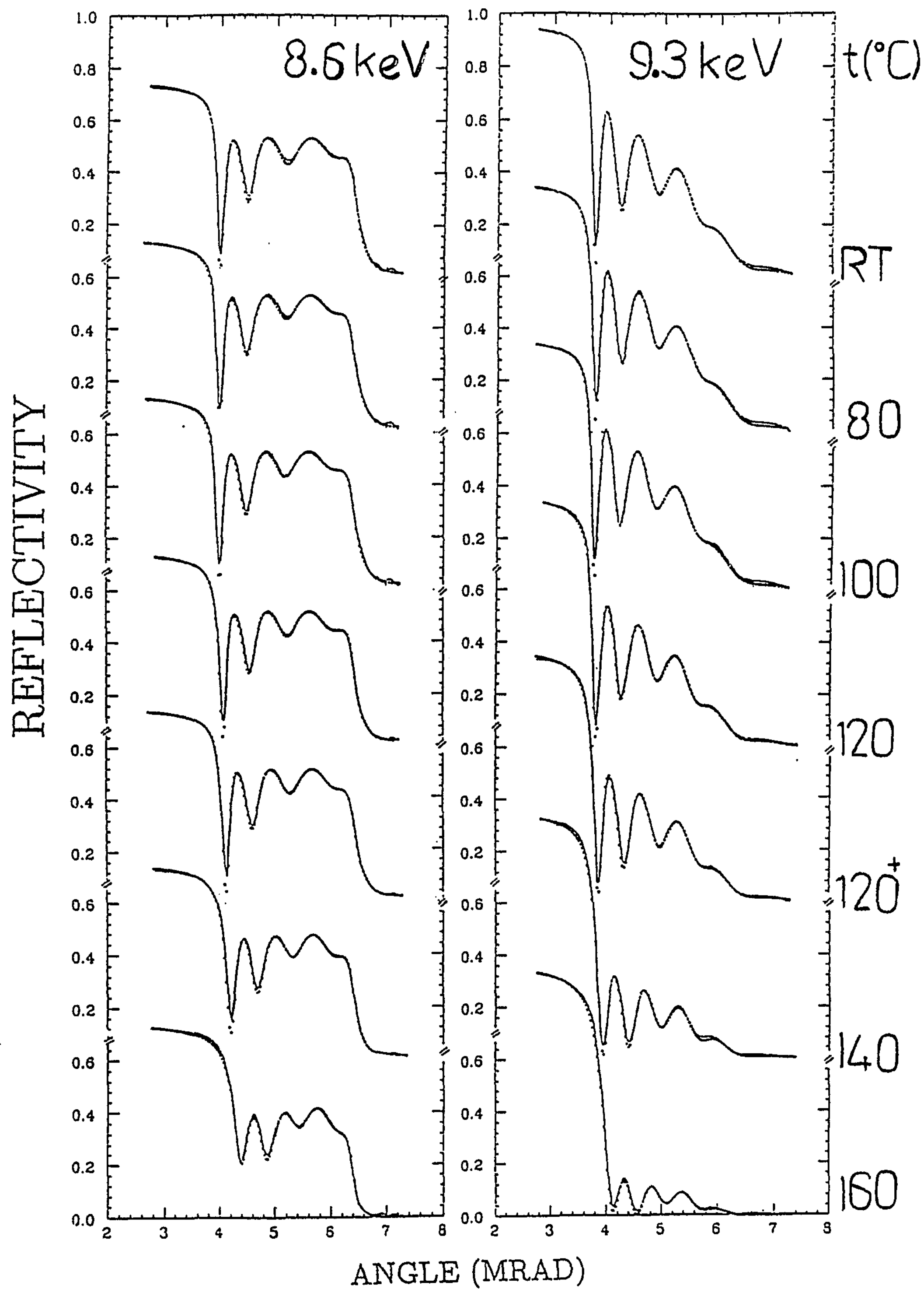

Figure 4.2: Reflectivity as a function of angle, at various annealing temperatures for the UHV sample. Lines: data, points: fitting.

Table 4.1: Model fitting results of the reflectivity as a function of the annealing temperature for the UHV sample. D is the thickness, ρ the relative density, σ the roughness, ϕ the correction for the incident angle, and n the normalization.

t(°C)	layer	D(Å)	ρ_{Cu}, ρ_{Al}	σ(Å)	ϕ_0(mrad)	n(8.6)	n(9.3)
RT	1	17	Al_2O_3	27	-0.097	1.32	1.04
	2	494	0.008, 0.992	0			
	3	23	0.170, 0.830	40			
	4		0.931, 0.069	18			
65	1	32	Al_2O_3	40	0.005	1.31	1.03
	2	480	0.004, 0.996	28			
	3	39	0.153, 0.847	41			
	4		0.932, 0.068	21			
80	1	30	Al_2O_3	41	-0.057	1.31	1.03
	2	481	0.006, 0.994	29			
	3	40	0.177, 0.823	35			
	4		0.931, 0.069	21			
100	1	34	Al_2O_3	44	-0.016	1.31	1.02
	2	469	0.007, 0.993	31			
	3	52	0.162, 0.838	30			
	4		0.932, 0.068	21			
120	1	30	Al_2O_3	40	0.140	1.31	1.02
	2	468	0.023, 0.977	26			
	3	65	0.192, 0.808	25			
	4		0.934, 0.066	20			
140	1	33	Al_2O_3	42	0.033	1.30	1.01
	2	459	0.038, 0.962	27			
	3	68	0.203, 0.797	29			
	4		0.933, 0.067	20			
160	1	31	Al_2O_3	44	0.111	1.31	1.03
	2	261	0.040, 0.960	24			
	3	260	0.109, 0.891	50			
	4	30	0.599, 0.401	50			
	5		0.937, 0.063	20			
180	1	36	Al_2O_3	50	0.065	1.32	1.02
	2	74	0.030, 0.970	32			
	3	151	0.097, 0.903	43			
	4	111	0.178, 0.822	37			
	5	221	0.215, 0.785	50			
	6	317	0.924, 0.076	50			
	7		0.938, 0.062	19			

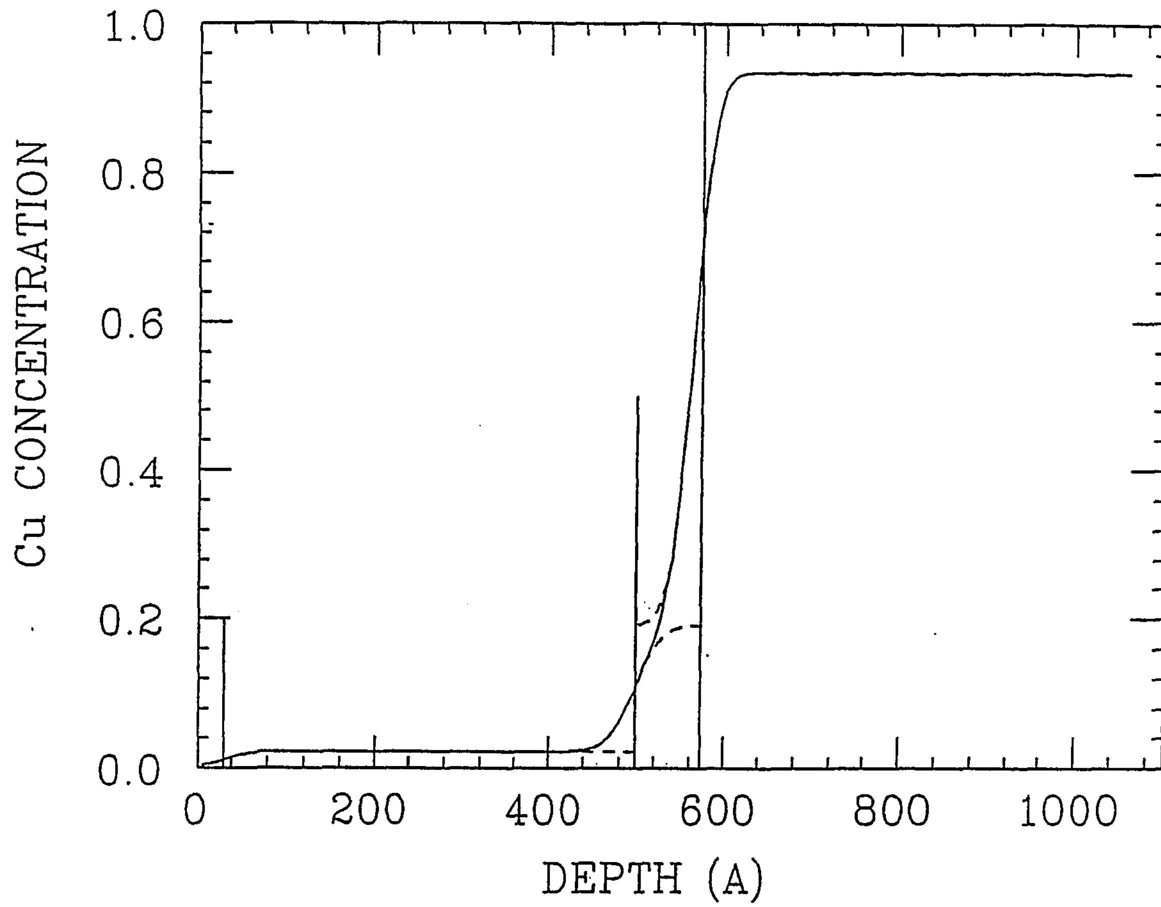

Figure 4.3: Construction of the Cu concentration profile. Dashed lines: Densities following a Complementary Error Fuction for each interface; Solid line: The overall density.

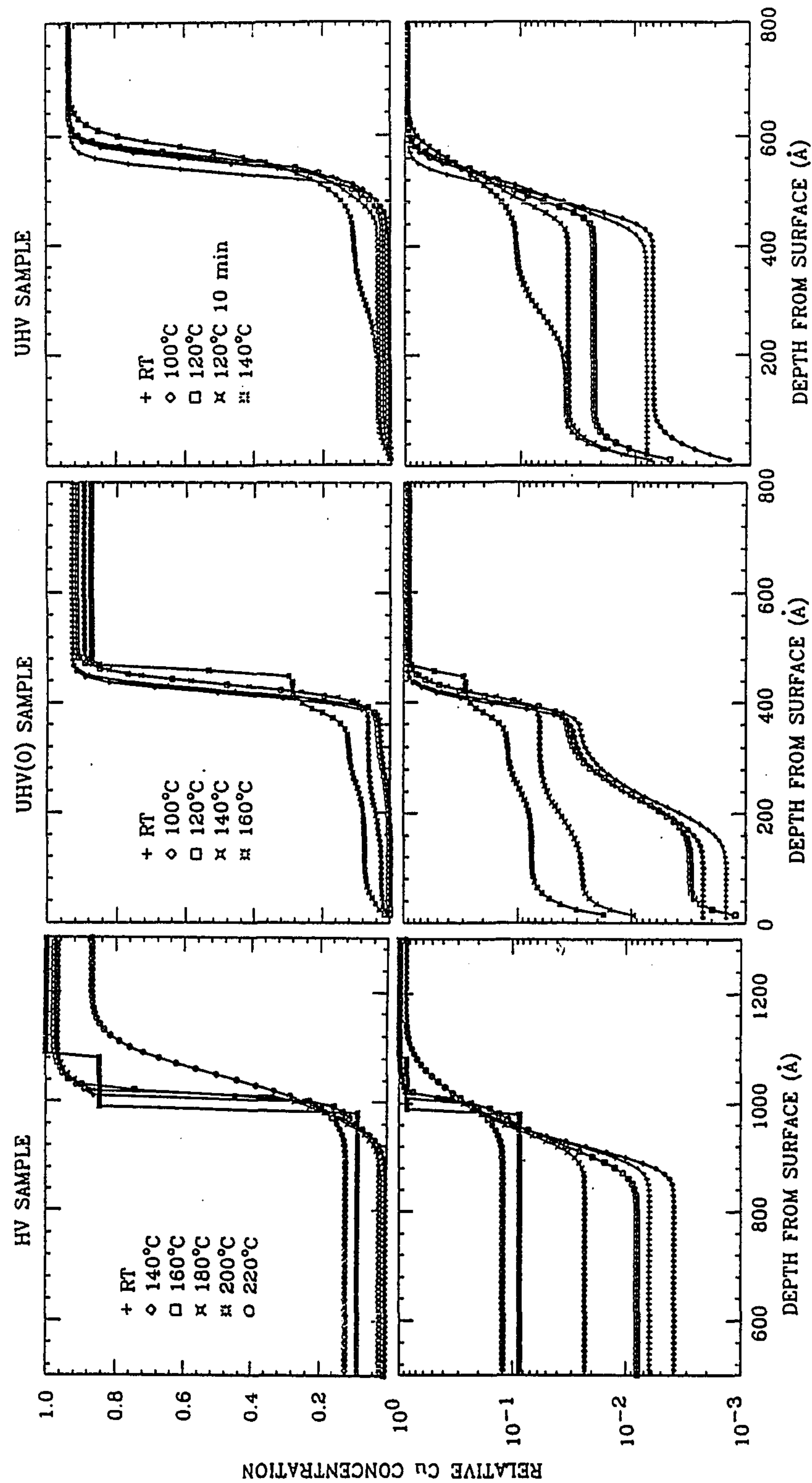

Figure 4.4: Models from fitting: Cu concentration depth profile. From left to right: HV, UHV(O), UHV.

ples at all annealing temperatures. These profiles give a clear picture of the samples, also they are important model. for the later quantitative analysis of EXAFS data.

4.2 Discussion Of Fitting Results

4.2.1 As Deposited

Table 4.1 shows that there is a small amount of Cu ($\sim$ 0.85 at.%) in the Al layer, even at room temperature. The solubility of Cu in Al is very low ($\sim$ 0.02 at.% at room temperature, from [2]). Therefore, any Cu in the Al layer is likely either to fill in the grain boundaries (GBs) or to segregate onto the surface of Al. Viewing the from the surface, Cu should emerge from the GB openings. There is also possibility of forming Cu clusters or even a continuous layer of Cu on the surface if there is excess supply of Cu. To gain surface sensitivity, the incident beam is fixed at a glancing angle (($\theta < \theta_c$(Al)) so that the penetration depth is limited to $\sim$ 30 Å below the surface, and the beam energy is scanned across the absorption edge of Cu. If there is a surface Cu contribution, a "step" should show up in both the fluorescence and reflectivity data. The fluorescence measurement is more sensitive than the reflectivity [41], but the latter is free of problems caused by the scattering from the bulk Cu, which reduces the sensitivity of the surface Cu. There is a small step, $\sim 0.006 \pm 0.003$, seen in the reflectivity data (Fig. 4.5a). Whether it is caused by the surface- or GB-Cu is discussed below:

(1) **GB Cu.** Assume that the contribution to the 0.85 at.% of Cu is from the Cu sitting in the GBs of the Al layer. (The rapid GB diffusion is well known for thin polycrystalline films [45].) A model calculation incorporating a typical surface roughness and an Al oxide layer suggests that this amount of Cu gives a step of $\sim$ 0.003 in the reflectivity data(Fig. 4.5b), in agreement with the data within the exprimental error. One can then evaluate an average

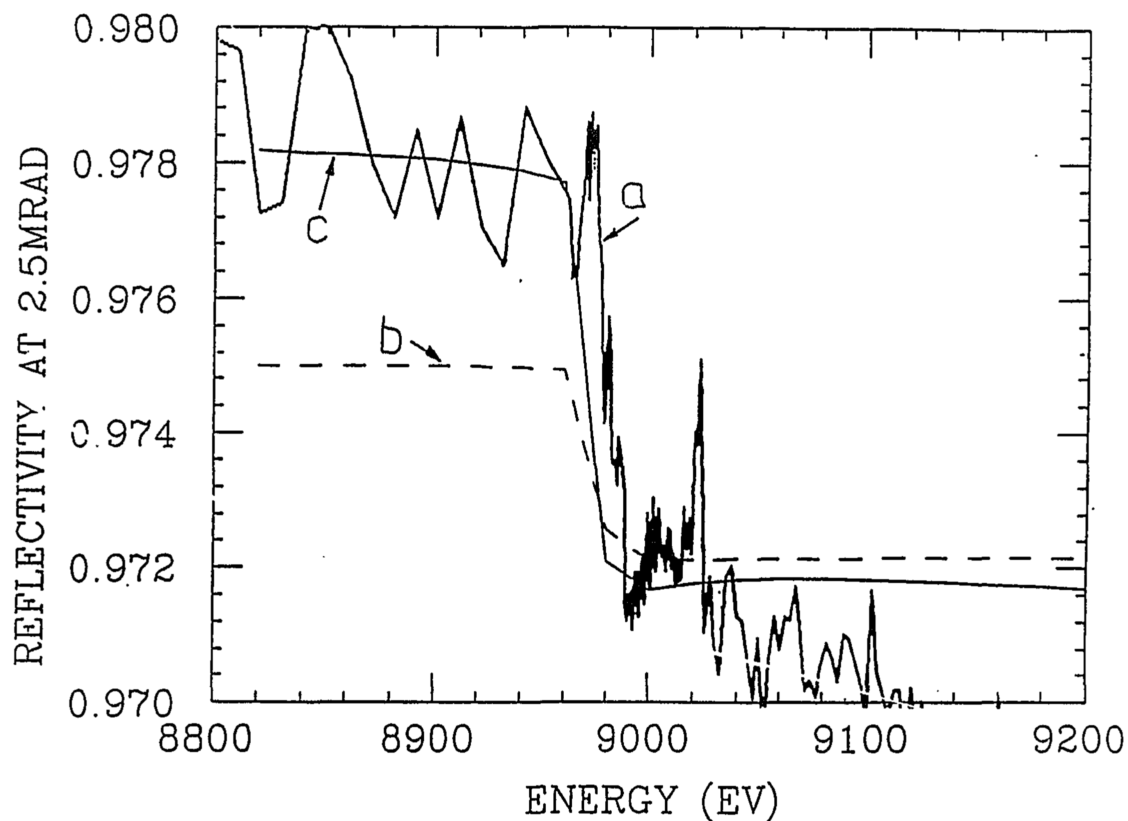

Figure 4.5: Reflectivity as a function of the X-ray energy: a: Data taken at 2.5mrad on sample UHV annealed at 120 degrees; b: Calculation assuming only GB Cu contributes; c: Calculation assuming a thin surface Cu layer in addition to GB Cu.

grain size of the Al layer. Assume the grains are squares and the Cu atoms fill in the GBs in single layers. As illustrated in Figure 4.6, each Al grain has four GBs, but each GB is shared by two Al grains. The ratio of the number of the Cu atoms in the GBs to that of the Al atoms in the grains is:

$$\frac{N_{Cu}}{N_{Al}} = \frac{2L/(2R_{Cu})}{L^2/\pi(R_{Al})^2} = 0.85at.\%$$

where L is the size of the grains. Knowing R_{Cu}=1.28 Å and R_{Al}=1.43Å, the calculation yields L $\sim$ 600 Å, which is about the size of the Al film thickness! The amount of Cu in Al is confirmed by a RBS measurement (data shown in Chapter 6, Figure 6.1). Due to the difficulty in preparing samples for the TEM measurement, the grain size could not be observed directly for the UHV samples. Successful TEM measurements on the HV sample show that the grain size was of the same order as the film thickness (Fig. 3.6a.)

(2) Surface Cu. If some of the 0.85 at.% Cu is from a continuous layer of Cu on the surface, the model calculation mentioned in (1) shows that it must be less than 6 Å, so that the step size is comparable (Fig. 4.5c). It is legitimate to say that the amount of surface Cu is less than the equivalence of a concentrated 6 Å layer, or two atomic layers. The presence of such a low level of surface Cu would not affect EXAFS signal significantly. The lack of a surface layer may be due to the formation of the surface oxide, which blocks the GB paths. If the Cu diffuses to the surface when the sample is still *in situ*, then an observable segregated layer of Cu might form at the surface, before the oxide layer forms. This situation is more likely to occur on samples with a thinner Al overlayer, since it takes less time for the Cu to travel to the surface under the same conditions for deposition. However, on all the samples prepared and studied, such rapid

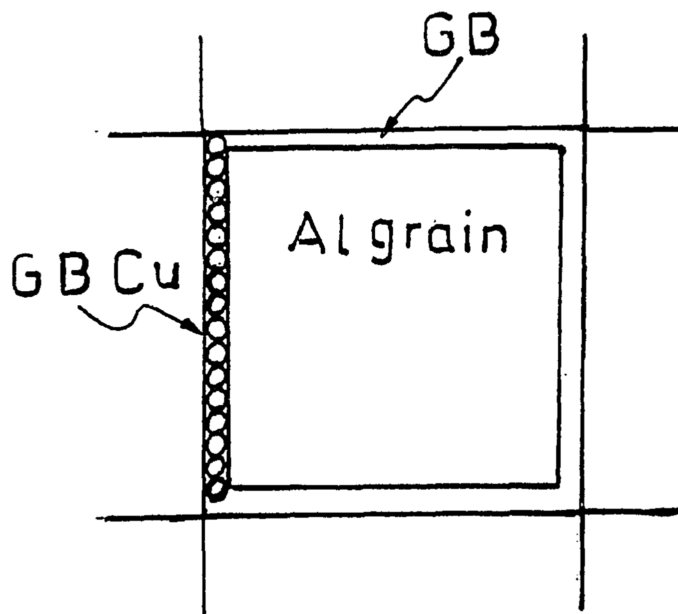

Figure 4.6: Illustration of grain size estimation

migration of Cu to the surface was not observed. This finding suggests that the GB diffusion happens while the sample is being aged in the air.

4.2.2 Annealing Behavior

As the temperature increases, the amount of Cu in the Al layer increases while the thickness of the layer decreases. The mixed layer evolves towards a Cu-rich direction and its thickness increases. These changes are what we can expect from interdiffusion. Extra intermediate layers appear at the higher temperatures (160°C and 180°C), indicating that large-scale reactions have begun.

The reflectivity data provide a quantitative picture of the density distribution in thin film samples, without regard to the specific form of the chemical reactions (whether the Cu and Al are bonded or just sitting together physically). Although the lack of compositional information makes the determination of the diffusion mechanism difficult (such as growth rate of a compound layer), it is worth an attempt based on a crude assumption, namely that the mixed layer(s) consists of a mixture of $CuAl_2$ (a most likely compound, according to the phase diagram and other studies) and unreacted Al or Cu, whichever is in excess. Such an assumption is a starting point, which has to be verified later.

For a diffusion-controlled growth kinetics [46], the thickness of the $CuAl_2$ layer should follow the $\sqrt{t}$ law, where t is the annealing time:

$$\frac{x^2}{t} = K_0 e^{-\frac{Q}{kT}},$$

where x is the thickness of the growing compound layer during time t, and K_0 is the diffusion coefficient. Using $k = 8.62 \times 10^{-5}$eV/deg (Boltzmann constant), this equation becomes:

$$\frac{x^2}{t} = K_0 e^{-11.6Q\frac{10^3}{T}}.$$

This equation leads to the Arrhenius plot in Figure 4.7 (natural log of the rate of the growth vs the inverse annealing temperature, T). The slope of the curve

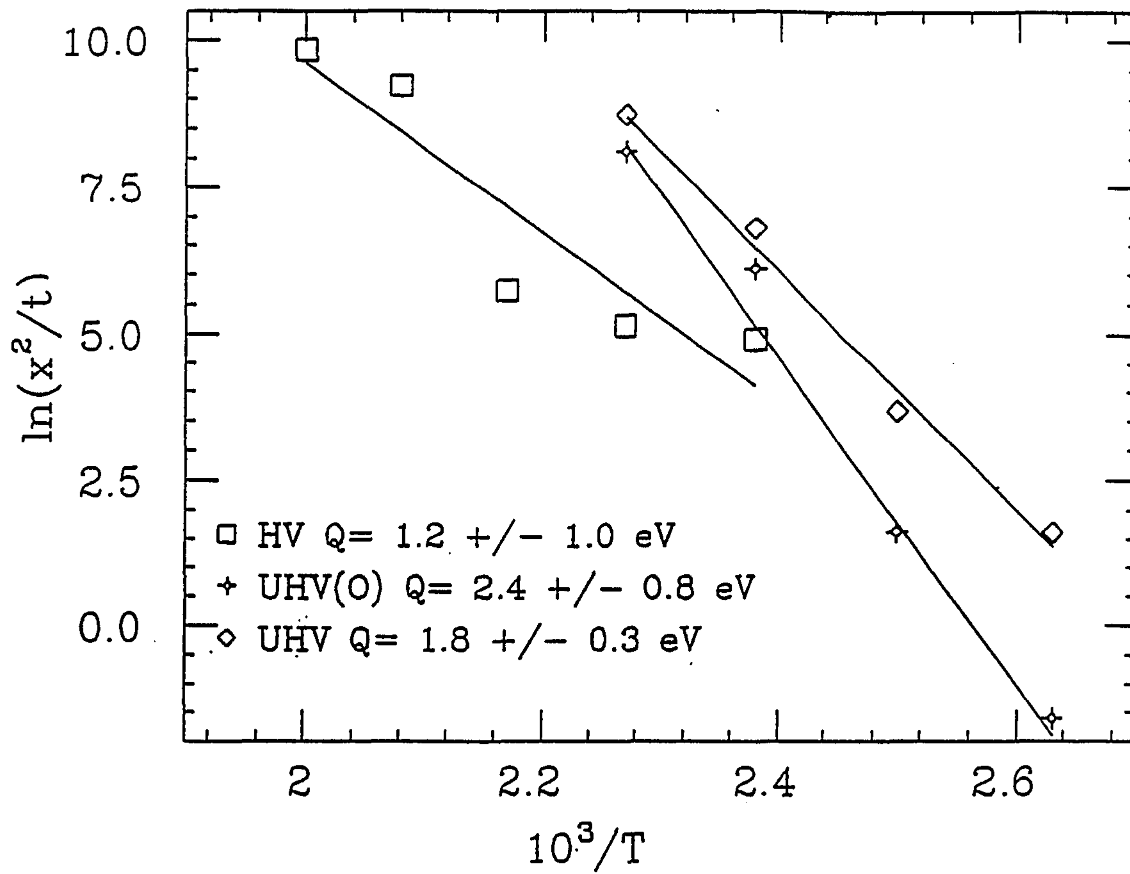

Figure 4.7: Arrhenieus plot of the interface growth on the HV, UHV(O), and the UHV samples.

represents the activation energy of growth. In the Cu-Al system, the growth of the $CuAl_2$ layer from thin films should be of the order of 1.2 – 1.3 eV [2]. Such a relation seems to be observed, considering the crude model used. Despite the difficulty in studying the growth mechanism quantitatively at the initial level, differences among the three samples are revealed and are compared in the next subsection.

4.2.3 Comparision of Three Samples from Various Preparations

Figure 4.4 also shows the density profiles obtained from fitting the reflectivity data from the other two samples at various annealing temperatures. At room temperature and low annealing temperatures, the HV and UHV samples have a similar Cu concentration (ρ_{Cu}) in Al, compared to the UHV(O) sample which has a considerably lower level ($\sim$ 50% lower). Since the amount of Cu in Al at this temperature range is mainly due to diffusion along the grain boundary, the reason that there is a lower level of ρ_{Cu} in near the surface of the UHV(O) sample can be speculated as either (1) some barrier that blocks such diffusion, or (2) the larger size of the grains.

Concerning speculation (1), the barrier could be the oxide layer formed at the interface by oxygen exposure. The interfacial formation of the Cu-Al compound could also serve as the barrier. The first barrier was reported in other studies [47,48] in a case of Al being deposited first. These authors suggested that if the noble metal was deposited first (in our case Cu), then the effect should be reduced. The second barrier would be true only if there is more compound formation in the UHV(O) sample than the other two samples. This possibility was investigated by X-ray Photoemission Spectroscopy experiment.

The XPS study on the Cu-Al interface indicates that an Al/O/Cu interface has a larger mixed region than an Al/Cu interface ([50], details shown in Chapter

6). It means that the oxygen exposure either enchances the interface reaction initially, or causes the Al to form clusters. Either one could explain the noticable intermediate layer in the UHV(O) sample even at room temperature. It will be shown later that the first guess is not supported be the EXAFS result.

The speculation (2), about grain size, is not directly supported by evidence, since the TEM picture is not available. In fact it is contracdicting the clustering guesss (which makes finer grains). At higher temperature anneals (140°C and higher), the UHV and the UHV(O) have very similar behaviors. The level of Cu in the Al layer of the UHV(O) sample begins to catch up with that of the UHV sample. The similar behavior is an indication of the breakdown of the diffusion barrier at the UHV(O) interface. Alternatively, it could mean that the activation energy for diffusion through the oxide layer is lower than for diffusion through the metallic compound layer, therefore the latter is the rate limiting process for interface growth. The $\sqrt{t}$ growth law is also observed, with a higher activation energy.

The HV sample does not follow the $\sqrt{t}$ growth as well as the other two samples (there are bigger deviations from a straight line). Due to the larger error bars, it is hard to compare with the other two samples. Th HV sample showed a different growth, even though the initial Cu level in the Al GBs is comparable to that of the UHV. Since the HV sample was made in a different chamber, the difference in pressure alone (10^{-10} vs 10^{-6} torr) was probably not the only reason to cause all the differences. The impurity content can be important. The thickness of the Al in the HV sample could have some influence: to what degree the thickness affects the reaction would be an interesting subject for future study.

4.3 Estimation Of Error Bars Of Fitting Parameters

Error bars should be put on the fitting parameters. The error of one parameter is determined by a deviation from the parameter's optimum value, which causes the minimum χ^2 to increase by a level $\Delta\chi^2$. The higher the level, the larger the region that contains the probability distribution for the parameter. In the case of six varying parameters (degree of freedom = 6), $\Delta\chi^2$ is 10.6 in order to cover 90% of the probability distribution [49]. In other words, the error bar in one parameter is determined by increasing χ^2 by 11. The number of data points for a typical scan is more than 100, and the number of independent points (determined by the angular resolution of the experiment) is about half of that number. So $\Delta\chi^2/\chi^2 \simeq 20\%$ is used as a criterion to judge the fitting. The shape of the minimum varies from parameter to parameter, but the minimum for a particular parameter should be very similar from scan to scan. Therefore, only one set of parameters from one situation is examined for errors. The error bars are then assumed to be suitable for other sets. Starting from a set of parameters which gives a desirable minimum in fit, an error bar in a parameter can be evaluated by the following procedure: The parameter a is changed to a new value $a + \Delta a$ and is fixed at this new value, then let all other parameters vary to reach a new minimum in the fit. If the new minimum deviates from the original minimum by 20%, Δa is accepted as the error bar of a. The relative error ($\Delta a/a$) of a typical set of parameters is listed in Table 4.2, in which the subscript 0 represents the surface layer and 1 is one layer below, and so on. It is not too suprising that the parameters from deeper layers are less sensitive. Big error bars on the roughnesses indicate that they are more closely correlated: one interface can be made smoother if the adjacent layer is made rougher to compensate. This feature shows the limitation of fitting in determining roughnesses of individual

layers. The more layers used in the model, the more difficult it is to determine roughness. However, the model does give an idea of how rough the sample is as a whole.

Table 4.2: Estimated errors of the fitting parameters.

a	σ_0	D_1	σ_1	ρ_1	D_2	σ_2
error	0.08	0.06	0.50	0.02	0.20	0.60

Chapter 5

EXAFS DATA AND ANALYSIS

5.1 Indirect Measurement of EXAFS

A direct measurement of EXAFS refers to a transmission measurement which gives the total absorption coefficient μ of the bulk sample. An indirect measurement is any measurement that records a signal which is related to μ. This signal can be, for example, the fluorescence or the reflectivity. In the case of thin film samples, it is neccessary to use indirect measurements because a layered structure is unsually studies and a total signal does not give spatial resolution.

Both fluorescence and reflectivity methods have been used in qualitative surface and interface studies [23]-[26]. Only recently has quantitative analysis become available [44]. Progress was hampered by the anomalous dispersion that affects both the near-edge and the EXAFS. A procedure of Anomalous Dispersion Corrections (ADC) has to be applied. Section 5.3 gives a detailed discussion on the subject.

In this study, the fluorescence yield is the main source of obtaining EXAFS. Theoretically, either the fluorescence or the reflectivity can provide correct EXAFS information. From a technical point of view, it is more difficult to analyze the reflectivity EXAFS because of the stronger distortion at the edge due to the anomalous dispersion effect.

Despite the ADC effect, a qualitative picture is often valuable. EXAFS data

from the Cu-Al systems are shown in section 5.2 before the ADC: Section 5.4 gives quantitative results after applying the ADC.

5.2 EXAFS Data

After each annealing, the EXAFS were measured at a few different angles to probe various depths of the sample. Figure 5.1 is a typical angle scan of the reflectivity (from the UHV sample annealed at 120°C) described in Chapter 4. The scan is used for calibrating the angle of incidence. Most measurements were taken at the first minimum (V1) after θ_c(Al), the first (P1) and the second maximum (P2). Figure 5.2(a) illustrates a model calculation of the contribution of X-ray fluorescence from various depths of the sample at the angles V1, P1, and P2. The model (shown in Fig. 5.2(b)) was obtained from fitting to the reflectivity in Chapter 3. The fluorescence is the product of the X-ray intensity inside the layer and the Cu distribution. This figure shows where the EXAFS signal is from, and also the ratio of the contribution from various depths. The measured fluorescence signal is the integration of the intensity shown in Figure 5.2(a).

5.2.1 EXAFS Data from Unannealed Samples

Figure 5.3 compares EXAFS data from the UHV and UHV(O) samples as deposited at V1, P1, and P2. On the top and the bottom of the figure, the Cu and $CuAl_2$ standards are plotted. The Cu-Al reaction is represented by the growing of $CuAl_2$ features and the diminishing of Cu features. The most prominent features are highlighted with arrows on the Cu and $CuAl_2$ standards. In general, the shallower the incident angle, the less signal is detected from the bulk. Therefore, the portion of the signal from the reacted region is the largest for the data from V1. The data from P1 is the next highest, and P2 is the smallest (see

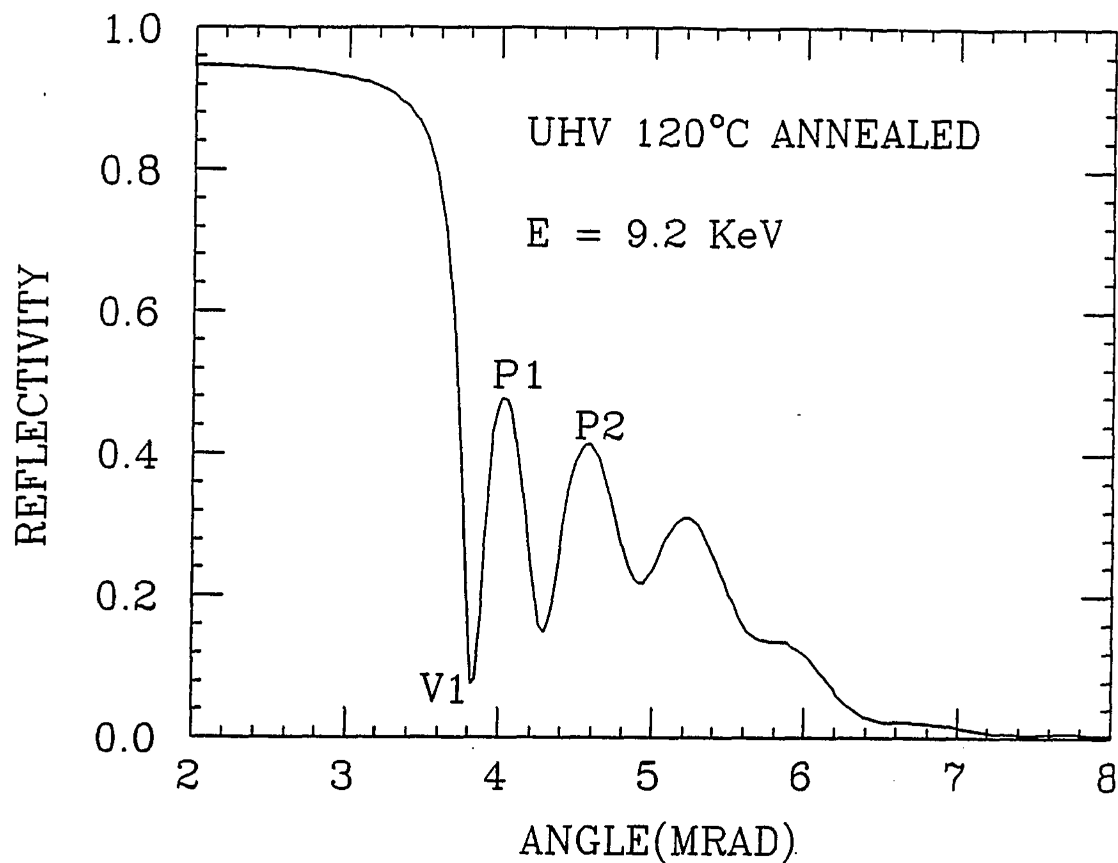

Figure 5.1: Reflectivity as a fucntion of the incident angle, from the UHV sample after annealing at 120°C. V1, P1 and P2 are the angles at which EXAFS was measured.

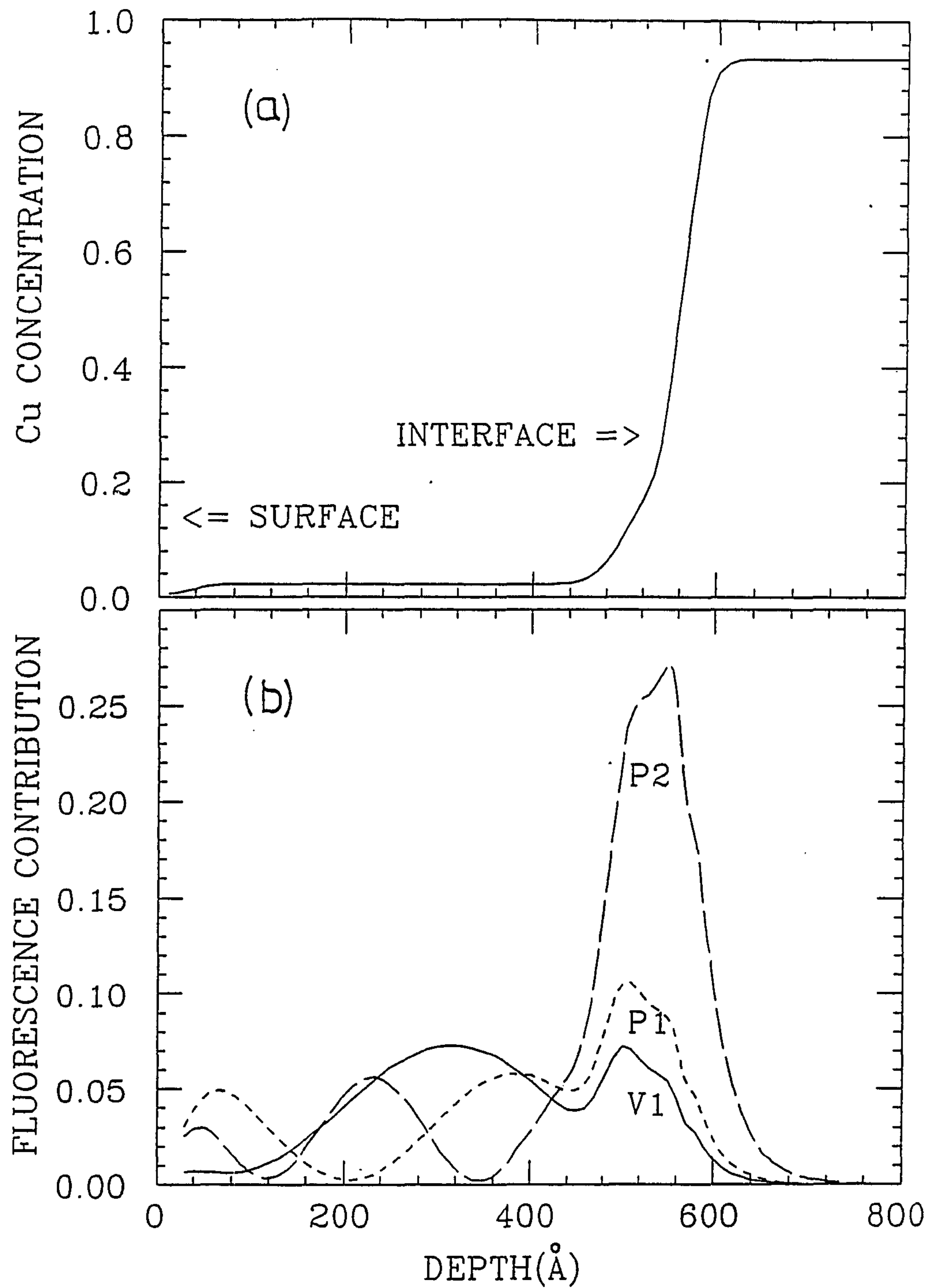

Figure 5.2: Model calculation of the fluorescence as a function of the depth into the sample (b), based on the model from the fitting to the reflectivity (a).

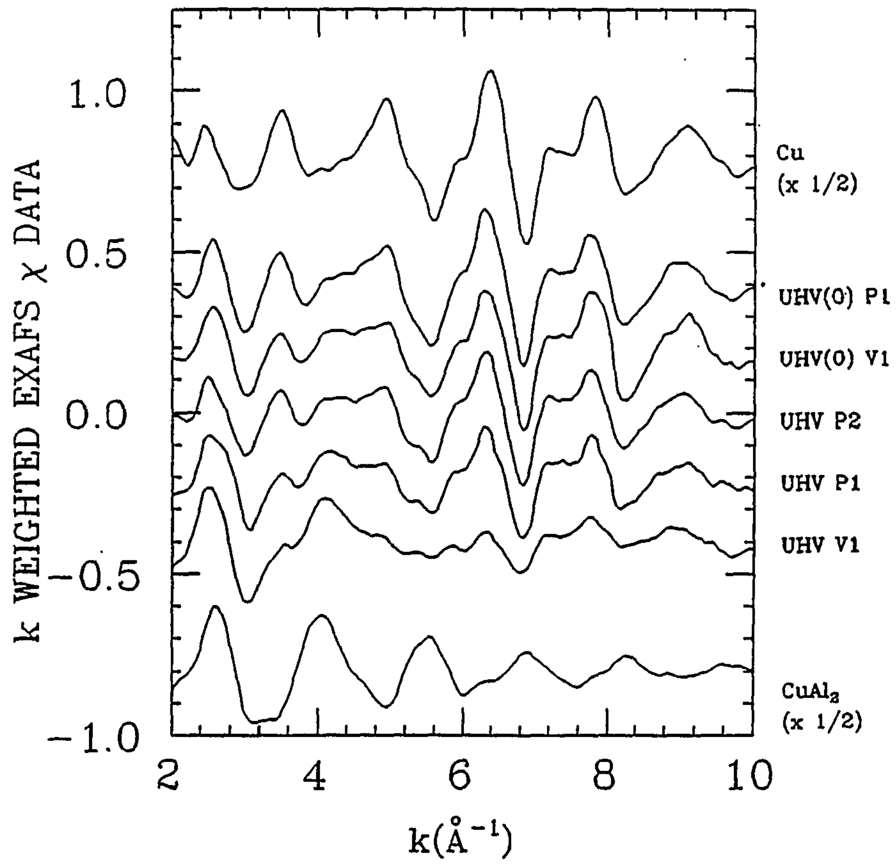

Figure 5.3: EXAFS from the UHV and UHV(O) samples as deposited, compared to the Cu and $CuAl_2$ standards

Fig.5.2). The degree of reaction is lower for the UHV(O) sample compared to the UHV sample at the same angle. However, the reflectivity results said that there is more Cu in the UHV(O) sample. It means that the Cu in the Al layer might not neccessary react with Al.

5.2.2 EXAFS Data As A Function of Annealing

Figures 5.4–5.6 are EXAFS obtained after each annealing, at angles V1, P1, and P2, respectively. The degree of reaction is persistently lower for the UHV(O) sample, up to 160°C anneal, although at higher temperature (above 140°C) anneals, the difference becomes smaller. This finding also agrees with the fitting to the reflectivity, which yields similar Cu distributions at higher temperature anneals.

5.2.3 Standard Analysis Procedure for EXAFS

There are many software packages for the EXAFS data analysis. The UW package ([51], [52]) and EXCURVE ([53]) were used in this work. The standard analysis procedure can be described as in following four steps (illustrated in Fig. 5.7). (Step (a) through (c) are performed with the UW package.)

(a) Background subtraction: The backgound of raw data μ is fitted with a pre-edge background (absorption due to the edges lower than the present edge, falls off as $1/E^3$), as well as a post-edge background μ_0 (the same as pre-edge, except for an addition of the step, $\Delta\mu$). The two backgrounds are removed from the data. The data then is normalized to the step. This step yields EXAFS χ data:

$$\chi = \frac{\mu - \mu_0}{step} = \frac{\Delta\mu}{step}$$

(b) Conversion from the energy space into k, the X-ray wave-vector, space. This gives the standard χ data which shows characteristic features from a

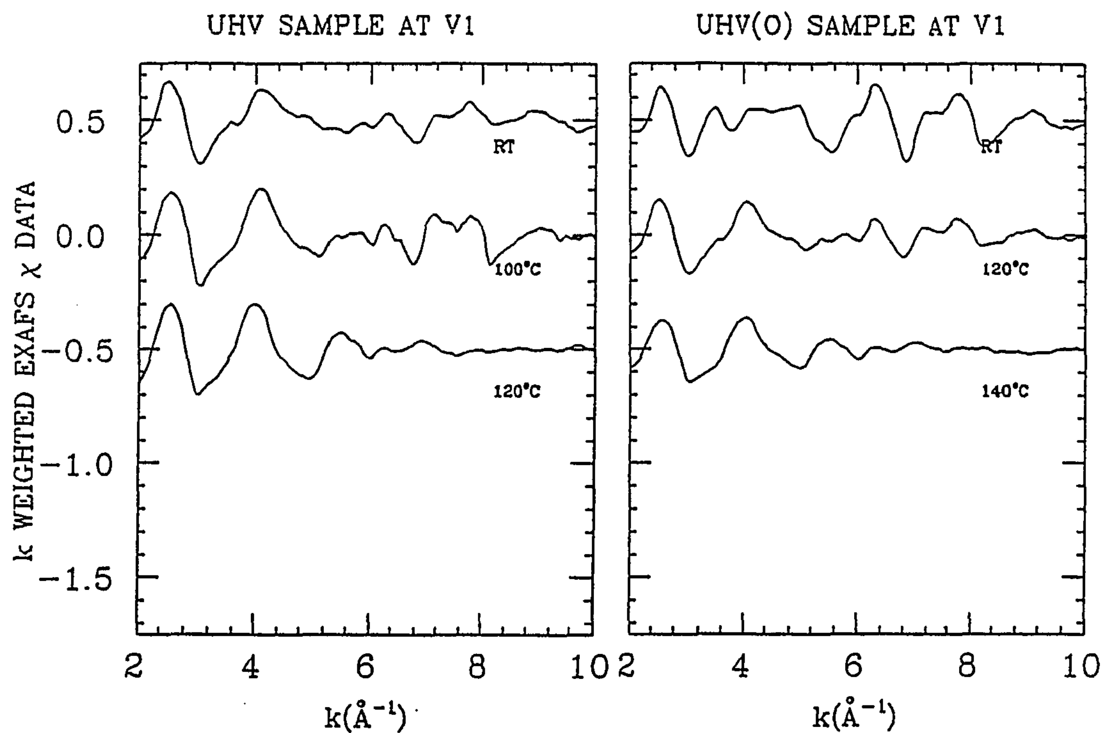

Figure 5.4: EXAFS taken at angle V1 from the UHV and UHV(O) samples, at various anneals.

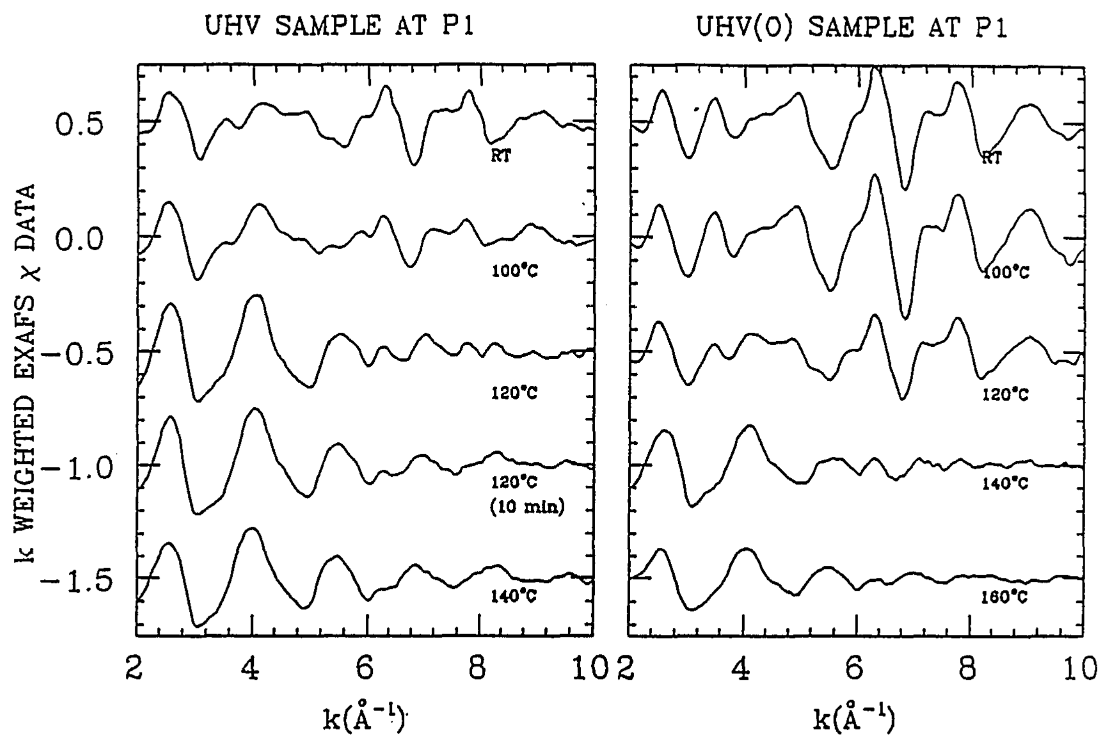

Figure 5.5: EXAFS taken at angle P1 from the UHV and UHV(O) samples, at various anneals.

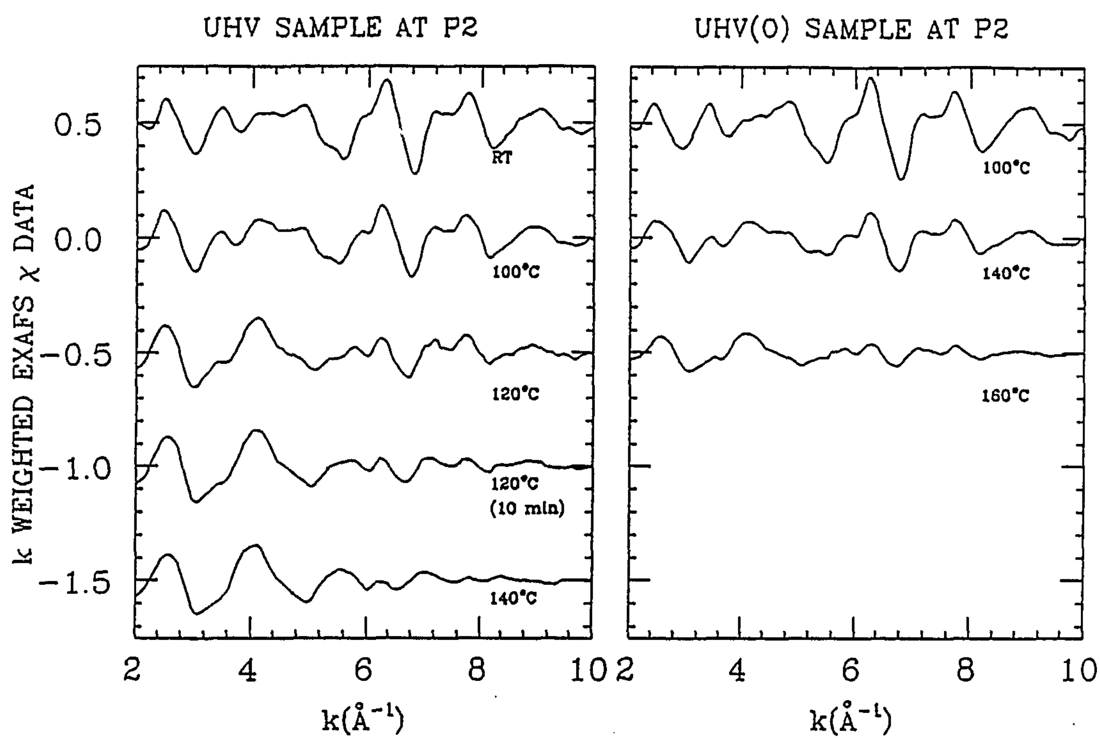

Figure 5.6: EXAFS taken at angle P2 from the UHV and UHV(O) samples, at various anneals.

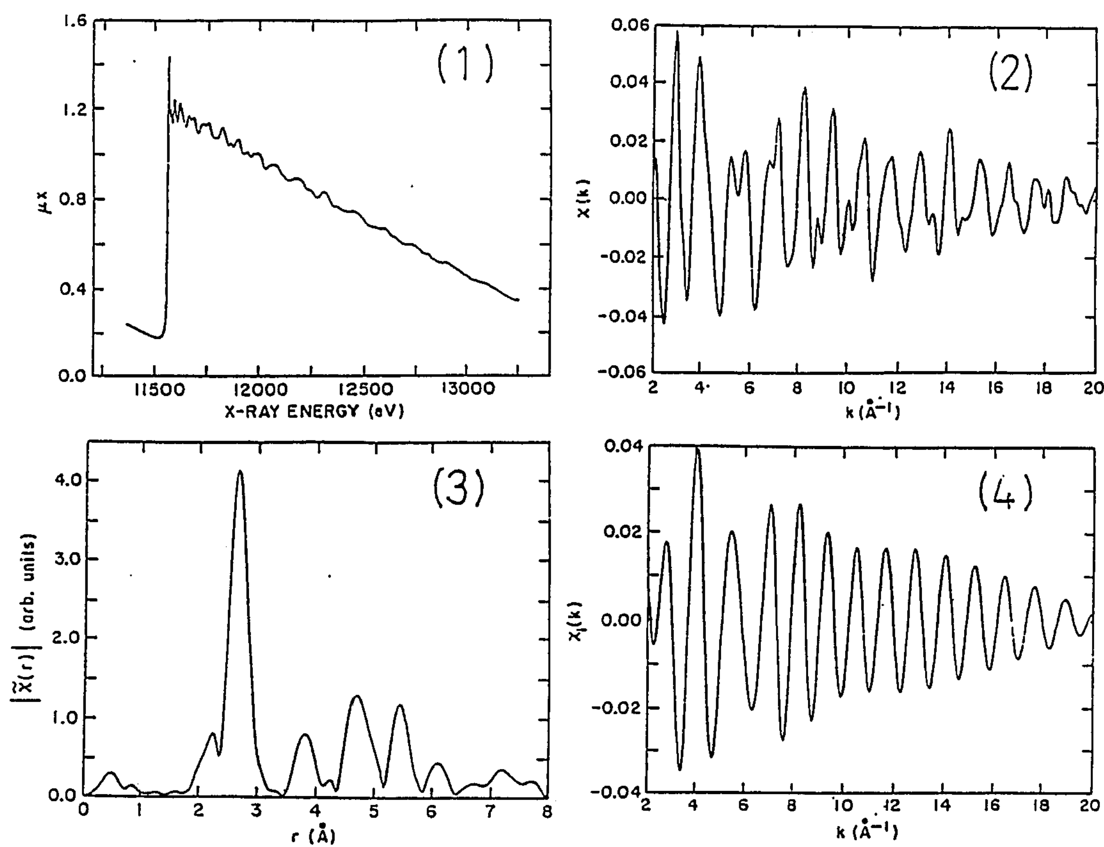

Figure 5.7: Standard EXAFS analysis procedure: (1) Raw data, (2) Background subtracted and converted to k-space, (3) Fourier-transformed, and (4) Backtransformed first shell data. From Reference [52].

material. Qualitative comparisons can be made at this level.

(c) The EXAFS data results from the interference between the photoelectron wave and the backscattered electron wave from the neighboring atoms. Relative to an absorbing atom, the neighbor atoms are in shell structure: the first shell, the second shell, etc. The various distances from the shells to the central atom result in interference of various frequencies. To separate these contributions, a Fourier transform for k is made. Since k is conjugate to the real space distance R, the amplitude of the transformed spectrum is related to the radial distribution of shells around the absorbing atom. To simplify the analysis, the first shell contribution is isolated (which usually corresponds to the main peak in the Fourier transformed spectrum) and backtransformed to k space.

(d) Now we have a spectrum with a single frequency of oscillation because of the single distance involved. This spectrum is referred to as "first shell χ data". Quantitative analysis usually starts from this level. One can either construct a theoretical model with various approximations (e.g. muffin-tin model and curved wave approximation, used in the EXCURVE program developed at Daresbary), or use measured data from one or several known structures (the approach of the UW package), to simulate the data. This procedure provides the type and the number of atoms in the shell, and the distance of the shell. Both software packages are employed in this procedure, with EXCURVE being the dominant method. To compensate for the deficiency caused by oversimplified theoretical assumptions, a known structure (from the "standard") is used to correct the theoretical model. The calculated phase shifts of the central atom and the backscattering atom are refined to fit the known EXAFS, as well as the amplitude. These modified parameters then are used to fit the data from unknown structures. For

example, a typical Cu-Al interface data set contains contributions from Cu-Cu bonds and Cu-Al bonds. The number and the distance of these bonds are uncertain since the interface structure may not be the same as any standard compound. A Cu-Cu 2.56 Å shell obtained from pure Cu (fcc structure, 12 neighbors) is used to calibrate the phase shifts of the central Cu atom and the backscattering Cu atom. A Cu-Al 2.60 Å shell obtained from $CuAl_2$ alloy , which has eight Cu-Al bonds at 2.60 Å and two Cu-Cu bonds at 2.44 Å (subtracted), is used to calibrate the Al backscattered atom phase shift. Once these two "standard" shells are determined, they can be used to fit the Cu-Al interface data. Now the phase shifts are fixed, but the amplitude and the distance are varied. If $CuAl_2$ is formed, the fit should reconstruct the structure with two 2.44 Å Cu-Cu bonds and eight 2.60 Å Cu-Al bonds. The accuracy of the fitting is usually ±1 for N (number of bonds) and ±0.01 - 0.03 for R (distance).

These procedures are designed for EXAFS data from direct measurements. When applied to indirect measurements, such procedures often do not yield correct answers. In particular, when measured at glancing angles, one has to consider the anomalous dispersion effect.

5.3 Anomalous Dispersion Correction (ADC)

5.3.1 The Anomalous Dispersion

The anomalous dispersion is associated with the photoabsorption process. When the X-ray energy is at an absorption edge, there is a sudden increase in the absorption coefficient μ. At this "abnormal" point, all optical constants of the concerned material experience a discontinuity as a function of the X-ray energy. Two of the optical constants most often referred to are β and δ, which represent the absorption and the scattering processes of X ray–matter interactions, respec-

tively. In this section, the optical constant β is also expressed in terms of μ, via $\mu = \frac{4\pi}{\lambda}\beta$. These two parameters, β and δ, together with the X-ray energy E and the incident angle θ, determine the indirect signals (such as the reflectivity and the fluorescence intensity) from a thin film at the glancing angle configuration. β and δ are related by the Kramers-Kronig integral [54]:

$$\delta(E_0) = \int_0^\infty \frac{\mu(E)}{E_0^2 - E^2} dE,$$

since the absorption and scattering processes are not independent of each other. If fine structures are observed in β (βEXAFS), they should also be observed in δ (δEXAFS), therefore, oscillations in the fluorescence and reflectivity signals are a superposition of the two types of EXAFS. One needs to extract βEXAFS, since a comparison to the EXAFS from a known structure (the "standard") is an essential step in performing the analysis. Note that the standard EXAFS is usually obtained from a direct measurement (which does not depend on δ). Unless the standard can be made into a thin film and is measured under the same angle (so that the EXAFS has same dependence on β and δ), the discrepancies between the fluorescence or reflectivity EXAFS and the standard will remain. Due to technical limitations (such as oxide on the surface), using thin film standard is impratical.

5.3.2 The Correction Procedure

The distortion due to the anomalous dispersion effect can seriously reduce the amplitude of the EXAFS, which changes the coordination numbers. The distortion can also change the phase of EXAFS, which affects the bond lengths. To eliminate such distortion, one has to calculate the scattering factor of the X rays, which has a real (δ) and an imaginary (β) part. Calculations have been made of δ by inputing experimentally measured β, using Kramers-Kronig relations [34,35]. The difficulty lies in the large range of data required to complete

the Kramers-Kronig integral (theoretically an infinite range is needed). In view of the small oscillatory amplitude of the EXAFS (which appears as oscillations in β, written as $\Delta\beta$) compared to β, an approximation that vastly simplifies the correction method was proposed by Heald *et. al.* [44]. The correction is described as follows:

To obtain EXAFS from any indirect measurement of μ (non-transmission), one can establish a general relation between μ and a function G that describes the measurement, without regard to the specific form of G. That is:

$$\Delta G = \frac{dG}{d\mu}\Delta\mu \tag{5.1}$$

G can be the fluorescence or reflectivity, or any measured function, and $\mu = \mu_0 + \Delta\mu$, where $\Delta\mu$ corresponds to the EXAFS oscillations. ΔG is then the oscillation of the measured signal that corresponds to $\Delta\mu$.

For the fluorescence, it is convenient to write:

$$G = \mu F \tag{5.2}$$

where G is now the fluorescence data, and F stands for the x-ray intensity inside the film, which also is a function of μ and δ. The smooth part (i.e. their values without the superimposed EXAFS oscillations) of μ and δ can be calculated with a simple model [54], which thus determines the smooth part of F. The smooth parts are written as μ_0, δ_0 and F_0, respectively. Equation (5.2) is put into the right hand side of Equation (5.1), and a Taylor expansion made on $F(\mu, \delta)$ with respect to $\Delta\mu = \mu - \mu_0$ disregarding the second and higher-order terms, Equation (5.1) then becomes

$$\Delta G = (F_0 + \mu_0 \frac{dF}{d\mu})\Delta\mu \tag{5.3}$$

Equation (5.3) is normalized to F_0 and the "step" of μ_0, remembering that the

"standard" EXAFS is expressed as:

$$\chi = \frac{\Delta\mu}{step}$$

(5.1) can be further written as

$$\frac{1}{F_0}\frac{\Delta G}{step} = \chi(1 + \frac{\mu_0}{F_0}\frac{dF}{d\mu})$$

Defining $\chi' = \frac{1}{F_0}\frac{\Delta G}{step}$ as the fluorescence EXAFS (fluoEXAFS for short), the relation between the fluoEXAFS and EXAFS is:

$$\chi'(fluo.) = \chi(1 + \frac{\mu_0}{F_0}\frac{dF}{d\mu}) \tag{5.4}$$

Similar arguments can be made for the reflectivity EXAFS (reflEXAFS). Then, replacing G by the measured reflectivity R, and $R = R_0 + \frac{dR}{d\mu}\Delta\mu$, and defining $\chi' = \frac{\mu_0}{R_0}\frac{\Delta G}{step}$ as the reflEXAFS, the counterpart of (5.4) for the reflEXAFS is:

$$\chi'(refl.) = \chi(\frac{\mu_0}{R_0}\frac{dR}{d\mu}) \tag{5.5}$$

A detailed calculation regarding F and R is discussed in Appendix B.

5.3.3 An Example of ADC: EXAFS from An Au Thin Film

The best way to convince ourselves that the correction is appropriate is to check it with a known system. Measurements were performed on a thin film of Au evaporated on float glass. Au was chosen because it is very stable and does not oxidize in air. Following the procedures described in 5.3.2, both fluoEXAFS and reflEXAFS data were corrected [55]. Comparison were made to the standard (Au foil) data from direct measurements. Figure 5.8 shows that the fluoEXAFS data after ADC are in good agreement with the standard, within experimental error. Therefore, the correction has served its purpose.

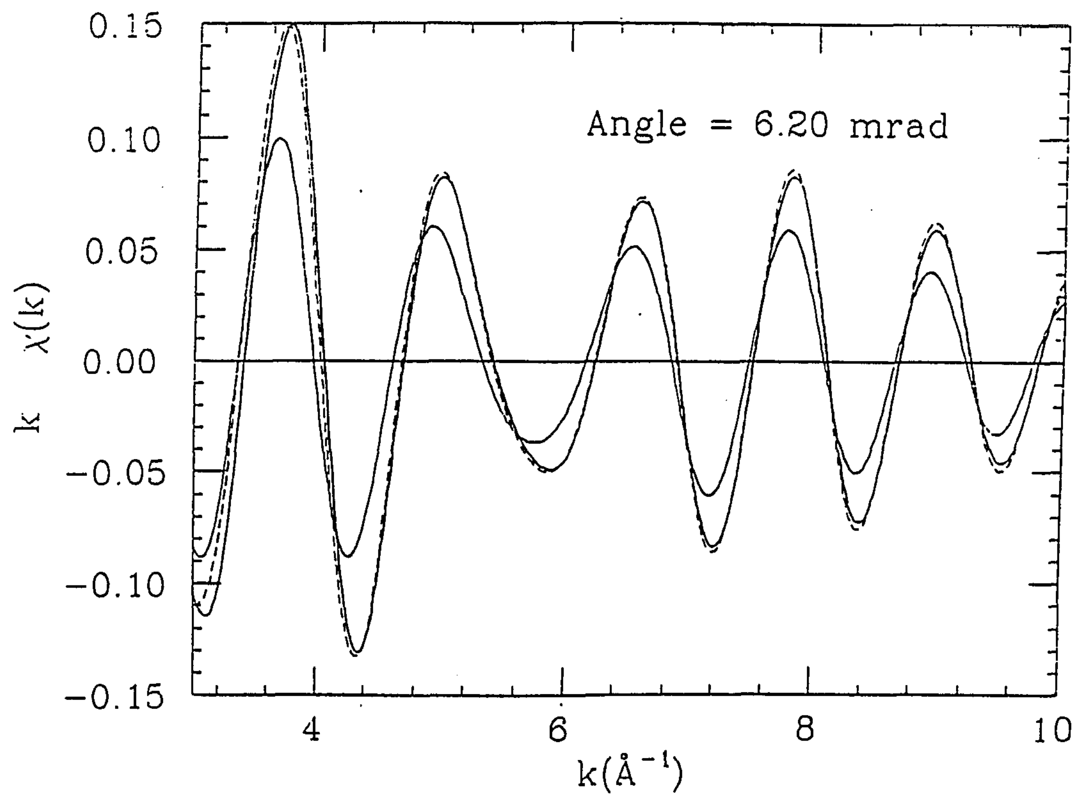

Figure 5.8: fluoEXAFS from a Au thin film, before (solid line, smaller amplitude) and after (solid line, larger amplitude) ADC, compared to the standard from a transmission measurement of an Au foil (dashed line).

5.3.4 ReflEXAFS

When applying ADC to reflEXAFS, special attention is required since the situation is more complicated than the fluoEXAFS. Since reflEXAFS is not the primary method for obtaining structural information in this work, interested readers are referred to Appendix D. For a reference on previous work see [26].

5.4 Quantitative Results

The models obtained from fitting to the reflectivity data (Chapter 4) are used in applying the ADC procedure. In the case of fluoEXAFS, the smooth function F_0 and $\frac{dF_0}{d\mu}$ are calculated. In reality, the models often consist of three or more layers due to interfacial mixing. The ADC assume that the $\Delta\mu$ part is approximately the same in all layers. This assumption holds for the two extreme cases: a very thin interface region or very thick one. For the intermediate case, the correction might introduce some errors.

Figure 5.9 shows the ADC for the first shell data from the Al/Cu UHV(O) sample (unannealed). The fitting results are shown in Figure 5.10. Further examples are shown in Figures 5.11-5.13, from the UHV(O) sample (120°C annealed) at all three angles. Table 5.1 summarizes the results from all annealings measured at various angles.

As expected, N_{Cu-Cu} increases as the X rays penetrate deeper, namely, as the incident angle advances from V1, P1, to P2; N_{Cu-Al} decreases accordingly (Table 5.1 from left to right). As the annealing temperature increases, the mixed regions expands. From the same angle, the X rays see less Cu-Cu contribution than the previous anneal and more Cu-Al contribution (Table 5.1 down). It is useful to compare the two samples, UHV and UHV(O), at the same temperature and the same angle. In agreement with qualitative observations in all cases, there is a greater Cu-Cu contribution and less Cu-Al contribution for UHV(O) than

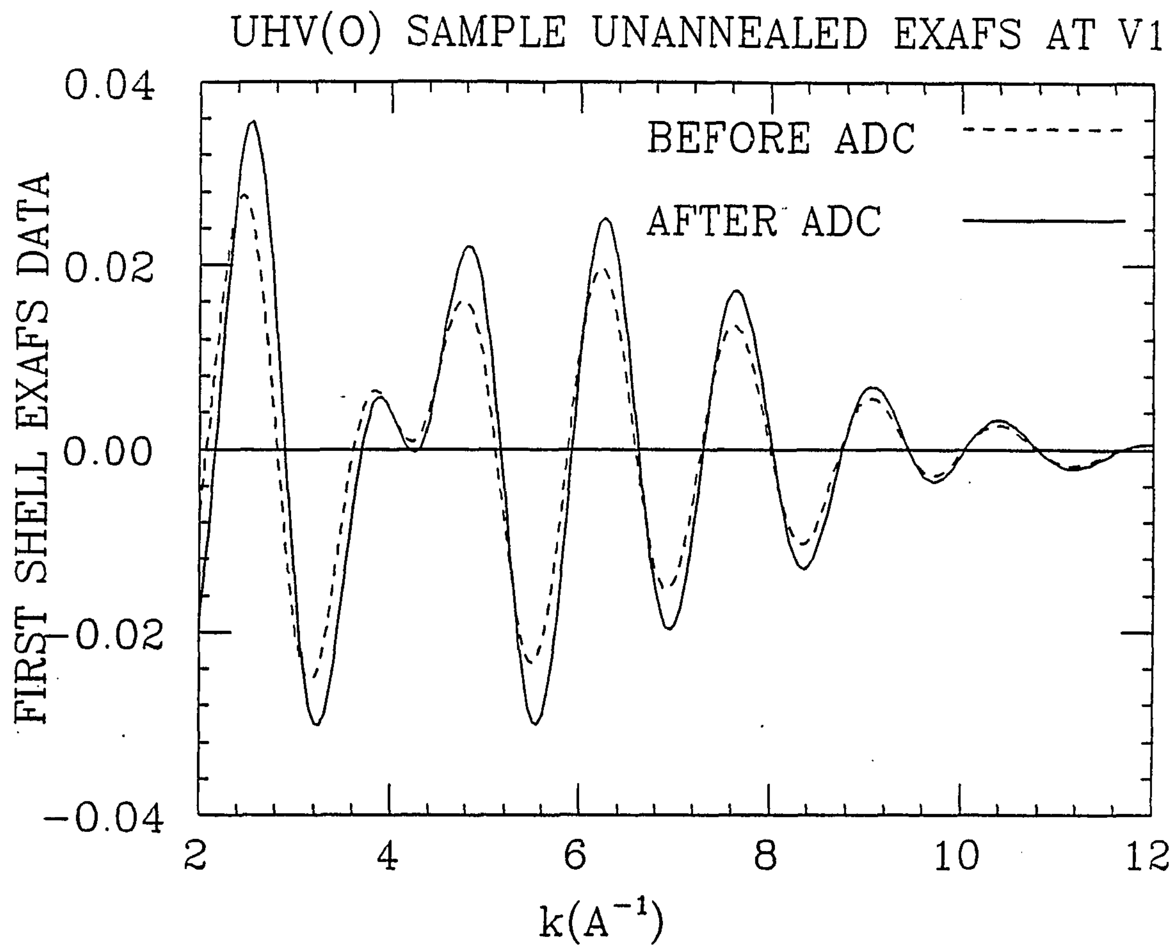

Figure 5.9: Examples of Al/Cu UHV(O) sample first shell data (unannealed) at V1 before and after the ADC.

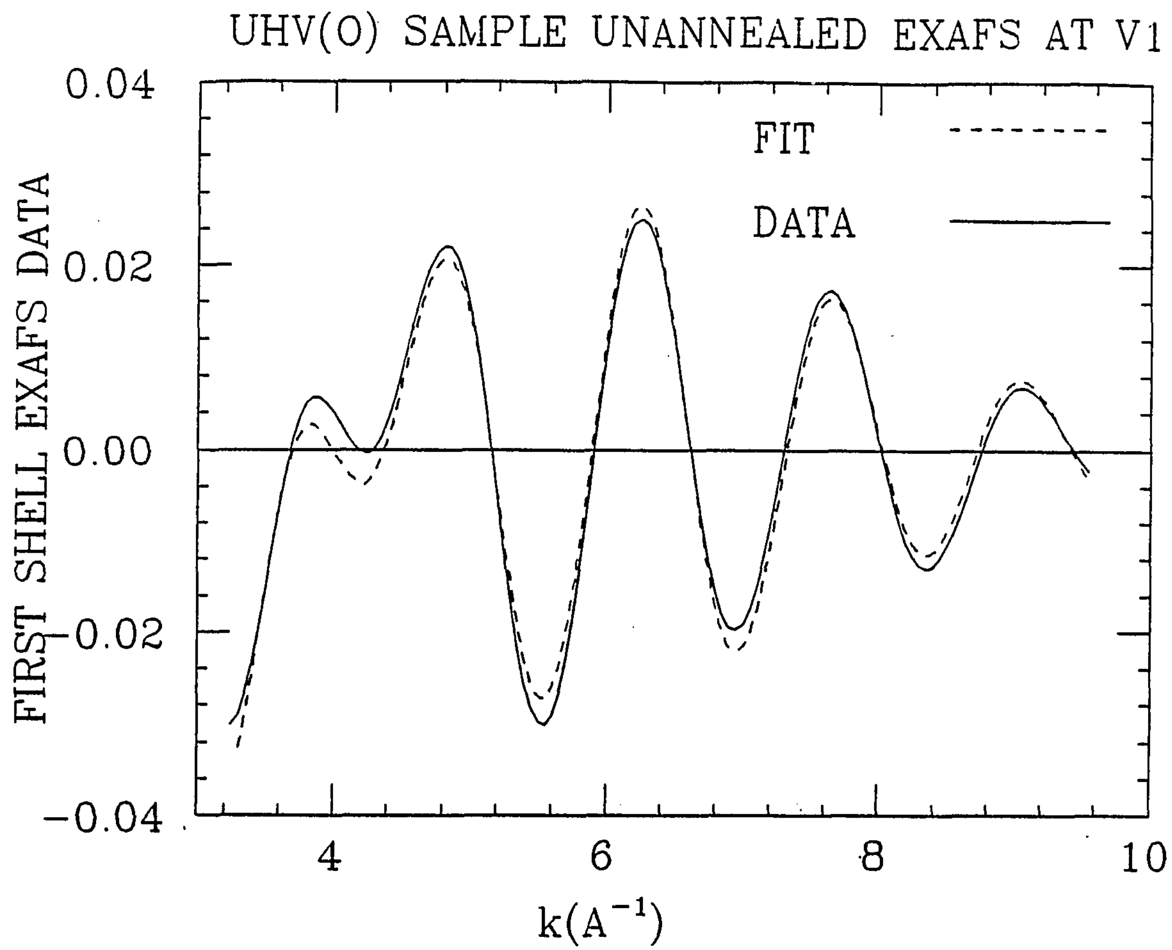

Figure 5.10: EXCURVE fitting results of the data shown in the previous figure. Solid line: data, dashed line: fitting.

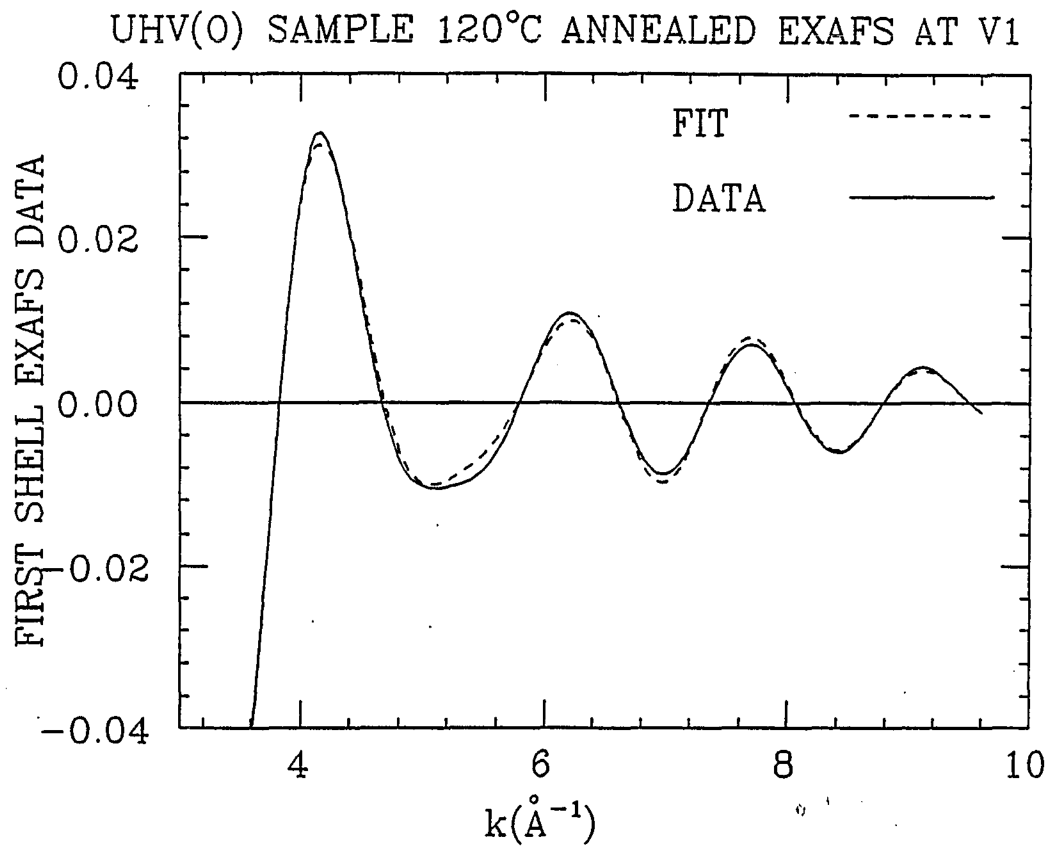

Figure 5.11: EXCURVE fitting results of the data, UHV(O) 120 degrees annealed, at angle V1

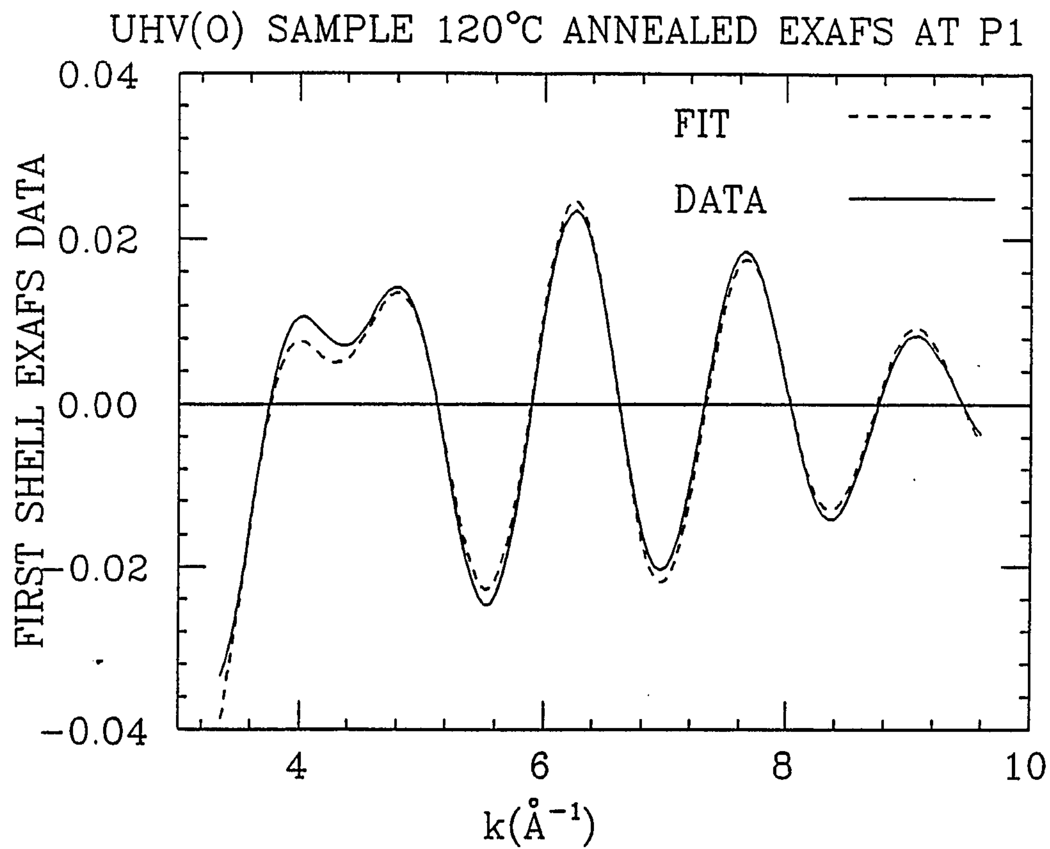

Figure 5.12: EXCURVE fitting results of the data, UHV(O) 120 degrees annealed, at angle P1

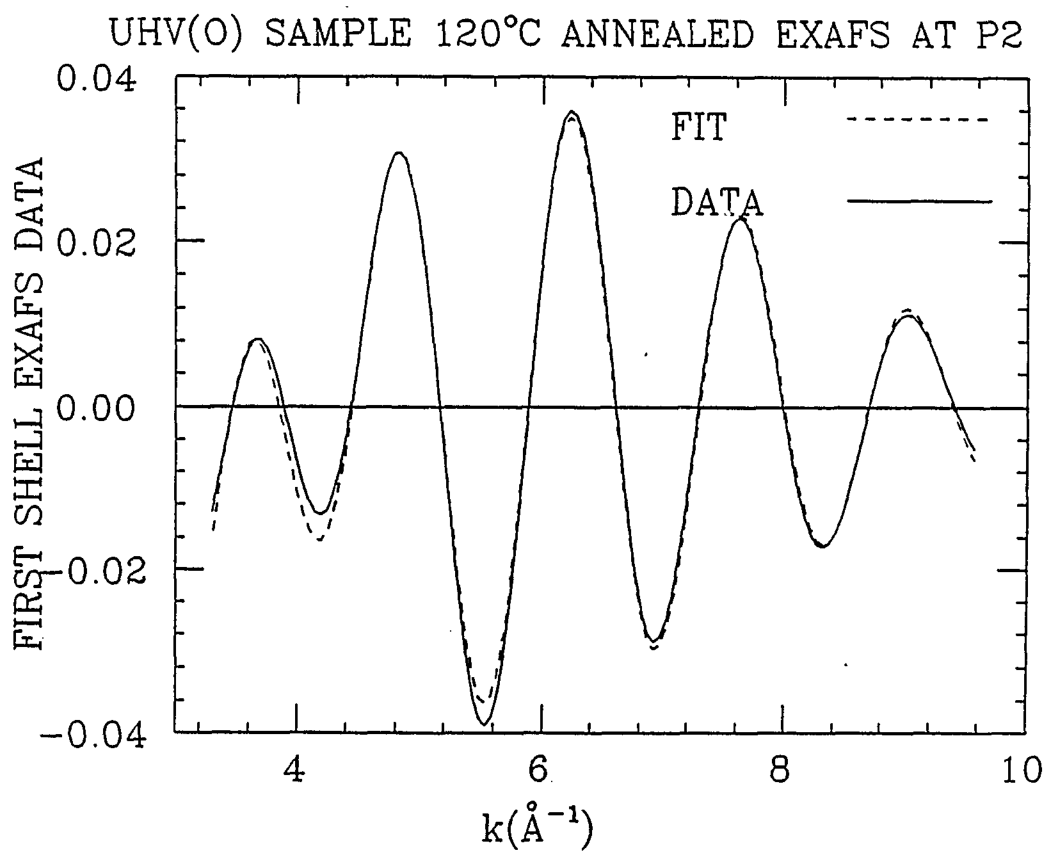

Figure 5.13: EXCURVE fitting results of the data, UHV(O) 120 degrees annealed, at angle P2

Table 5.1: Fitting results of the EXAFS first shell data

Sample	Angle→	V1			P1			P2		
(Anneal)	Bond↓	N	R	σ^2	N	R	σ^2	N	R	σ^2
UHV(O)	Cu-Cu	8	2.55	0.021	9	2.56	0.018			
(RT)	Cu-Al	3	2.55	0.022	2	2.55	0.022			
	Cu-Cu									
UHV(O)	Cu-Cu				10	2.56	0.018			
(100°C)	Cu-Al				3	2.58	0.022			
	Cu-Cu									
UHV(O)	Cu-Cu	4	2.55	0.018	6	2.55	0.016	8	2.57	0.017
(120°C)	Cu-Al	6	2.55	0.020	4	2.56	0.023	2	2.56	0.022
	Cu-Cu	1	2.47	0.016						
UHV(O)	Cu-Cu	2	2.63	0.018	2	2.56	0.017	6	2.56	0.018
(140°C)	Cu-Al	7	2.54	0.023	7	2.55	0.023	5	2.54	0.023
	Cu-Cu	3	2.45	0.016	1	2.46	0.015	1	2.43	0.015
UHV(O)	Cu-Cu				0	2.56	0.019	3	2.57	0.017
(160°C)	Cu-Al				6	2.55	0.023	6	2.51	0.023
	Cu-Cu				2	2.47	0.016	2	2.42	0.016
UHV	Cu-Cu	5	2.56	0.017	6	2.57	0.021	8	2.57	0.021
(RT)	Cu-Al	4	2.57	0.020	3	2.57	0.021	2	2.56	0.021
	Cu-Cu									
UHV	Cu-Cu	4	2.55	0.017	4	2.56	0.016	6	2.57	0.016
(100°C)	Cu-Al	8	2.56	0.023	5	2.57	0.023	3	2.56	0.023
	Cu-Cu									
UHV	Cu-Cu	1	2.61	0.017	3	2.63	0.017	4	2.58	0.017
(120°C)	Cu-Al	10	2.52	0.022	11	2.54	0.022	7	2.54	0.021
	Cu-Cu	3	2.43	0.014	4	2.45	0.014	2	2.45	0.015
UHV	Cu-Cu				0	2.56	0.017	2	2.56	0.017
(120°C)	Cu-Al				8	2.54	0.020	6	2.52	0.020
(10min)	Cu-Cu				2	2.44	0.016	1	2.44	0.016
UHV	Cu-Cu				0	2.56	0.017	1	2.56	0.019
(140°C)	Cu-Al				9	2.56	0.022	7	2.52	0.022
	Cu-Cu				2	2.45	0.016	1	2.43	0.016
UHV	Cu-Cu				0	2.56	0.017			
(160°C)	Cu-Al				9	2.56	0.020			
	Cu-Cu				3	2.45	0.016			

UHV, suggesting that the UHV(O) interface is less reactive than the UHV one.

As discussed in the EXAFS analysis procedures, if $CuAl_2$ forms at the interface, the ratio of N_{Cu-Cu} to N_{Cu-Al} should approach 2:8, with the bond lengths of 2.44 Å and 2.60 Å, respectively. At higher temperature anneals, the first condition seems to be satisfied, but the latter not observed. There are two possibilities: One is that $CuAl_2$ is not formed, the other is that there are other phases which reduce the average Cu-Al distance. The latter is the more probable. This question is further discussed in Chapter 7.

Chapter 6

STUDIES USING COMPLEMENTARY TECHNIQUES

Several studies using the various tools mentioned in Chapter 1 were made on the Cu-Al thin film samples. They were used to assist in interpreting or confirming the glancing angle X-ray studies. Despite their limitations, these techniques provide valuable complementary information.

6.1 Rutherford Backscattering Spectroscopy (RBS)

In the RBS study, an energetic charged particle beam (2 MeV He^{++}) is sent into the thin film at near normal incidence. Due to the Coulomb interaction, the ions are backscattered by the nuclei in the sample. By measuring the energy and the amount of the backscatted ions, one can derive the concentration and the location of the scatterer, and from this information the composition profile of the sample can be determined [57]. Figure 6.1 is an RBS measurement done on the UHV unannealed sample (performed by the IonX company). A fit wiht a theoretical model shows the layered structure in the film. There is a small amount of Cu throughout the Al layer, which is in agreement with the results of the glancing angle X-ray reflectivity fitting. However, it is not clear what the

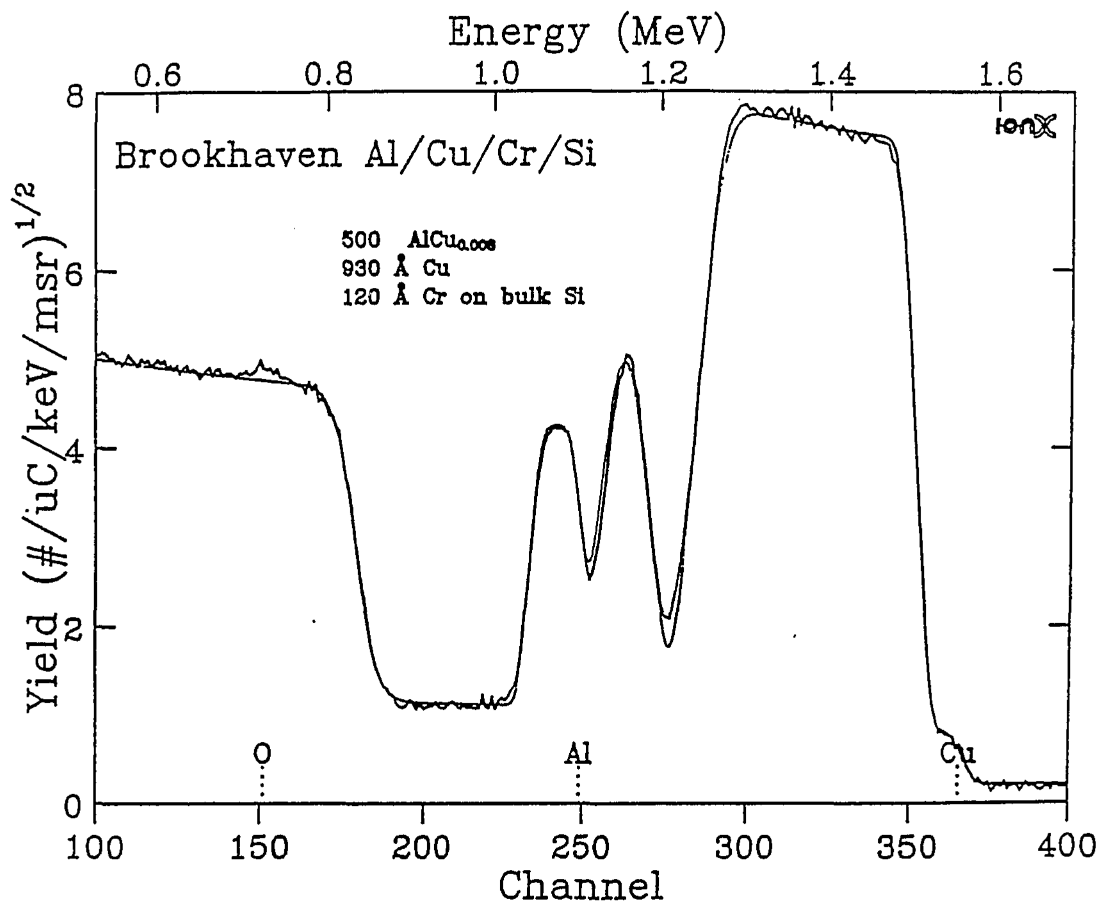

Figure 6.1: RBS on UHV unannealed sample

interface is like because of the small reaction region at room temperature. The typical depth resolution of this technique is 200 Å. With the glancing angle X-ray technique, the initial reaction was revealed (see Ch.4).

6.2 Transmission Electron Microscopy (TEM)

TEM pictures were obtained from the samples prepared by HV evaporation and by RF sputtering (Fig. 3.6). They clearly show the film's quality and the interface sharpness. The HV-evaporated sample has a sharp interface and large grains, while the sputtered sample has a very rough interface and fine grains. These features might explain that a higher degree of reactions was detected (Ch.4) for the sputtered sample. Since at the temperatures used in this study the reaction is mainly due to grain boundary diffusion, finer grains enable quicker diffusion. The vacuum condition also could be a factor [59]. Due to the technical difficulty in preparing samples for TEM (involving ion milling and glueing), attempts with the UHV samples failed. Thermal annealing during the glueing process ($\sim$ 120°C) and from ion milling also add uncertainty to the interface mixing, especially for the UHV-prepared samples which react at lower temperatures. In all of the UHV samples a large amount of mixing was observed, probably due to the preparation. A new LN_2 stage for the ion mill may allow these samples to be measured in the future. Nevertheless, TEM provides a visual picture of the sample. Where there was sufficient compound formed, selected-area-diffraction can be used to identify phases. Unfortunately there was no evidence of any phase other than Cu and Al in the samples successfully prepared. The interface may be too disordered for strong diffraction. For a reference on TEM studies of thin films see, for example, [58].

6.3 Auger Electron Spectroscopy (AES)

The AES technique includes two processes: First the sample surface is sputtered with ion bombardment to expose the subsurface. Then an electron beam is sent in to excite Auger electrons from the exposed surface. The Auger signal contains information on the types of atoms and on the chemical bonding state, and only comes from a small depth below the surface (determined by the electron escape depth, typically 20 Å). Therefore, knowing the sputtering rate, the composition as a function of the depth can be determined [6]. Figure 6.2 shows an AES profile of on a Cu-Al bilayer. For all three catogories, HV-evaporated, sputtered, and UHV-evaporated, the concentration profile reveals layer structures. The Al concentration in the Cu layer is found to be unrealistically high (contradicting the RBS results), and is probably due to the energy resolution of the Auger probe. The Al LVV Auger transition gives an Auger electron with kinetic energy $\sim$ 68 eV, and the Cu 3p Auger electron is $\sim$ 59 eV. The energy scan for the Al Auger peaks inside the Cu layer shows a shift to $\sim$ 62 eV, but at the mixed region it is $\sim$ 68 eV: this is an evidence for the misidentification of Cu as Al. It suggests that the possible chemical bondings between the Cu and Al in the mixed region do not give observable shift in the Auger peaks: this is a difficiency of the AES technique for studying Cu-Al system. Moreover, although masked by the reasons stated above, the reliability of this study is also limited by the sputtering effect in which the surface substance is driven into the bulk and detected as if it is a local substance. AES is a good technique for locating light elements such as oxygen which are not easily sensed by the X-ray technique. However, our results of AES sutdies were too inconsistent to allow us to reach any turther conclusions about the samples. There are *in situ* studies on Cu-Al interfaces [60], which can reveal monolayers of reaction. Similar to the XPS, the type of measurement might not be ideal for comparing to the *ex situ* studies.

RT

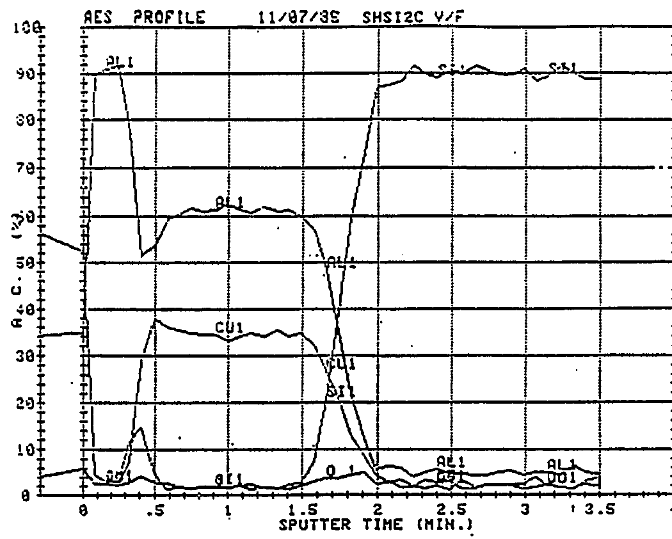

180

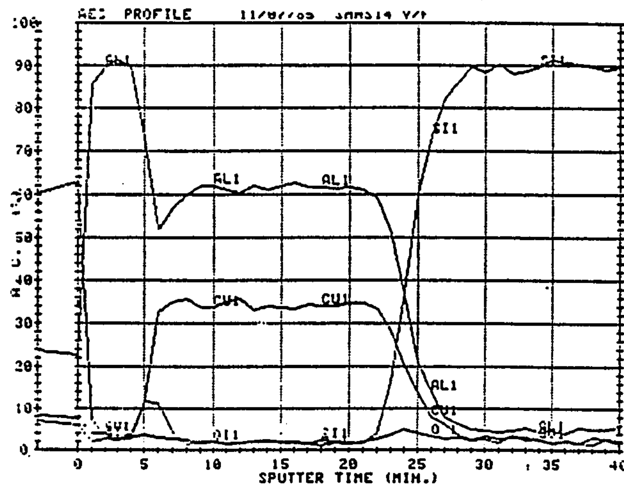

220

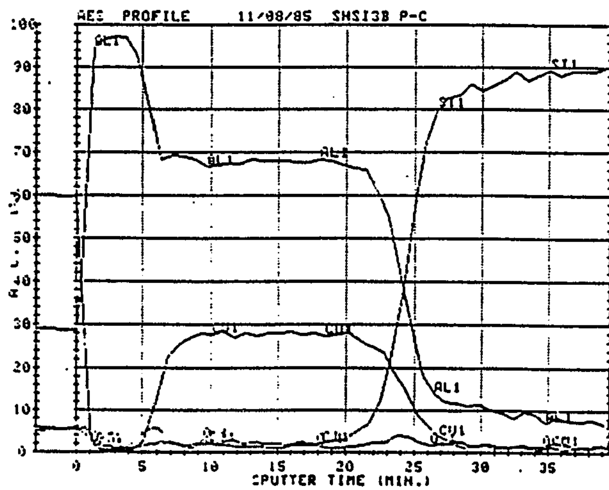

Figure 6.2: AES on HV sample

6.4 X-ray Photoemission Spectroscopy (XPS)

XPS detects photoelectrons emitted by X-ray excitation. The energy range for X-ray photons is a few tens to a few hundred electron volts. Photoemission occurs when electrons in a bond state are excited to higher states above the vacuum level, which are collected and analyzeed according to their kinetic energies. The energy distribution curve (EDC) reflects the initial electron density distribution: it can be used to determine the core-level state or the band structure, both of which are sensitive to chemical bonding [61]. The experiment is conducted in an UHV chamber, with a slow-rate deposition capability ($\sim$ 1 monolayer/min). The EDC is obtained after each monolayer is deposited, so that the layer growth features can be studied. A layer grown in this fashion (allowing 10- to 20- minute intervals between monolayers for doing measurements) might not be the same as one prepared for X-ray studies, which is deposited continuously. However, it gives us some idea of the initial interface formation at a monolayer scale.

The Cu-Al system was studied at beamline U-7B of the VUV ring of the NSLS [50]. In one study, Al was directly deposited on a thick film of Cu (on a Ta substrate). In the other, the Cu surface was exposed to 1000L oxygen exposure before Al deposition. In both cases, an initial reaction between Al and Cu was detected, as evidenced by a change of the shape of the Cu valence band (Fig.6.3), as well as a shift of the Al core level peak location (Fig.6.4).

The reaction can be identified by the feature at -4.4ev in the valence level EDC. The behavior in these two cases was not the same: Al/Cu had slower reaction (the -4.4ev feature formed slower) than Al/O/Cu, but then the feature was buried faster in Al/Cu than in Al/O/Cu upon subsequent Al deposition. In the Al/O/Cu case, the feature persisted through out the whole deposition procedure (up to 30 monolayers). The core-level data should give a better hint of whether a compound (e.g. $CuAl_2$) was formed. Unfortunately, the Al 2p level

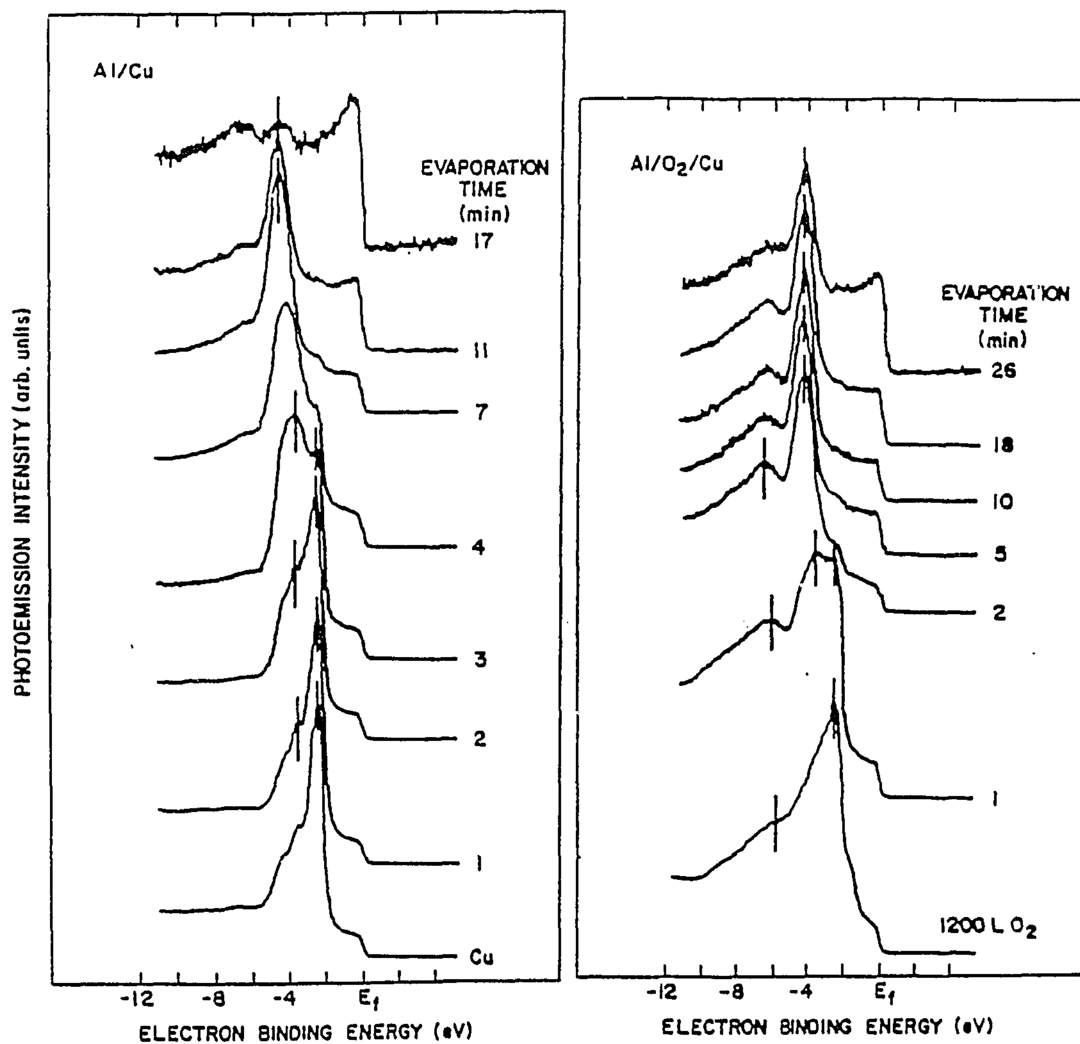

Figure 6.3: XPS data for the Al/Cu and Al/O/Cu valence bands as a function of Al evaporation time

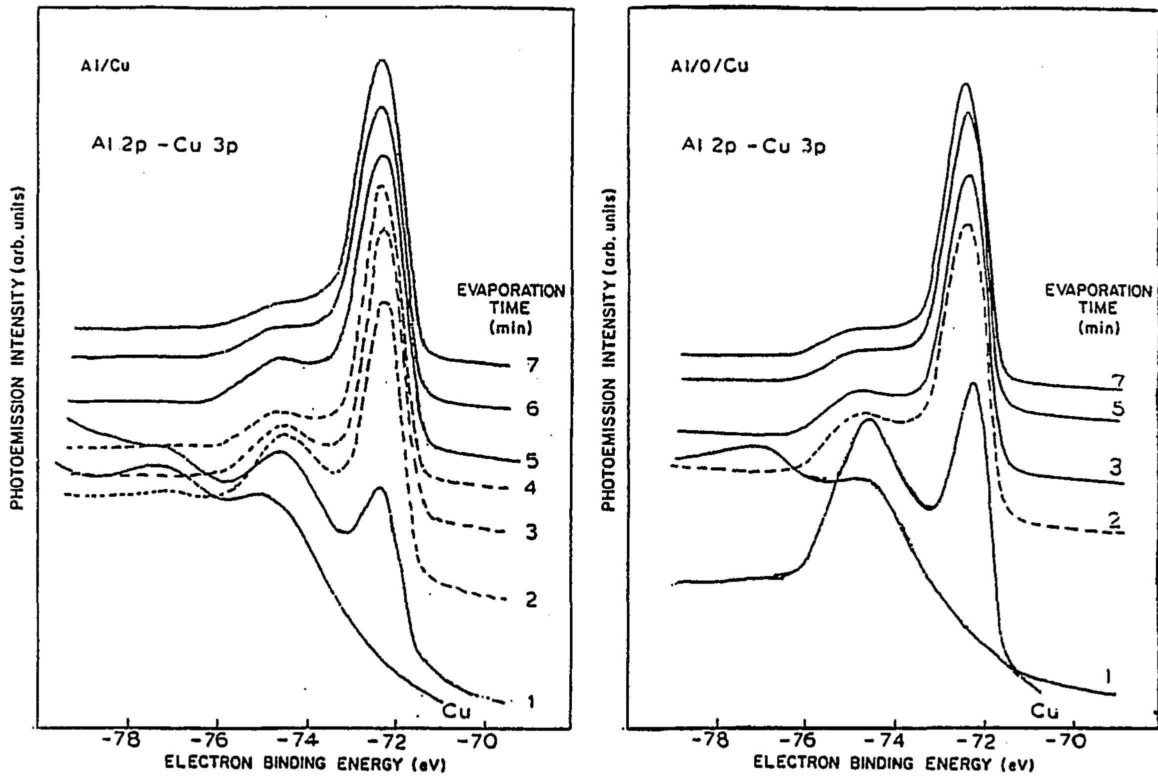

Figure 6.4: XPS data for the Al/Cu and Al/O/Cu core levels

in $CuAl_2$ has only a 0.4 eV shift away from that of the Al metal. The resolution of the measurement is not sufficient to unambiguously resolve such a shift. In the case of Al/Cu, the shift seemed to be more definite than in the Al/O/Cu case. It is hard to determine what happened at the interface of the Al/Cu and Al/O/Cu, except that there was change from the unmixed state (the Al/Cu results are in agreement of another study [43]). Further studies on the annealing behavior (the sample was heated after the final deposition of Al) indicate that there is a new phase forming at the Al/Cu (see Fig. 6.4), marked by two extra peaks on the higher energy side. But such a phsae does not occur for the Al/O/Cu, suggesting that oxygen enhanced the initial mixing during deposition, but hindered the reaction induced by thermal annealing. In the X-ray reflectivity study, a larger mixed region is obtained for the UHV(O) sample. But the EXAFS study shows that the Cu-Al bonds are fewer in the UHV(O) sample. The X-ray results agree with the photoemission results provided that the larger mixed interface region is not chemically reacted. Considering the different scales and different conditions of the studies, direct comparison is difficult.

Chapter 7

DISCUSSION

By combining the results from the reflectivity and the EXAFS analysis, an average interface location can be derived. The reflectivity fitting gives a model of the density profile, and the EXAFS analysis gives local structural information. Where exactly "local" area is located depends on the X-ray intensity distribution inside the film. The intensity distribution (I_f vs depth) can be calculated using the model of the density profile shown in Figure 5.2(a). The total EXAFS contribution from various depths is represented by the area under the intensity curve in Figure 5.2(b). A larger value of I_f means a larger contribution to the EXAFS from the corresponding depth. Besides the interface location, the analysis also porvides information about film morphology and grain boundary diffusion under the influence of oxygen exposure.

7.1 An Average Position Of The Interface

The ratio of the number of Cu-Al to Cu-Cu bonds, $r = N_{Al}/N_{Cu}$, obtained from the EXAFS data is proportional to the ratio of the number of Cu-Al to Cu-Cu bonds excited by X rays. These bonds can be anywhere within the film. To determine where these bonds are located, some assumptions have to be made. Assume an average interface position x ($0 < x < d$, with 0 being the surface and d the total film thickness) (Fig.7.1), the areas under the I_f curve on either side

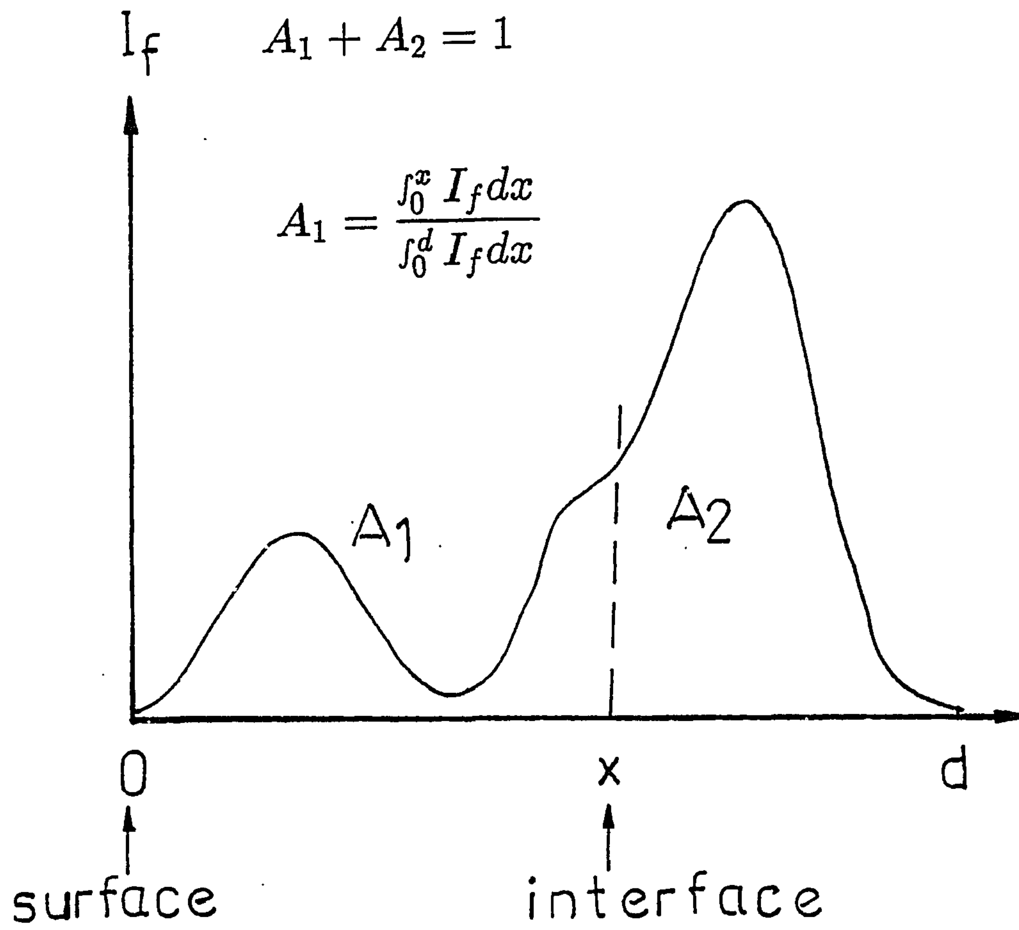

Figure 7.1: Areas on either side of the interface location, based on model calculations discussed in Chapter 5

of x (normalized to the total area) can be written as:

$$A_1 = \frac{1}{A}\int_0^x I_f dx \tag{7.1}$$

where A is the total area:

$$A = \int_0^d I_f dx,$$

and,

$$A_2 = 1 - A_1.$$

To start with a simple case, A_1 and A_2 represent the signals from Cu-Al and Cu-Cu bonds, respectively. Then, the ratio r is also equal to A_1/A_2. I will show later that a more complicated situation (wiht both Cu-Cu and Cu-Al bonds present in A_1 and A_2) also can be studied. Using:

$$r = \frac{A_1}{A_2} = \frac{A_1}{1 - A_1},$$

yields,

$$A_1 = \frac{r}{1 + r}. \tag{7.2}$$

The value of r is a function of incident angles, because different depths are probed at different angles. For each r there is an A_1. From the value A_1 the interface position x can be determined by solving for x in:

$$\frac{1}{A}\int_0^x I_f dx = \frac{r}{1 + r} \tag{7.3}$$

For a particular film measured at various angles, x derived from Equation 7.3 should give the same value, since x represents the physical location of the interface and should not depend on the angle at which the measurement is made. This correspondence is a good way of checking the accuracy of the model of the density profile, as well as the consistency of the EXAFS results. Table 7.1 lists the average interface position obtained at all three angles at which EXAFS were measured, for various annealings on the UHV(O) and UHV samples. The

Table 7.1: Location of the interface at various anneals obtained from the EXAFS ratio at angle V1, P1, and P2.

UHV(O)				UHV			
T(°C)	V1	P1	P2	T(°C)	V1	P1	P2
RT	310	3250	-	RT	460	460	500
120	386	366	386	100	520	520	530
140	320	410	420	120	530	530	550
160	-	438	428				

positions are also illustrated in Figure 7.2. Except for the data from the UHV(O) sample annealed at 140°C measured at angle V1 (marked by *), the interface can be localized to a precision of about 40 Å(the error bar of x is typically 10%). Compared to the resolution of other techniques (~200 Å for RBS and AES), the X-ray technique is superior. These results are obtained based on a simple assumption: that there is no Cu-Cu bond in A_1 and no Cu-Al bond in A_2. Whether this is an over-simplified model is discussed in the next section. The data point marked by * is probably due to an error in the EXAFS fitting. At this annealing temperature, the determination of the Cu-Cu component is uncertain at low angles due to the higher degree of reaction. The EXAFS result indicated a Cu-Cu bond of 2.60 Å, which is suspiciously large compared to the expected value of 2.56 Å. The coordination number given might also deviate from the true value. The error bar for r at this point is $\sim$ 30% (120Å).

7.2 Errors Caused By Various Factors

Despite the good precision of the data, the x values of the unannealed cases are unreasonably low compared to the values of the nominal interface locations (400 Å for UHV(O) and 500 Å for UHV, obtained from fitting to the reflectivity data). The error is likely to be caused by underestimating the amount of Cu-Al bonds in the experimental data. There are four possible factors that can contribute to underestimating the Cu-Al bonds: (1) Disordered Cu-Al bonds from grain boundaries (GBs) which contribute little or nothing to the EXAFS signal; (2) Large-angle scattering which adds to the Cu-Cu contribution and reduces the ratio; (3) Oversimplified single-bond approximation; and (4) Deviation of the density model. These four factors are discussed individually.

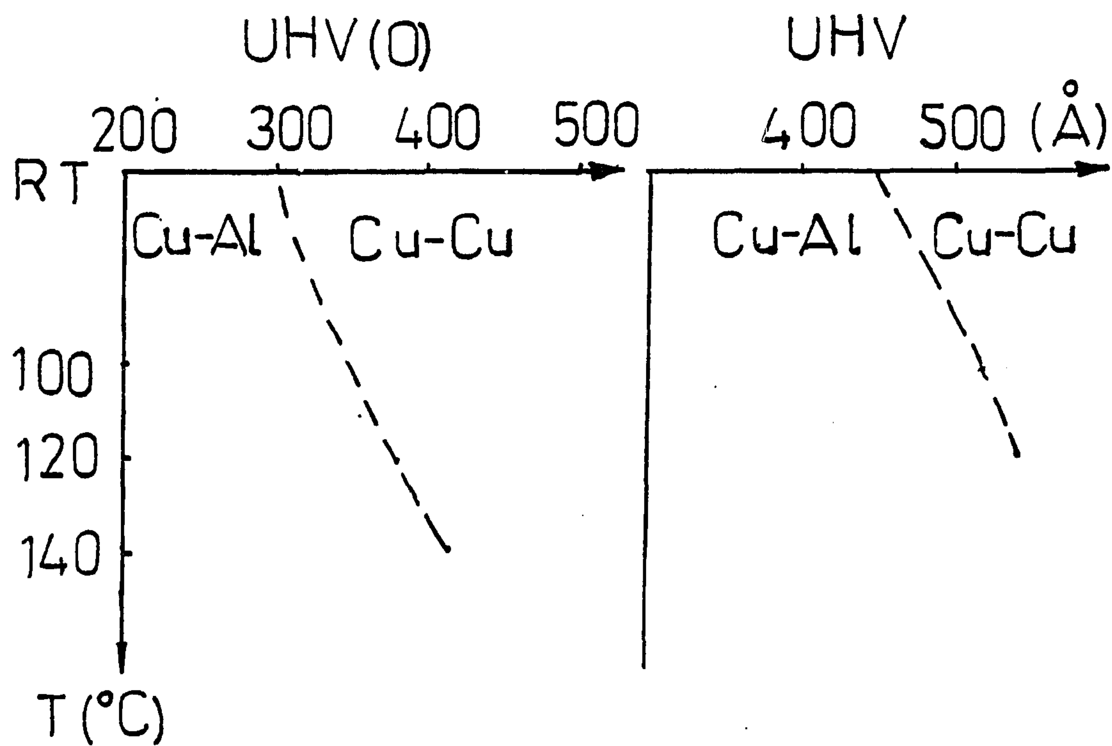

Figure 7.2: Movement of the interface as a function of anneals.

7.2.1 Consideration of GB Cu-Al Bonds

The Cu atoms diffusing into the Al grain boundaries do not neccessarily chemically react with the Al atoms. Therefore, there may be no single value that can describe the Cu-Al distance. In other words, the Cu-Al bonding is very disordered in the GB area, so that the Cu atoms contribute to the fluorescence step but not to the EXAFS. Such a contribution reduces the amplitude of the Cu-Al EXAFS, giving a smaller average number of nearest neighbors. This effect was ignored in the previous section, which reduced the interface location (x value). A simple solution to this problem is to divide the area A_1 in Figure 7.1 into a GB region and a new region of Cu-Al bonds, at location x_1. The ratio r obtained from the EXAFS refers to the ratio of the new Cu-Al region to A_2. The dividing point, x_1, is determined by the consistency of the data from all three angles. The interface location x is obtained from a modified form of Equation 7.3:

$$\frac{1}{A}\int_{x_1}^{x} I_f dx = \frac{1}{1+r}\left(r + \frac{1}{A}\int_{0}^{x_1} I_f dx\right) \tag{7.4}$$

This consideration brings the interface closer to the nominal position. For UHV(O), x(P1) is increased by 95 Å for x_1=400 Å, and for UHV, x(P1) is increased by 60 Å for x_1=440 Å.

7.2.2 Consideration of Large-Angle Scattering

Large-angle scattering refers to the scattering of the primary X rays by atoms encountered on the path, causing the X rays to deviate from their original glancing angle incidence. Part of the scattered X rays go into the deeper part of the sample, causing fluorescence from the bulk. Since the bulk of the sample is a Cu layer, extra Cu-Cu bonds in their metallic form are added to the EXAFS signal. Quantitative estimation of the scattering is difficult, because of the experimental factors involved. One simple fact is that the ratio, r, is reduced due to extra

Cu-Cu contribution, δN_{Cu}:

$$r = \frac{N_{Al}}{N_{Cu} + \delta N_{Cu}}$$

The true ratio:

$$r' = \frac{N_{Al}}{N_{Cu}} = r(1 + \frac{\delta N_{Cu}}{N_{Cu}})$$

The difference:

$$\Delta r = r' - r = r\frac{\delta N_{Cu}}{N_{Cu}}$$

Δr leads to a change in A_1:

$$\Delta A_1 = \frac{\Delta r}{(1+r)^2}$$

(from Equation 7.2). ΔA_1 in turn causes a change in x, which can be calculated as follows: Assume:

$$\int_0^x I_f dx = x\bar{I}_{f1}$$

$$\int_x^d I_f dx = (d-x)\bar{I}_{f2}$$

where $\bar{I}_{f1}$ and $\bar{I}_{f2}$ are the average fluorescence intensities in area A_1 and A_2, respectively. Equation 7.1 can be written as:

$$A_1 = \frac{1}{A}\int_0^x I_f dx = \frac{x\bar{I}_{f1}}{x\bar{I}_{f1} + (d-x)\bar{I}_{f2}}, \tag{7.5}$$

Solving for x and differentiating x with respect to A_1, yields:

$$\Delta x = \frac{dx}{dA_1}\Delta A_1 = \frac{r_I x}{r_I + (1-r_I)A_1}\frac{\Delta A_1}{A_1}. \tag{7.6}$$

Assuming that 10% of the Cu-Cu contribution is due to the scattering – the 10% level is estimated by comparing the fluorescence step-height at $\theta < \theta_c(Al)$, where the Cu-Cu contribution is solely due to the scattering, to the step-height at larger incident angles, then $\Delta r = 0.1r$, using Equation 7.6 for the UHV(O) sample, the 10% scattering corresponds to ~ 20 Å reduction in x. Since the forward scattering is of most concern, we can expect the scattering to increase

as the angle increases. At the same time, the total signal also increases because the unscattered X-ray beam penetrates deeper to the sample. It is not whether the scattering or the total signal increases faster. If the scattering does, then x should suffer more reduction for P2 than for P1, for example. This reduction can explain the smaller x values for larger angles for the UHV(O) sample: At 120°C anneal, x(P2) is smaller than x(P1) by 10 Å; this difference suggests that the scattering contribution is 5% greater for P2 than for P1. In other words, if eliminating the 10% scattering at P1 and 15% at P2, then x(P1) can be moved from 435 to 455 Å, and x(P2) from 425 to 455 Å. This is an example of how scatterings affect the interface location. In the case of the 160°C anneal for the UHV(O) sample, the difference means a 20% increase in scattering for P2, which seems unreasonably large. Therefore, scattering alone may not account for the errors. It is not clear why the scattering has less effect on the UHV sample, but it might have something to do with the thickness and morphology of the film. The reacted region that contains Cu-Al bonds is much larger for the UHV sample than for the UHV(O). This difference might change the scattering pattern. Since the deviation due to the scattering effect is within the error bars, the scattering issue was not emphasized in this work. A 10% reduction in r, or $\Delta r = 0.1r$, is a reasonable guess.

7.2.3 Consideration of The Validity of The Single-Bond Assumption

Consider some relative amount of Cu-Cu bonding (δ_1) in A_1, and δ_2 Cu-Al in A_2: the interface is therefore relocated. The new location can be determined by finding the new A_1 and A_2 which satisfy the following relations:

$$r = \frac{A_1}{A_2} = \frac{A_1'(1-\delta_1) + A_2'\delta_2}{A_2'(1-\delta_2) + A_1'\delta_1} \tag{7.7}$$

where $A_1^{'}$ and $A_2^{'}$ are areas under the single-type assumption. By calculating the change from $A_1^{'}$ to A_1, the modified interface location can be determined. Equation 7.7 leads to a simple result:

$$A_1 - A_1^{'} = \delta_2 A_2^{'} - \delta_1 A_1^{'} \tag{7.8}$$

Equation 7.8 says that depending on the amount of the other type of bond, the interface can move to a larger or smaller value (when $\delta_2 A_2^{'} > \delta_1 A_1^{'}$, x increases; otherwise it decreases, as shown in Fig.7.3(a)). The amount of the movement (the distance of the new x from the original x (now $x^{'}$) under the single-type assumption) depends on the value of $A_1^{'}$, which is inversely proportional to the incident angle (X rays are more localized in the first half of the film at smaller incident angles). When moving towards the direction of increasing x, as shown in Figure 7.3(b), the amount of the movement is larger for a smaller angle (e.g. $\Delta x(P1) > \Delta x(P2)$), when moving towards the direction fo decreasing x, $\Delta x(P1) < \Delta x(P2)$.

To quantify the above argument, one can use Equation 7.6 to calculate the change in x due to the change in A_1. For a simplified situation ($\delta_2 = 0$), equation 7.8 becomes:

$$A_1 = -\delta_1 A_1$$

For this case, a typical example is given (using Equation 7.6): 10% of Cu-Cu bond ($\delta_1 = 0.1$) in A_1 results in a 40-Å increase in x for P1, and a 25-Å for P2. Since the error bar for x is typically 40 Å, this model does not discriminate whether there are 10% Cu-Cu bonds in A_1, or none. In other words, there might be a 10% contribution from Cu-Cu bonds in A_1. A more realistic situation might be that there is an equal number of Cu-Cu bonds in A_1 and Cu-Al bonds in A_2 due to interdiffusion at the interface. The two terms on the right hand side of Equation 7.8 tend to cancel out. The net effect on the interface location is very

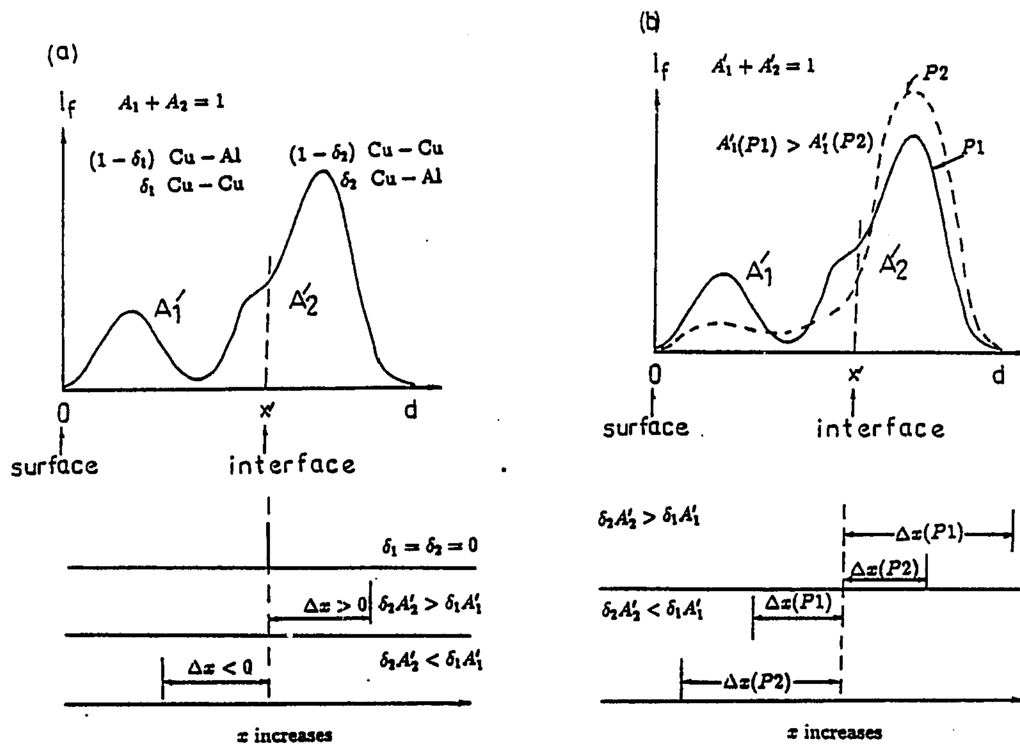

Figure 7.3: Change of the interface location due to the exsistence of the other type of bond. (a): Effects of the relative amount of the other type of bond, (b): effects of different incident angles.

small.

7.2.4 Consideration of Deviation in Density Profile

If the density is incorrect, then the calculated curve I_f vs depth (based on the density model) and the areas are incorrect. Since the main effect of a change of the incident angle from P1 to P2 is an increase of the second area A_2 (due to a larger penetration), it is natural to think of the deviation in the density in the region to the right of x as a source of error. As shown in Figure 7.4, assuming that the deviations in the areas ΔA_1 and ΔA_2 are the result of a deviation in the density:

$$\frac{\Delta I_f}{I_f} = \frac{\Delta \rho}{\rho}.$$

The deviation of r is then:

$$\frac{\Delta r}{r} = \frac{\Delta A_1}{A_1} - \frac{\Delta A_2}{A_2}$$

Equation 7.6 is not suitable for evaluating Δx in this case, because $\bar{I}_f$ is also a variable now ($\bar{I}_f = \bar{I}_x \rho$). A general relation between r, x and $I_f(\rho)$ is worked out as follows: Using $\Delta A_1 = \bar{I}'_{f2}\Delta x$ and $\Delta A_2 = \Delta I_{f2}(d-x) - \bar{I}_{f2}\Delta x$ (Fig.7.4), yields

$$\frac{\Delta r}{r} = \bar{I}'_{f2}(\frac{\Delta x}{A_1 A_2} - \frac{\Delta I_{f2}}{\bar{I}'_{f2}}\frac{d-x}{A_2}).$$

Rearrangement yields

$$\frac{\Delta x}{x} = A_1 \frac{d-x}{x}(\frac{\Delta r}{r} + \frac{\Delta \rho}{\rho}), \tag{7.9}$$

where $\Delta\rho/\rho \simeq \Delta I_{f2}/\bar{I}'_{f2}$ is used. To maintain r at the value of the EXAFS result, or $\Delta r = 0$, a change in x

$$\Delta x = A_1(d-x)\frac{\Delta \rho}{\rho}$$

is needed to compensate for a change in ρ. In a typical example: A 10% increase in ρ causes a 40-Å increase in x(P1), and a 25-Å increase in x(P2). A 10%

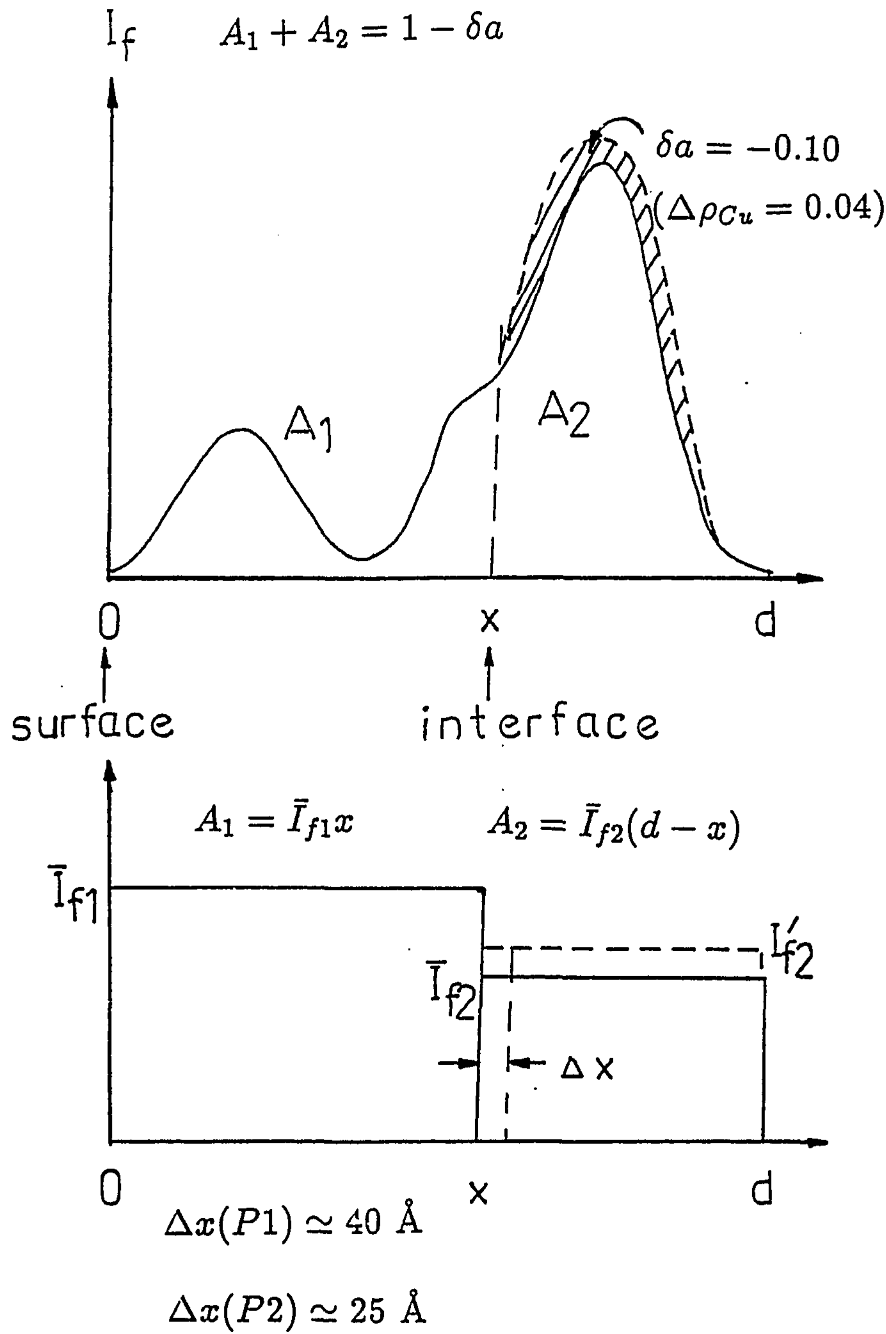

Figure 7.4: Change of the areas due to the deviation in the model of the density profile

error in the density is quite large. The error bar from fitting is typically 1%. Another source of error is caused by imperfections in the films. When modeling the reflectivity data, the sum of the relative densities of the two components are constrained to be unity. This constraint is not accurate if there is a large number of defects and vacancies (which is often true in polycrystalline films). The Al density artificially put in the Cu layer, for example, compensates for the existence of defects, but makes the Cu density smaller. A combination of 0.93Cu+0.07Al is equivalent to 0.95Cu+vacancies. This error is 2%. A total error of 3% seems to be maximum for $\Delta\rho/\rho$.

To simplify the correction procedure (without disturbing the density distribution), one can introduce a change in r to make a required change Δx, while keeping ρ constant. From Equation 7.9, one can see that the coefficient of $\Delta r/r$ is equal to that of $\Delta\rho/\rho$, therefore, $\Delta r = 0.03r$ is a good estimate.

To summarize all four sources of error: (1) GB contribution: causes x to shift 75 to 100 Å; (2) large-angle scattering: causes x to shift $\sim$ 20 Å if the scattered signal is 10% of the total Cu signal, $\Delta r = 0.1r$; (3) Presence of Cu-Cu bonds in the Al side and Cu-Al bonds in the Cu side: tends to cancel out; and (4) Deviation of the Cu density: causes x to shift 8 to 13 Å if the density has a 3% error, or $\Delta r = 0.03r$.

A comparison of all four types of errors with the error bar of x (determined by the error bar of the coordination numbers from EXAFS fitting) which is typically 10% (or 40 Å) shows that only type (1) makes a significant contribution to the determination of the interface location. Nevertheless, (2) and (4) should be included.

7.2.5 A Corrected Interface Location

Incorporating errors (2) and (4), the experimental EXAFS ratio should be modified:

$$r' = r + \Delta r_{(2)} + \Delta r_{(4)} = r + 0.10r + 0.03r = 1.13r.$$

By replacing r by r' in Equation 7.4, the new interface location x is derived. The new x values are listed in Table 7.2. In this attempt, x_1 is determined to be 400 Å for UHV(O) and 440 for UHV, and assumed unchanged thought out all annneals. The uncertainty of x_1 is similar to that of x. (The two error bars, Δx_1 and Δx, are correlated: An increase in x_1 causes an increase in x, to maintain a correct ratio pre-determined by the EXAFS fitting.) For the UHV sample, the new x values are more reasonable, compared to the nominal interface locations (Figure 7.5). The consistency among the three angles is observed. For the UHV(O) sample, the x values has larger discrepancies at higher temperature anneals among the three angles. In addition, when plotting the density profile together with the interface locations, x seems to be unreasonably large (Figure 7.6). This leads to another attempt: Instead of using the same x_1, try changing it on the two higher anneals (where the consistencies are poor with a fixed x_1). The new x_1's are 300 and 250 Å, respectively, for the 140 and 160°C anneals, which are substantially lower than the original (unnealed) value. The new results are better (Figure 7.7), and the consistencies are also improved. The results with varying x_1 are also listed in Table 7.2. Appendix A shows the procedure for determining x (under item SUM and AX) and examples of results.

In Figure 7.5 and Figure 7.7, there are two boundaries, x_1 and x, representing the Al/Cu-Al and Cu-Al/Cu interface, respectively. For the UHV sample (Figure 7.5), x_1 is stationary (within 40 Å), but for the UHV(O) sample (Figure 7.7) it moves towards the Al side as temperature increases. The Cu-Al/Cu interface location, x, has similar behavior for both samples — moving towards the Cu

Table 7.2: Location of the interface at various anneals obtained from the EXAFS ratio at angle V1, P1, and P2, considering the GB effect

(a) Fixed GB region (x_1)

UHV(O) x_1=400				UHV x_1=440				
T(°C)	V1	P1	P2	T(°C)	V1	P1	P2	P3
RT	425	420	-	RT	530	520	520	-
120	450	435	425	100	550	540	540	-
140	470	470	450	120	570	560	550	-
160	-	520	480	120^+	-	-	570	570
				140	-	-	580	570

(b) Varying x_1 for the UHV(O) sample

UHV(O)				
T(°C)	x_1	V1	P1	P2
RT	400	425	420	-
120	400	450	435	425
140	300	430	440	430
160	250	-	460	450

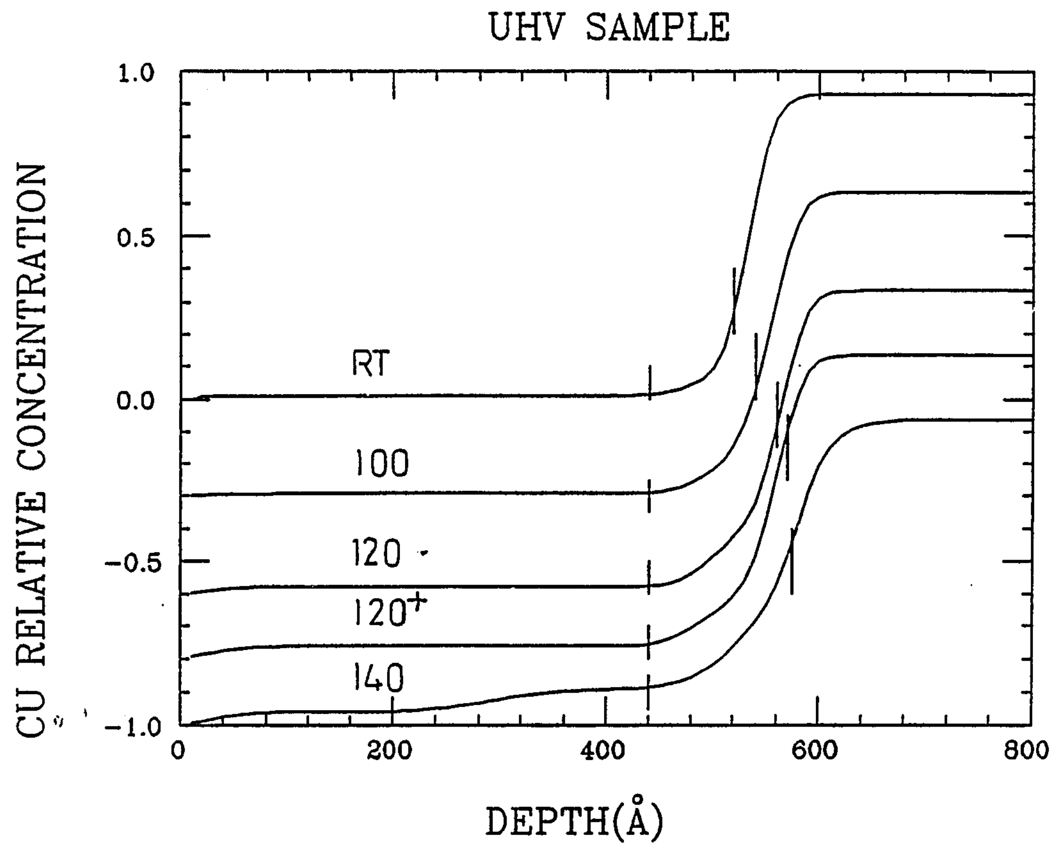

Figure 7.5: Movement of the interface as a function of anneals for the UHV sample, considering the GB effect.

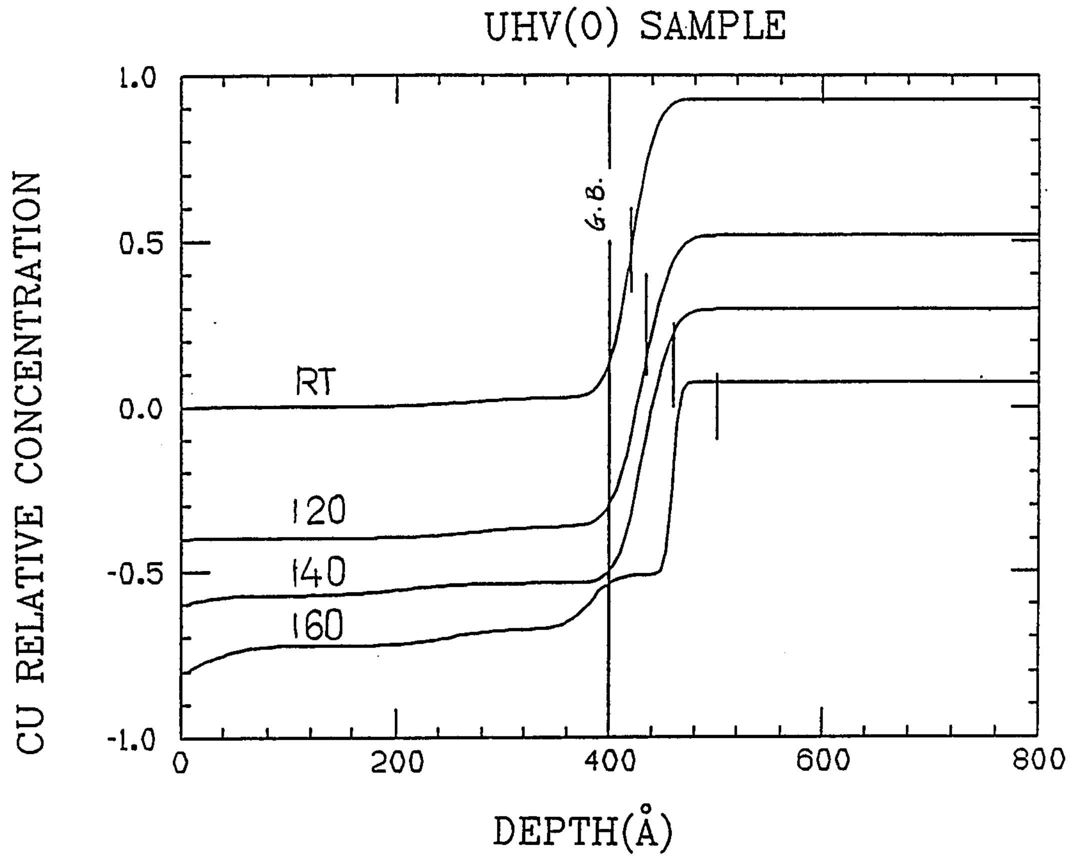

Figure 7.6: Movement of the interface as a function of anneals for the UHV(O) sample, considering the GB effect

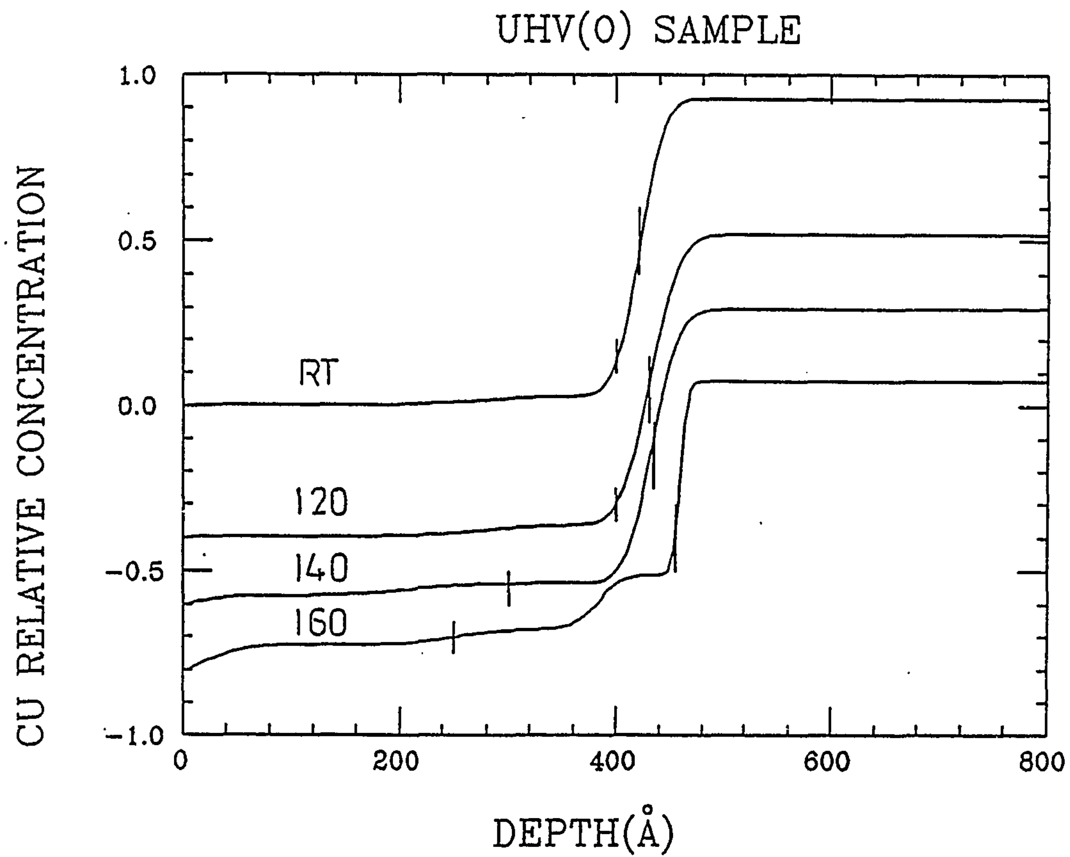

Figure 7.7: Movement of the interface as a function of anneals, considering GB effect and varying the Al/Cu-Al boundary as temperature increases

side for about 50 Å between RT and 160°C.

7.3 Growth Kinetics, Oxygen Effect, And A Picture Of Cu-Al Interfaces

7.3.1 The UHV Sample

The UHV results suggest a planar compound growth kinetics, which is in agreement with other studies ([3], [4]). Note that the temperature range used in this study is lower compared to the other ones (160 - 250°C for [3] and 160 - 220°C for [4]). For polycrystalline films, the grain boundary assisted diffusion is more important [5,62] at low temperatures. One would expect that the mixed Cu-Al region develops along the grain boundaries and the contacting interface (Figure 7.8a), mixed region represented by shaded areas). This resembles the type-B kinetics for GB diffusion (Figure 7.9, from [45]). Type-A is usually used to describe diffusions at higher temperatures (higher than 1/3 melting temperature), when the bulk diffusion is comparable to the grain boundary diffusion. Type-C is the other extreme, when the bulk diffusion is neglegible compared to the grain boundary diffusion. At the temperature range of this study, the intermediate type-B kinetics is more suitable [5].

Since the GB Cu is assumed not to contribute EXAFS signal (discussed previously), the Cu-Al bonds along the GBs might not be recognized. The main contribution is from the continuous layer near the interface. At the temperature range used, the mixed region near the interface is still Al-rich (see density profile). The concentration of Cu in $CuAl_2$ compound is ~30% at., and in other compounds it is even higher. It seems that the Cu diffusing into the mixed region tends to react with the remaining Al, before the Cu which goes into the GBs starts to react with the Al in the Al layer. This is probably why the Al/Cu-Al boundary does not change by more than 40 Å. The increasing Cu concentration

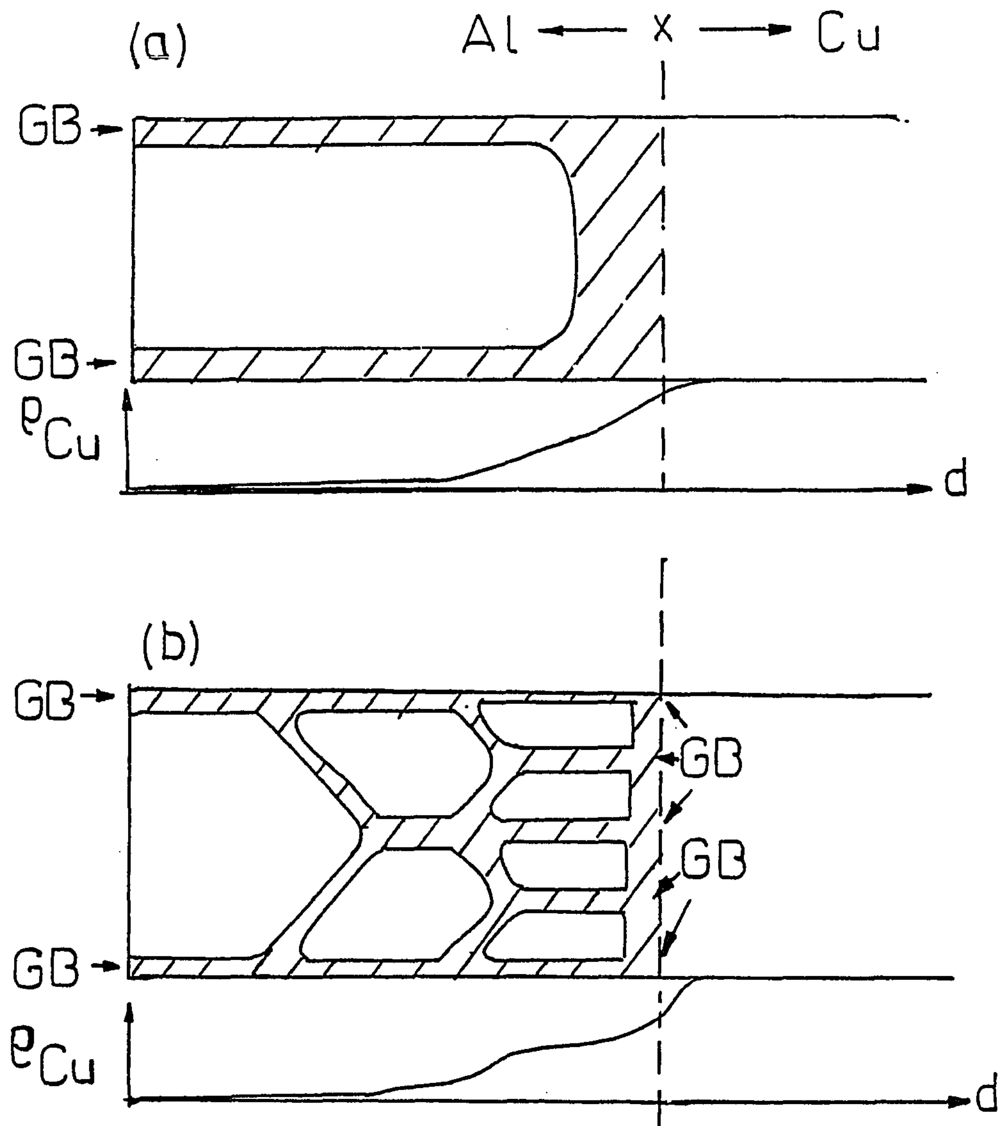

Figure 7.8: A sketch describing the kinetics of interface reation for the (a) UHV and (b) UHV(O) sample. In (b), smaller grains near the interface join to make larger grains towards the surface.

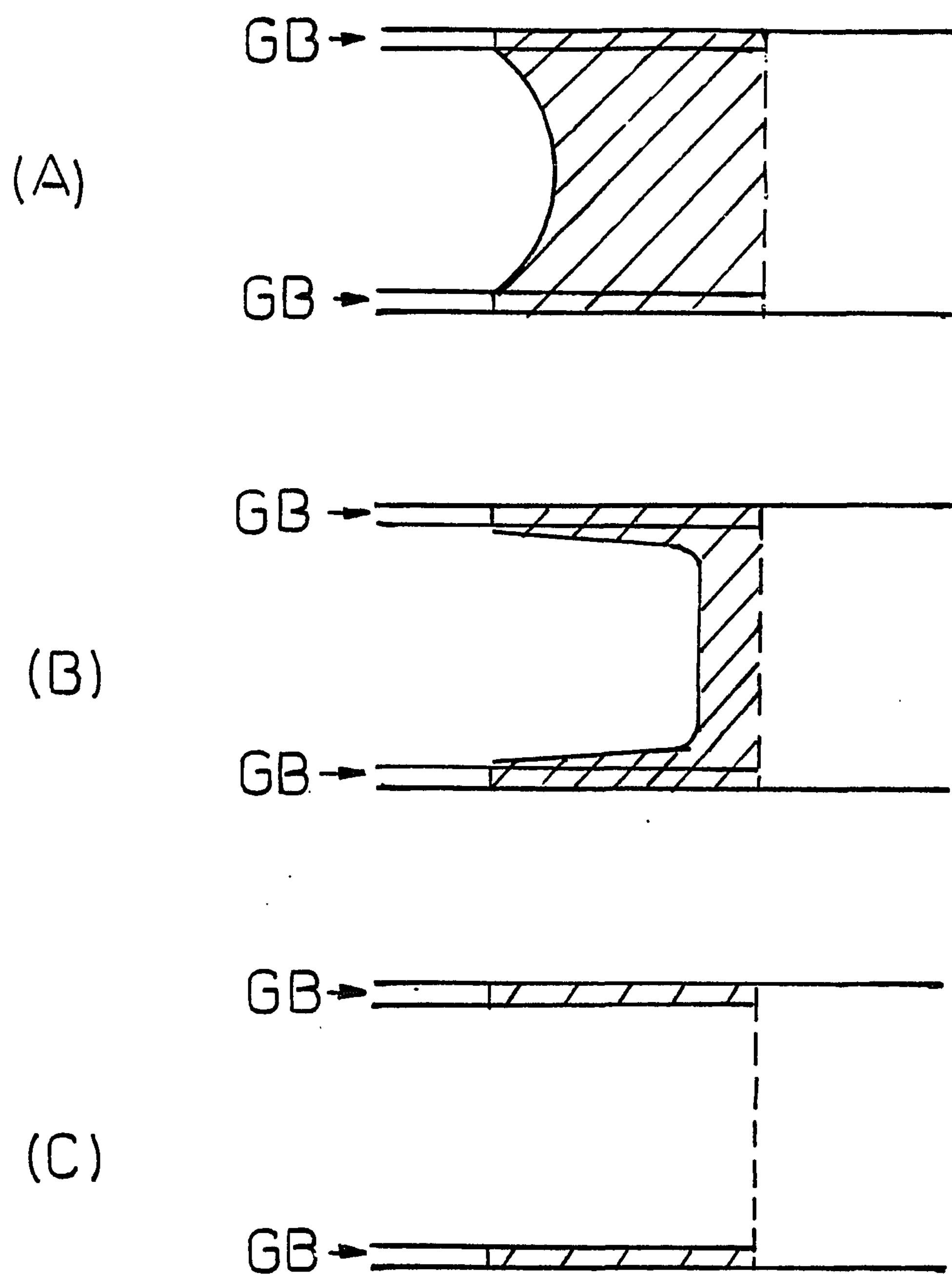

Figure 7.9: A-, B-, and C-type of GB diffusion model, based on reference [45].

in the Al layer is a sign of a continuing supply of Cu into the Al GBs. Eventually more ordered Cu-Al bonds will form and the Al/Cu-Al interface will move towards the Al side, upon higher temperature anneals.

7.3.2 The UHV(O) Sample. Difference in Grain Sizes?

The UHV(O) sample has the same kinetics. The different behavior can be attributed to the finer grain size near the interface. This is described as follows: The fact that x_1 is closer to x compared to the UHV sample suggests that the region of Cu-Al mixing is more confined in the UHV(O) sample. The higher concentration of Cu in the density profile near the interface obtained from the reflectivity fitting (better seen in the log plot in Fig.4.4, which shows that the extra "bump" in the Al layer) falls outside of the reacted region. This means that the extra "layer" is not due to the Cu-Al reaction, as one might naively think at the first glance, but it is due to GB diffusion of Cu into the Al layer. The reason the concentration is higher, can be speculated as the finer grain size for the UHV(O) sample (Figure 7.8(b)).

There is no direct proof of this speculation, since the TEM experiments were unsuccessful. However, the XPS results do lend some support. As described in Section 6.4, the experiment on the Al/O/Cu system suggests that there is clustering at the interface, in contrast to the Al/Cu system which behaves more like a layer-by-layer growth. One study using Auger showed that evaporating Cu onto an Al oxide substrate caused clustering of the Cu, whereas evaporating onto an Al substrate resulted in intermixing [64]. Clustering could mean a rougher interface and finer grain size for the subsequent film. Another study on effects of oxygen on the growth of Al films showed that the film morphology was strongly influenced by the oxygen partial pressure [65]. They found a fine-grained layer at partial pressure higher than 1×10^{-4} Pa ($\sim 8 \times 10^{-6}$ torr) and island growth

below this pressure. Many grains are oxidized. The oxygen partial pressure for the UHV(O) sample was 7×10^{-7} torr ($\sim 0.9 \times 10^{-5}$ Pa) before the Al deposition, similar to the work cited. The clustering mechanism is supported.

Eventually, the grains coalesce to form larger grains when the film is thick enough. XPS data indicate that the fine-grain region is at least 26 monolayers ($\sim$ 65 Å). The density profile in Figure 4.4 also suggests about the same thickness. Despite more Cu-Al contact in this region, there is no indication of chemical bonding (which should give a unique distance and should be detected by EXAFS). Oxygen must have played an important role in this behavior. The initial interface is formed of some kind of Cu-Al-O mixed compound. (This can not be observed directly by EXAFS, because the oxygen is only 1000 L worth which results in probably no more than a few monolayers[66], and the backscattering amplitude of the oxygen atoms decays very rapidly at high k.) This compound prevents a reaction between Cu and Al (to form $CuAl_2$). In view of the annealing behavior, it is reasonable to say that the interface oxide layer also raised the threshold for the Cu-Al reaction. Once the reaction starts, there is a tendency for the UHV(O) and UHV samples to react the same way.

The expansion of the Cu-Al region towards the Al side (x_1 moving towards the Al side) for the UHV(O) sample, suggests that the Cu-Al bonds formed in the Al layer via GB supply become detectable by EXAFS at higher anneals. It might imply that the Al in the mixed (oxidized) region near the interface is less reactive compared to the Al towards the surface. When the annealing temperature is high enough, the Cu atoms can break through the oxide barrier and react with the Al through the GBs. This is in contrast to the UHV sample in which the Al in the mixed region is ready to "capture" any out-diffusing Cu atoms.

7.3.3 More Comparison on Annealings

Initially the Cu-Al region is more confined for the UHV(O) sample, at higher temperature it is comparable to that of the UHV sample due to the spreading towards the Al side. Therefore, the amount of compound formation is comparable for the two samples after high temperature anneals. This shows that once the oxide barrier is broken down, the reaction between Cu and Al is quite similar for the two samples. If the temperature range used for the study was too high, the oxygen effect would not be observed (see [5], in which the diffusion couple was annealed at 175°C for 85 minutes). This might not be true if the deposition sequence is reversed ([64] in which Al_2O_3 used as substrate, also see [59]).

With regard to the Al diffusion into the Cu layer, this technique can not distinquish the difference between the two samples. It seems that by adding oxygen the film morphology is affected more on the Al side than the Cu side. Since the oxygen was added after the Cu was deposited, it is reasonable that the subsequently deposited Al film is more severely modified than the Cu film.

7.3.4 Bond Lengths, Phases

In the known Cu-Al compounds, the average Cu-Cu and Cu-Al bond lengths (obtained and calculated from [67]-[70]) are listed in Table 7.3. One can imagine that if all phases exist at the same time, the picture is quite complicated. Other studies on Cu-Al thin films reported simultaneous growth of $CuAl_2$ and a very small amount of Cu_9Al_4, and subsequent growth of CuAl [4]. The present technique concludes that the Cu-Al interface compound has an average Cu-Al bond length of $\sim$ 2.56 Å, and after annealing at 140°C the bond length is $\sim$ 2.52 Å on the Cu side (this seems to agree with other studies which showed that the next phase is formed on the Cu side for Cu rich systems). All this happens within 200 Å near the original Cu-Al interface, which is not easily detected by other

Table 7.3: Bond lengths of stadard compounds between Cu and Al

	$CuAl_2$		CuAl		Cu_9Al_4	
Bond	N	R	N	R	N	R
Cu-Cu	2	2.44	4	2.56	*	2.62
Cu-Al(1)	8	2.60	2	2.47	*	2.61
Cu-Al(2)			4	2.59		

* Due to the complicated structure of Cu_9Al_4, an averaged distance is used:

$$R = \bar{R} = \frac{\Sigma_i N_i R_i}{\Sigma_i N_i}.$$

techniques. However, the Cu-Al bond lengths do not seem to match any of the standard compounds, but the Cu-Cu bond lengths could be matched with either $CuAl_2$ or CuAl (has a 2.44 and 2.56 Å bond, respectively, both bonds were detected at various stages). It might mean a complicated simultaneous growth of many competing phases. Certain phases might not be kinetically stable and therefore are suppressed [46]. Under certain conditions (e.g. heating and cooling rate) the growth of one phase might not be dominating very strongly. In this study the annealings were done for 5 minute for each temperature, in contrast to other studies in which the samples were annealed isothermally for longer periods of time. The observation might also suggest that the interface being studied is in a process of evolving into a standard compound, yet the atomic arrangement does not quite reach the required equilibrium to form a compound.

When determining the interface location, the major assumption in the model is that the Cu in the Al grain boundaries does not contribute to the EXAFS. This assumption made the determination of the interface location somewhat arbitrary. The only constraint lies in the consistency of the data from all three angles, which is not always satisfactory. Currently, there is no other way of measuring grain boundary structure in polycrystalline films. If the GB contribution can be isolated, the interface can be determined with more confidence. Electron yield detection could be a solution because of its high surface sensitivity and freedom from the substrate contamination [72]. This should be an interesting direction for future work.

Chapter 8

SUMMARY

This thesis has presented a new technique for studying thin film interfaces. By sending X rays onto thin films at a glancing angle, the penetration of the X rays can be controlled. Below the critical angle of the sample material (a few milliradians), the X rays penetrate into a shallow region ($\sim$ 30 Å) in the form of an evanescent wave. This feature assures surface sensitivity. In the case of a bilayer, interfaces can be probed, provided the heavier element is deposited first.

A simple experimental procedure was used to perform two types of measurement: Scanning the energy and the angle of the incident beam. X rays from a synchrotron radiation source are energy-selected by a double crystal monochromator and the beam size is narrowed, both vertically and horizontally, by a slit. The beam is monitored by ionization chambers before (incident beam) and after (reflected beam) interacting with the sample. An additional chamber collects fluorescence signals. Therefore, the reflectivity and fluroescence are measured simultaneously. The time for data collection is $\sim$ 10 minutes for an angle scan and $\sim$ 20 minutes for an energy scan.

The analysis of the reflectivity data involves model simulation and least-square fitting procedures. These procedures provide macroscopic information about thin films: The thickness and roughness of each layer, and the composition distribution. The accuracy of each fitting parameter was discussed in Chapter 4.

The roughness parameter has relatively large uncertainty (up to 50%) due to the correlation of the roughnesses of the adjacent layers. Considering the fact that there is no other direct measurement of interface roughness except for TEM, the reflectivity technique is very helpful in thin film characterizations yet relatively easy to apply.

The fluorescence signal is used to extract EXAFS, which contains structural information. An ADC procedure was developed to remove distortions in amplitude and phase in the fluorescence EXAFS obtained from concentrated samples. After ADC, the EXAFS data can be analyzed using one of the many well-developed software packages for transmission EXAFS.

The goal of using the glancing angle technique is to identify atomic structures at a certain depth in the thin film. This goal can be achieved by combining the reflectivity and the EXAFS results. The model obtained from fitting to the reflectivity data can be used to determine what part of the sample is illuminated by the X rays at a certain angle. The EXAFS data taken at this angle reveal the structure of the illuminated part. By comparing the EXAFS data taken at several angles (which correspond to contributions from various parts of the sample), the interface location (which separates one type of structure from the other), can be determined by preserving the consistency of interface locations obtained from data measured at all angles.

The glancing angle X-ray reflectivity and EXAFS technique was applied to Cu-Al thin films to study the interfacial reaction between the two elements. The thin films were deposited under various conditions (HV,UHV,UHV(O)) and were annealed before each measurement. Qualitative difference was found among the three samples. Under similar conditions, the degree of reaction seemed to be the highest for the UHV sample and lowest for the HV sample. The data shows that the deposition condition affects the interdiffusion (which is the predominant

mechanism for thin film reactions).

Least-square fitting of the reflectivity from all three samples show that Cu diffuses into the Al layer (probably through the grain boundaries) as the temperature goes up. For the UHV and UHV(O) samples, a distinct mixed layer with large roughness grows at the interface when the temperature is high enough. This extra layer is initially about 30 Å at room temperature, and grows to $\sim$ 200 Å after annealing at 160°C. Whether the Cu and Al are reacted within the mixed region can not be determined by reflectivity. The EXAFS data can clarify this question.

After the ADC procedure, the EXAFS data from UHV and UHV(O) at all angles and all annealing temperatures were analyzed and compared. The results agree with the qualitative observation: The UHV sample is more reacted than the UHV(O) sample, possible because there is an oxide barrier at the interface. However, there was no evidence of a pure $CuAl_2$ phase. The Cu-Al bond, which is 2.60 Å in the $CuAl_2$ structure, is always shorter (2.52 to 2.57 Å). Attempts using X-ray diffraction to look for the $CuAl_2$ were unsuccessful. The thin film interface reaction may be too disordered to be described by a single phase. In fact, other studies show ([3],[4]) multiple phases growing simultaneously, with $CuAl_2$ being the dominant one at temperatures below 200°C. Examining the structure of other compounds (e.g. CuAl, Cu_9Al_4) shows that the existence of other phases would reduce the Cu-Al bond length.

Using the EXAFS results, the ratio of N_{Cu-Cu} to N_{Cu-Al} (the number of Cu-Cu bonds to the number of Cu-Al bonds) was determined for each angle at each anneal. This ratio corresponds to the contribution from the illuminated part of the sample at each angle. To determine the boundary separating Cu-Cu and Cu-Al bonds, the area under the calculated flourescence curve (based on the model from fitting to the reflectivity) was integrated and divided. The interface

locations were adjusted to find the same value as the EXAFS ratio. This location is also constrained by the demanding consistency of all the measurements. The analysis shows that consistency is obtained at all angles, to an accuracy of 40 Å. The results also suggest that the Cu in Al grain boundaries does not contribute to the EXAFS. This is not too surprising since the grain boundary structure can be very distorted. In the interface region, the Cu-Al bond lengths do not match any of those in standard Cu-Al compounds. This could suggest a simultaneous growth of multiple phases, or a disordered area at the interface.

Other techniques were used to provide complemetary information. RBS, AES, and TEM supported the X-ray results, but were less precise and do not reveal structural differences. Photoemission studies provided information on a different scale, which seemed to confirm the role of oxygen exposure (indicating that there is clustering during film growth, which generates finer grains).

The glancing angle X-ray reflectivity and EXAFS technique are superior to other techniques at a qualitative level, considering the simplicity of performing the experiment and the ability to direct interpret the data. Quantitatively, the reflectivity part gives satisfactory results from model fitting. The EXAFS part is also satisfactory for small reactions. For more extensive reactions, the data analysis is limited by the complexity of interface formation: A multiple-phase structure requires more atom shells in the EXAFS fitting, which reduces the accuracy of the fitting. Therefore, the strength of the glancing angle EXAFS technique is in studying the initial reaction at thin film interfaces, when the interaction region is too small to be easily probed by other techniques. At present, it can be applied to any thin solid film couples provided that the absorption edge of one material does not fall into the EXAFS region of the other material. There is a problem for films in a single crystal form, because the Bragg diffraction can severely affect the EXAFS data ([73]). New detectors are under develop-

ment which should solve this problem in the future, allowing the technique to be more widely used. In the current study there was no experimental way of directly measuring the grain boundary structures, and an assumption had to be made that they are disordered. If this assumption can be confirmed by future experiments, the confidence in the technique will be further improved.

Thin film technology heavily depends on understanding interface reactions, to which the glancing angle EXAFS technique can contribute. This thesis has demonstrated that the technique can be a useful tool for probing initial reactions at Cu-Al thin films interfaces. With the aid of synchrotron radiation sources, the application of the glancing angle EXAFS technique has a promising future for studying interfaces of various systems.

Appendix A

PROGRAMMING NOTES

A.1 SUM and AX: Estimation Of The Interface Locations

After calculating the fluorescence intensity as a function of depth, SUM is used to calculate the integral of the curve:

$$SUM(x) = \int_0^x I_f dx,$$

where x extends to the total thickness of the layers. The output is written as X-Y pairs $(x, SUM(x))$. Feed this data file into AX, which calculates the appropriate interface location x that seperates the Cu-Al and Cu-Cu regions. The input information also includes the estimation of the GB area, x_1, and the ratio of Cu-Al to Cu-Cu bonds (from EXAFS fitting), r. The results from UHV(O) and UHV samples, unannealed and 140°C annealed, are complied in the following tables:

UHV(O) RT: $\overline{x - x_1} = 35 \pm 25$ Å.

	V1 r=0.64		P1 r=0.43	
x_1	x	$x - x_1$	x	$x - x_1$
350	410	60	405	55
380	420	40	415	35
400	425	25	420	20
440	455	15	450	10
460	475	15	470	10

UHV(O) 140°C: $\overline{x - x_1} = 75 \pm 25$ Å.

	P1 r=5.4		P2 r=1.3	
x_1	x	$x - x_1$	x	$x - x_1$
350	460	110	440	90
380	465	85	450	70
400	475	75	455	55

UHV RT: $\overline{x - x_1} = 110 \pm 30$ Å.

	V1 r=1.4		P1 r=0.86		P2 r=0.54	
x_1	x	$x - x_1$	x	$x - x_1$	x	$x - x_1$
380	520	140	510	130	520	140
400	520	120	510	110	520	120
440	530	90	520	80	520	80

UHV 140°C: $\overline{x - x_1} = 175 \pm 40$ Å.

	P2 r=10.5		P3 r=2.0	
x_1	x	$x - x_1$	x	$x - x_1$
350	560	210	560	210
380	570	190	560	180
400	570	170	560	160
440	580	140	570	130

The consistency between angles can be compared by varying x_1 value.

A.2 FITING2: A Fitting Routine For Reflectivity Data

The IMSL ZXSSQ is used for finding the minimum of a function (the difference between the calculation and the experimental data). The input function is based on REFLU, using a matrix calculation [36]. Usage: see Appendix C.2.

A.3 FLCORR: Corrections To Ion Chamber Response

The first version was written by Steve Heald for making the I_0 chamber absorption correction, which is needed for the fluorescence EXAFS data analysis. It is modified to correct the I_r chamber response. Both corrections for I_0 and I_r are needed for the reflectivity EXAFS data analysis.

The true reflectivity R is related to the ratio I_r/I_0 (the ion chamber output) by the following equation:

$$R = \frac{I_r}{I_0} \frac{e^{\mu_0 x_0}(1 - e^{-\mu_0 x_0})}{1 - e^{-\mu_r x_r}},$$

where μ_0, x_0 are the absorption coefficient and the length of the gas in the I_0 chamber, respectively, and μ_r, x_r are the counterparts for the I_r chamber.

Usage:

```
$FLCORR infile,outfile
EDGE ENERGY (EV)> 8980 // Cu k-edge
THE INDICES OF THE GASES ARE:
1=HE, 2=N2, 3=NE, 4=AR, 5=KR, 6=XE
1--FLUOR. ONLY, 0--REFL. ONLY, 2--BOTH> 1
INPUT IO GAS FRACTIONS>,1/ //pure N2
CHAMBER LEGTH (CM)>15
NKEY1,NKEY2>1,10 // nkey 1 through 10 to be corrected
NKEY1,NKEY2>// end
```

A.4 FLUCOR: Manipulating UW binary data files in XMU format

The program can handle division, multiplication, inversion, or square root between two data files in XMU format. The program asks information of the first file, the second file and what to be done with them. Then a comment line and a new XMU file name are input and used to create a new file containing the generated file in XMU format.

Usage:

```
$RUN FLUCOR
(answer the questions)
```

A.5 COR: ADC procedures

1 Run REFLU to calculate X_0, $\frac{dX}{d\beta}$, $\frac{dX}{d\delta}$, and $\frac{d\delta}{d\beta}$. X represents F for the fluorescence, R for the reflectivity. In REFLU, after entering the regular information CMP, LIN, NRG (see online HELP), type COR to generate the necessary output files for the next step. The calculated F_0 as a function of energy has to be converted into XMU format by using CALLFLU routine.

2 Construct a new function from the raw data file. In case of the fluorescence data, divide the data by the calculated function F_0; In case of the reflectivity data, divide the data by calculated R_0/μ_0. This is done by utilizing FLUCOR, inputting the data and the calculations in XMU formats.

3 Do a normal EXAFS analysis procedure on the constructed function (now also in XMU format), including generating the ENV file.

4 Use the output from REFLU to calculate the correction factor and store it in an ENV format. This procedure is summarized in a command procedure COR. It requires two input files: PHASE.INF and DOC.INF. They contain the phase information of the input files, and the documentation for the generated files, respectively. The output file is written in an ENV format, the file name is part of the input in DOC.INF.

Example of DOC.INF:

```
TOT.ENR
CHI
8.979
CU U3 A7 P3 5.38MRAD // comments
TOT
TOT.CHI
FST.ENR
CHI
8.979
CU U3 A7 P3 5.38MRAD // comments
FST
FST.CHI
SND.ENR
CHI
8.979
CU U3 A7 P3 5.38MRAD // comments
SND
SND.CHI
END
eof
```

```
SND.CHI
1
0
.978
0
N
UNT
Y.CHI
SND.CHI
1
0
-.207
0
N
UNT
FST.CHI
END
eof
Y.CHI
1
0
1
0
N
X.CHI
1
0
```

```
2
1
N
TAN.CHI
END
eof
TAN.CHI
1
PHI
PHI.CHI
END
eof
PHI.CHI
1
TOT.CHI
1
TOT CU U3 A7 P3 5.38 // comments
TOTF.ENV // output filename containing the correction factor.
eof
FLU.DAT
FLU1.DAT
1
1
eof
FLU1.DAT
XMU
FLU CU U3 A7 P3 5.38 // comments
```

```
FLU
FLU.XMU
END
eof
```

In the example above, the only lines to be changed are the comment lines and the output file name. Leave the others alone.

Example of PHASE.INF:

```
PERCENT, PHASE DIFF,INDEX(1-F,2-1/R,3-LN(R),4-MUO*R/RO),SHIFT
5,78,1,0 // index:  1 for fluorescence, 4 for reflectivity.
```

5 Run TOTENV: divide the amplitude of the data ENV by the correction ENV, and subtract the two phases. Generate a new ENV file containing the corrected first shell data in ENV format.

Usage:

```
$RUN TOTENV
(answer the questions)
```

A.6 CALLFLU

Converts X-Y pairs into an IDP file. Can output XMU and CHI format.

Usage:

```
$RUN CALLFLU
(answer the questions)
```

A.7 IDPLIS

Converts IDP format into X-Y pairs. Only XMU format is handled. Use UN-PACK for other formats.

Usage:

Creat a file IDPLIS.INF containing the following: `CUU3AA.XMU // IDP filename`

```
c*input nkey,v0,xscal,wgt,exca(0:interpolate,1:copy) // comments
U3A4.DAT // Filename containing the X-Y paris
7,0,1E-3,1,1/ // nkey in the IDP file, x shift, x scale, y weight, 1
for listing
U3A5.DAT // Next file...
1,0,1E-3,1,1/
/ // End of action
```

Then

```
$RUN IDPLIS
```

Appendix B

SOME CALCULATIONS

B.1 Notes From James: Model For X-ray Absorptions

When X rays interact with a medium, the situation can be described as a collection of oscillators scattering the incident electromagnetic wave, with a scattering factor f. The behavior of the scattered beam is dependent on the energy of the incident beam E (frequency ω) relative to the absorption edges E_k (frequency ω_k) of the material. When the incident beam energy is much higher than all the absorption edges, the scatterers can be viewed as a group of free electrons, which is described by a scattering factor

$$f = f_0' + if_0''$$

where

$$f_0' = Z$$

and in our work, $\sigma(\omega) = (\omega_0/\omega)^3\sigma(\omega_0)$ is assumed, which gives

$$f_0'' = \frac{\omega_0}{4\pi r_e c}(\frac{\omega_0}{\omega})^2\sigma(\omega_0),$$

where $r_e = e^2/m_e c^2$ is the classical electron radius, $\sigma(\omega_0)$ is the absorption cross section at a reference frequency ω_0.

When ω is in the neighborhood of ω_k, an additional term must be added to f to account for the anomalous dispersion:

$$f = f_0' + i f_0'' + \Delta f_k,$$

where Δf_k is complex:

$$\Delta f_k = \frac{x^2 \ln(1 - x^2 + i\kappa x) + x^2 - i\kappa x}{(x^2 - i\kappa x)^2} g_k \tag{B.1}$$

where $x = \omega/\omega_k$, and $\kappa = \gamma/E_k$ (γ is the "core hole width"), and g_k is the oscillator strength:

$$g_k = \frac{1}{4\pi^2 r_e} \omega_k \sigma_k(\omega_k) \tag{B.2}$$

where $\sigma_k(\omega_k)$ is the absorption "jump" at the edge ω_k. The values of the absorption cross section can be found in McMaster's Compilation of X-ray Cross Sections.

The index of refraction, r, is written as

$$r = 1 - \delta - i\beta,$$

which is related to the scattering factor f by

$$r = 1 - 2\pi N r_e (\frac{c}{\omega})^2 f$$

where N is the atomic number density, calculated by $N = N_0 \rho / A$, where N_0 is Avogadro's number, ρ the mass density, A the atomic mass. The real part of f contributes to δ, the imaginary part to β:

$$\delta = 2\pi N r_e (\frac{c}{\omega})^2 [f_0' + \mathrm{Re}(\Delta f_k)],$$

$$\beta = 2\pi N r_e (\frac{c}{\omega})^2 [f_0'' + \mathrm{Im}(\Delta f_k)]. \tag{B.3}$$

If the material has more than one type of element, f should be summed over all elements.

The coefficient, $2\pi N r_e (c/\omega)^2$, at X-ray energies of the order of 10 keV (near the Cu K-edge) is of the order of 10^{-6} for Cu. f_0' is of the order of Z (the charge number), f_0'' and Δf_k are usually near unity. Therefore, δ and β are small positive numbers: $\delta \sim 10^{-5}, \beta \sim 10^{-6}$.

When evaluating $d\delta/d\beta$ (for correcting anomalous dispersion in EXAFS), the following calculation replaces the Kramers-Kronig analysis: Putting Equation B.2 into B.1, and emphasizing on the linear relation between Δf_k and σ_k, Equation B.1 can be written as:

$$\Delta f_k = (\Delta f_k)' \sigma_k \tag{B.4}$$

where $(\Delta f_k)'$ is independent of σ_k. Hence

$$\begin{aligned} \mathrm{Re}(\Delta f_k) &= \mathrm{Re}(\Delta f_k)' \sigma_k, \\ \mathrm{Im}(\Delta f_k) &= \mathrm{Im}(\Delta f_k)' \sigma_k. \end{aligned} \tag{B.5}$$

Since δ and β are calculated by using the absorption cross section at the relevant edge σ_k, in the case of EXAFS where the fluctuation is caused by a change in σ_k, Equation B.3 and B.5 lead to the derivatives:

$$\frac{d\delta}{d\sigma_k} = 2\pi N r_e (\frac{c}{\omega})^2 \mathrm{Re}(\Delta \mathrm{f_k})'$$

$$\frac{d\beta}{d\sigma_k} = 2\pi N r_e (\frac{c}{\omega})^2 \mathrm{Im}(\Delta \mathrm{f_k})'.$$

Combining the two equations above, a convenient expression is obtained for the magnitude:

$$\left| \frac{d\delta}{d\beta} \right| = \frac{\mathrm{Re}(\Delta f_k)'}{\mathrm{Im}(\Delta f_k)'} \tag{B.6}$$

A phase factor must be added to account for the fact that the oscillations in δ and β are out of phase. From experimental results and Kramers-Kronig analysis [26], the phase difference is always $\sim \pi/2$. Thus,

$$\frac{d\delta}{d\beta} = \frac{\mathrm{Re}(\Delta f_k)'}{\mathrm{Im}(\Delta f_k)'} e^{i\frac{\pi}{2}}. \tag{B.7}$$

B.2 Calculations Of X-ray Reflectivity For Multilayers

Consider a three media system: air/Al/Cu (referred to as 1/2/3) where the air and Cu layers are infinitely thick. The recursive equation in Chapter 2

$$R_{n-1,n} = a_{n-1}^4 \frac{R_{n,n+1} + F_{n-1,n}}{R_{n,n+1}F_{n-1,n} + 1}$$

can be specified as

$$R_{12} = \frac{\gamma_2 + \gamma_1 e^{-2if_2d_2}}{\gamma_1\gamma_2 + e^{-2if_2d_2}}$$

where $\gamma_n = b_n/b_n^R$. The amplitude of R is

$$\mid R_{12} \mid = [\frac{\gamma_1 + \gamma_2 + 2\gamma_1\gamma_2 cos(2f_2d_2)}{1 + \gamma_1\gamma_2 + 2\gamma_1\gamma_2 cos(2f_2d_2)}]^{1/2}$$

The $\cos(2f_2d_2)$ factor gives rise to the oscillations in R as a function of angle: f_2 is the vertical component of the wave vector in layer 2, which is a function of angle. The same type of oscillation occurs as the energy changes (which leads to a change in the magnitude of the wave vector). The oscillation frequency is proportional to the layer thickness d_2. If there are more layers, oscillations occur whenever there is interference between the incidence and the reflectence, and the frequencies are determined by the distance between the surface and the reflecting interface.

B.3 Calculations Of X-ray Fluorescence For A Thin Film

As shown in Figure 2.3, the intensity of the X rays at depth x is

$$I_x = I_s e^{-\mu^* x/sin\theta},$$

where I_s is the surface intensity, and μ^* is the effective absorption coefficient. The fluorescence excited from a thickness dx at x is:

$$dI_f' = I_x \mu_A dx/sin\theta.$$

Part of this fluorescence is absorbed on the way out to the surface, leaving

$$dI_f = dI'_f e^{-\mu_f x/sin\phi}$$

to be detected. The total fluorescence being detected on the surface, assuming $\phi = 90°$, is

$$\begin{aligned} I_f &= \int_0^d dI_f \\ &= I_s \mu_A \int_0^d e^{-\mu^* x/sin\theta - \mu_f x} dx/sin\theta \\ &= I_s \frac{\mu_A/sin\theta}{\mu^*/sin\theta + \mu_f}(1 - e^{-(\mu^*/sin\theta + \mu_f)d}). \end{aligned}$$

Denote $\mu_a = \mu_A/sin\theta$, $\mu_t = \mu^*/sin\theta + \mu_f$, it yields:

$$I_f = I_s \frac{\mu_a}{\mu_t}(1 - e^{-\mu_t d}).$$

I_s can be calculated as:

$$I_s = I_0(1 + R_{12} + R_{12}^* + \mid R_{12} \mid^2),$$

where I_0 is the incident beam intensity. When $\theta \gg \theta_c$, μ^* can be replaced by μ, the actual absorption coefficient, and $I_s = I_0$.

Appendix C

DATA ANALYSIS PROCEDURES

C.1 Procedures For EXAFS Data Analysis

The following is a simple description of usage of the UW software for fluorescence EXAFS data analysis. See online HELP and [51] for more details.

1. Convert raw data into IDP format: run CONVERT, which generates an XMU file.
2. Run FLCORR to make a correction of the ionization chamber absorption.
3. Run BACK for background subtraction, which generates a CHI file.
4. Run FT and IFT for Fourier tranform and back transform to obtain the first shell data, and generate an ENV file.
5. Do ADC, follow procedures listed in Appendix A, which generates a new ENV file.
6. Fitting: use program EXCURVE, to fit the corrected first shell data.

C.2 Procedures For Reflectivity Data Analysis

When raw data is converted into XMU format, first use REFLU to calculate the reflectivity using the known information (such as layer thickness, types of layers, degree of mixing), and adjust the parameters to obtain a reasonable fit. Once the parameters are set, the following procedures are used:

1. Edit the following files to input information:

   DAT.FNM (filename)

   `PUT IN DATA FILE NAME//` comments

   `[CHEN.OCT87.CUAL.U3]` // directory name

   `CUU3AA.XMU` // file name

   DAT.FIL (file)

   `,1 [CHEN.OCT87.CUAL]CUU3AA.XMU` // comments

   `1.4E-4,5,9.2,1.0,6,8.6,1.31,0` //θ_0, nkey1, E_1, NOR_1, nkey2, E_2, NOR_2, index (0= fitting, 1 = no fitting)

   `EOF` // end of file

   DAT.INT (initial)

   `C ENTER ANGPST,MSTAR,MEND,CENT BELOW` // comments

   `1E-6,30,190,.65` // motor step, points to be disregard at the start, at the end, smoothing factor

   DAT.CIN (component information)

   `29,63.54,8.92,8.979,3809,30300,.0015` // element 1. Z, A, ρ, E_k, σ_b, σ_a, γ

   `13,27,2.7,8,2246` // element 2, Z, A, ρ, E_b, σ_b

```
13,27,2.7,10,1131 // element 2, Z, A, ρ, Ea, σa
8,16,1.429E-3,8,285.1 // element 3 ...
8,16,1.429E-3,10,140
24,52,7.19,10,11930 // element 4 ...
24,52,7.19,10,11930
14,28.09,2.33,10,1570 // element 5 ...
14,28.09,2.33,10,1570
```

DAT.LIN (layer information)

```
LYR OX // comments
0 // regular roughness
30,40,2,2,3,.7763,1306.2 // D, σ, nc, ic1, ic2,... icnc, ρ1, ρ2,... ρnc
LYR4 // next layer...
0
468,26,2,1,2,.023,.977
LYR5
0
65,25,2,1,2,.192,.808
LYR6
0
500,20,2,1,2,.934,.066
EOF // end of input layers
```

DAT.FIT2 (fitting)

```
! NSIG,EPS,DELTA,MAXFN,IOPT // comments
2,0,0,100,2 // ,,,maximum number of function calls,
```

DAT.TRK (track of parameters)

`1,2,4,5,6,7//` the parameters to be varied (called by the index), up to six. See procedure 2 for how to find out the index of each parameter.

2. To obtain a list of the parameters (how they are arranged): change MAXFN in DAT.FIT2 into a small number (e.g. 2), so the fitting will stop quickly. The list of data is written in file OUT.DAT. Here is an example: `1 PAGE`

```
SCAN,NKEY,COUNTS:CUU3A4-AN1 5 261

SCAN,NKEY,COUNTS:CUU3A4-AN2 6 522

[CHEN.OCT87.CUAL.U3]CUU3AA.XMU

FILE 5 AND FILE 6:
 INDEX  CONTENT                    INITIAL VALUE    FITTED VALUE
   1    D                OF  1      30.00000000      30.00000000
   2    SIGMA            OF  1      40.00000000      40.00000000
   3    DENSITY OF COMP  OF  2       0.77630001       0.77630001
   4    DENSITY OF COMP  OF  3    1306.19995117    1306.19995117
   5    D                OF  2     468.00000000     468.00000000
   6    SIGMA            OF  2      26.00000000      26.00000000
   7    DENSITY OF COMP  OF  1       0.02300000       0.02300000
        .
        .
        .
  16    DENSITY OF COMP  OF  2       0.06600000       0.06600000
  17    PHIZR                        0.00014000       0.00014000
  18    ANGPST                       0.00000100       0.00000100
  19    SMOOTH FACTOR                0.64999998       0.64999998
  20    NORMAL FACTOR                1.00000000       1.00000000
END OF FILE 5 AND FILE 6

SSQ= 4.8424389E-02 RSSQ= 2.5505185E-02
```

Determine which parameters you want to vary first, input their indices to DAT.TRK. Parameter 19 is related to the angle resolution of the experiment.

3. First fit a short range of data, by putting a large number for x_2 in DAT.INT (number of points to be cut from the end of the scan). Use IDP to determine how many points will lead to a short data range as shown in Fig.4.1.

Vary the parameters mentioned in fitting step 1 in Section 4.1. Fit one file at a time for this step, since the nomalization factor is different for scans at different energies. The results of fitting is written in file OUT.DAT.

4. Edit the input files to renew the parameters obained from 3, Change x_2 in DAT.INT back to a small number for a whole range fit. Fit two files together. Type file OUT.DAT for results.

5. The fitted parameters do not replace the old ones automatically. Therefore, to check the results of the fit, the new parameters have to be typed in by editing DAT.LIN or DAT.FIL, whichever is relevant. Change the index in DAT.FIL from 0 to 1 (no fitting), then run the program again. This time it won't fit, but simply calculates with the new parmameters. The output is written in a file DAT.DAT. Run program CAL, which converts the output into XMU format (both exprimental data and the fit). Then they can be viewed using IDP.

6. Recycle these procedures until satisfactory. Remember each time the new parameters have to be replaced manually.

Appendix D

ANALYSIS OF REFLECTIVITY EXAFS

As discussed in Section 5.3.2, the reflectivity EXAFS also suffers from the anomalous dispersion effect. The same model used for correcting the fluorescence EXAFS can be used to correct the reflectivity EXAFS. Here, reflEXAFS is defined as

$$\chi' = \frac{R_\mu - R_{\mu 0}}{step},$$

where R_μ is a constructed function based on the measured reflectivity R:

$$R_\mu = \frac{\mu_0}{R_0} R, \tag{D.1}$$

and R_0 is the calculated reflectivity (using the model obtained from angle data) as a function of energy, μ_0 is the calculated absorption coefficient step. Hence, if the calculation matches the data, R_μ should be a function containing the oscillations from R and a step from μ_0. The reflEXAFS obtained this way is different from the true EXAFS

$$\chi = \frac{\mu - \mu_0}{step}$$

in the following way:

$$\Delta R_\mu = \frac{dR_\mu}{d\mu} \Delta\mu$$

$$\begin{aligned}\chi' &= \frac{\Delta R_\mu}{step} \\ &= \frac{\Delta\mu}{step}\frac{dR_\mu}{d\mu} \\ &= \chi\frac{dR_\mu}{d\mu}.\end{aligned}$$

Therefore, χ' is divided by the correction factor $\frac{dR_\mu}{d\mu}$ to extract the real EXAFS.

Before constructing R_μ, one precaution is needed: The measured R data should be matched by the calculated R_0 both in the step size and the absolute value. Due to experimental conditions (air scattering, instrument response, e.g.), this can not always be satisfied. An additional procedure is used to adjust R_0 to match the data. There are two parameters, a constant shift and a normalization factor. This can easily be done by using the "SCALE" and "POINT" features in IDP, as well as a little algebra. By finding the right values for these two parameters, R_0 should reproduce the smooth background of R (by overplotting R_0 on R to check it).

Once a correct R_0 is obtained, construct R_μ according to Equation D.1. Run through the UW procedure listed in Appendix C. At the step for ADC, use the correction file for the reflectivity data (see Appendix A under ADC procedures).

Appendix E

A STORY

(Adapted from a Hammamatsu Newsletter)

A rabbit is typing his thesis when a fox walks by. "What are you doing, rabbit?" asks the fox. "I am typing my thesis." "What is it on?" "How a rabbit eats a fox." "I don't believe a word you said." "I'll show you my experiment." The rabbit takes the fox into the lab, then comes back alone to continue his typing. Now a wolf walks by. "What are you doing, rabbit?" asks the wolf. "I am typing my thesis on how a rabbit eats a wolf." "Never heard of it. Do you mean how a wolf eats a rabbit?" "No. I'll show you my experiment." The rabbit takes the wolf into the lab, then comes back alone to continue his typing. Now a tiger walks by. "What are you doing, rabbit?" asks the tiger. "I am typing my thesis on how a rabbit eats a tiger." "How dare you joke like that?" "I am not joking. I'll show you my experiment." The rabbit takes the tiger into the lab, then comes back alone to continue his typing.

The student dean, who has been watching all along, feels compelled to ask: "I am curious about your experiment." "Yes, Dean, I'll show you." They walk into the lab and see a well. At the bottom there are three pairs of skeletons — a fox, a wolf, and a tiger. But then they also see a lion sitting in it. Sighs the dean: "It doesn't matter what your thesis is, as long as you have the right advisor!"

Bibliography

[1] *Thin Films — Interdiffusion And Reactions*, J. M. Poate, K. N. Tu, and J. W. Mayer, Eds., John Wiley & Sons, New York (1978)

[2] L. F. Mondolfo, *Aluminum Alloys: Structures and Properties* Butterworth & Co. Ltd. Boston (1976)

[3] H. T. G. Hentzell, R. D. Thompson, and K. N. Tu, J. Appl. Phys. **54**, 6123 (1983)

[4] R. A. Hamm and J. M. Vandenberg, J. Appl. Phys. **56**, 293 (1984)

[5] H. S. Wildman and J. K. Howard, J. Vac. Sci. Technol., **12(1)** 75 (1975)

[6] J. W. Mayer and J. M. Poate, in *Thin Films — Interdiffusion And Reactions*, J. M. Poate, K. N. Tu, and J. W. Mayer, Eds., John Wiley & Sons, New York (1978)

[7] L. G. Parratt, Phys. Rev. **95**, 359 (1954)

[8] J. M. Andre, A. Maquet, and R. Barchewtiz, PHys. Rev. B **25** 5671 (1982)

[9] R. S. Becker, J. A. Golovchenko, and J. R. Patel, Phys. Rev. Lett. **50** 153 (1983)

[10] F. H. Cocks and R. Gettliffe, Mater. Lett. **3** 133 (1985)

[11] B. N. Thomas and S. A. Rice, J. Chem. Phys. **86** 3655 (1987)

[12] M. G. Le Boite, A. Traverse, L. Nevot, B. Pardo, and J. Corno, Nucl. Instrum. and Methods in Phys. Res. **B29** 653 (1987)

[13] A. Krol, C. J. Sher, and Y. H. Kao, Phys. Rev. B **38**, 8579 (1988)

[14] M. F. Toney and T. C. Huang, J. Mater. Rev. **3** 351 (1988)

[15] C. A. Lucas, P. D. Hatton, S. Bates, T. W. Ryan, S. Miles, and B. K. Tanner, J. Appl. Phys, **63** 1936 (1988)

[16] A. Braslau, M. Deutsch, P. S. Pershan, A. H. Weiss, J. Als-Nielsen and J. Bohr, Phys. Rev. Lett. **54** 114 (1985)

[17] S. K. Sinha, E. B. Sirota, S. Garoff, and H. B. Stanley, Phys. Rev. B **38** 2297 (1988)

[18] E. A. Stern and S. M. Heald, in *Handbook of Synchrotron Radiaton*, E. E. Koch, ed., **1b**, North-Holland, Amsterdam, 1983

[19] *EXAFS Spectroscopy, Techniques and Applicaltions*, Teo and Joy, ed., Plenum Press, New York, 1981

[20] Lytle, in *Advances in X-ray spectroscopy*, C. Bonnelle and C. Mande, Eds., Pergamon Press, 1982

[21] E. A. Stern, D. E. Sayers, and F. W. Lytle, Phys. Rev. B **11**, 4836 (1975)

[22] S. M. Heald, E. Keller, and E. A. Stern, Phys. Lett. **103A**, 155 (1984)

[23] R. Barchewitz, M. Cremonse-Visicato, and G. Onori, J. Phys. **C11** 4439 (1978)

[24] R. Fox and S. J. German, J. Phys. **C13** L249 (1980)

[25] L. Bosio, R. Cortes, A. Defrain and M. Froment, J. Electro-anal. Chem. **180** 265 (1984)

[26] G. Martens and P. Rabe, Phys. Status Solidi A **58** 415 (1980)

[27] J. A. del Cueto and N. J. Shevchik, J. Phys. C: Solid Stae PHys. **11** L833 (1978)

[28] D. T. Jiang, N. Alberding, A. J. Seary, and E. D. Crozier, Rev. Sci. Instrum. **59** 60 (1988)

[29] J. Stohr, L. I. Johansson, S. Brennan, M.. Hecht, and J. N. Miller, Phys. Rev. B **22** 4052 (1980)

[30] G. N. Greaves, N. T. Barrett, G. M. Antonini, F. R. Thornley, B. T. M. Willis, A. Steel, J. Am Chem. Soc. (to be published)

[31] J. M. Block, W. B. Yu, X. Yang, M. Ramanathan, P. A. Montano, and C. Capasso, Phys. Rev. Lett. **61** 2941 (1988)

[32] W. E. O'Grady, J. McBreen, G. Tourillon, E. Dartyge, A. Fontaine and K. I. Pandya, J. Chem. Phys. **85** 6732 (1986)

[33] Z. Tan, J. Budnick, and S. Heald, Rev. Sci. Instrum. (to be published)

[34] U. Bonse, I. Hartmann-Lotsch, H. Lotsch, in **EXAFS and Near Edge Structure**, A. Bianconi, L. Incoccia, and S. Stipcich, Eds., Spreinger-Verlag, Berlin, 1983

[35] P. Dreier, P. Rabe, W. Malzfeldt, and W. Niemann, in **EXAFS and Near Edge Structure**, A. Bianconi, L. Incoccia, and S. Stipcich, Eds., Spreinger-Verlag, Berlin, 1983

[36] B. Vidal and P. Vincent, Appl. Opt. **23** 1794 (1984)

[37] D. E. Sayers, S. M. Heald, M. A. Pick, J. I. Budnick, E. A. Stern, and J. Wong, Nucl. Instrum. and Methods **208** 631 (1983)

[38] Informal Report, Users Manual: Guide to the VUV and X-ray Beam Lines, N. F. Gmur and S. M. White-DePace, Eds., BNL40156, 1987

[39] E. A. Stern, W. T. Elam, B. A. Bunker, Qun-quan Lu, and S. M. Heald, in *Synchrotron Radiation Instrumentation* (Proc. of the Second Nat. Conf. on Sunchrotron Radiation Inst., Ithaca, New York), North-Holland, New York 1981

[40] K. H. Behrndt, in *Thin films, Paper Presented at A Seminar of The American Soc. for Metals*, Chapman & Hall, 1964

[41] S. M. Heald, J. M. Tranquada, and H. Chen, J. De Physique Coll. C8 **47** 825 (1986)

[42] S. M. Heald, J. M. Tranquada, D. O. Welch, and H. Chen, Mater. Res. Soc. Symp. Proc. **37** 437 (1985)

[43] V. Di Castro and G. Polzonetti, Surface Sci. **186** 383 (1987)

[44] S. M. Heald, H. Chen, and J. M. Tranquada, Phys. Rev. B **38** 1016 (1988)

[45] D. Gupta, D. R. Campbell, and P. S. Ho, in *Thin Films — Interdiffusion And Reactions*, J. M. Poate, K. N. Tu, and J. W. Mayer, Eds., John Wiley & Sons, New York 1978

[46] U. Gosele and K. N. Tu, J. Appl. Phys. **53** 3252 (1982)

[47] S. U. Campisano, G. Foti, E. Rimini, S. S. Lau, and J. W. Mayer, Phil. Mag. **31** 903 (1975)

[48] J. S. Solomon and S. R. Smith, J. Vac. Sci. Technol. A **5** 1809 (1987)

[49] W. H. Press, B. P. Flannery, S. A. Teukolsky, W. T. Vetterling, *Numerical Recipes: The Art of Scientific Computing*, Cambridge Univ. Press, Cambridge 1986

[50] D. DiMarzio, H. Chen, M. Ruckman, and S. Heald, J. Vac. Sci. (to be published)

[51] B. A. Bunker, PhD Thesis, University of Washington (1980)

[52] S. M Heald and J. M. Tranquada, in *Physical Methods Of Chemistry*, B. W. Rossiter, J. F. Hamilton, and R. C. Baetzold, Eds., **5**, John Wiley & Sons, Inc., (to be published)

[53] S. J. Gurman, H. Binsted, and I. Ross, J. Phys. **C 17** 143 (1984).

[54] R. W. James, *The Optical Principles of the Diffraction of X-rays*, B. Bell and Sons, London 1958

[55] H. Chen and S. M. Heald, Physica B (Proc. of 5th Int. Conf. on X-ray Absorption Fine Structure, Seattle, Washington 1988), in press

[56] C. A. Chang, J. Appl. Phys. **52** 4620 (1981)

[57] *Ion Beam Handbook for Material Analysis*, J. W. Mayer and E. Rimini, Eds., Acedemic Press, New York 1977

[58] M. C. Madden, Thin Solid Films, **154** 43 (1987)

[59] J. E. E. Baglin and J. M. Poate, in *Thin Films — Interdiffusion And Reactions*, J. M. Poate, K. N. Tu, and J. W. Mayer, Eds., John Wiley & Sons, New York 1978

[60] H. Asonen, C. J. Barnes, A. Salokatue, and M. Pessa, Surface Sci. **152/153** 262 (1985)

[61] N. V. Smith and F. J. Himpsel, in *Handbook of Synchrotron Radiaton*, E. E. Koch, ed., **1b**, North-Holland, Amsterdam, 1983

[62] X. A. Zhao, H. Y. Yang, E. Ma, and M. A. Nicolet, J. Appl. Phys **62** 1821 (1987)

[63] K. N. Tu, Ann. Rev. Mater. Sci. **15** 147 (1985)

[64] V. DiCastro and G. Polzonetti, Surface Sci. **189/190** 1085 (1987)

[65] M. J. Verkerk and G. J. Van der Kolk, J. Vac. Sci. A **4** 3101 (1986)

[66] D. A. Fisher, G. G. Cohen, and N. J. Shevchik, J. Phys. F: Metal Phys. **10** L139 (1980)

[67] S. Westman, Acta Chem. Scand. **19** 1415 (1965)

[68] P. Villars and L. D. Calvert, Pearson's Handbook of Crystallographic Data for Intermetallic Phases, American Society for Metals, 1985

[69] International Tables for X-ray Crystallography, N. F. M. Henry and K. Lonsdale, Eds., The Kynoch Press, Birmingham 1969

[70] Program STRUC in the UW software pakage.

[71] G. Martens, P. Rabe, N Schwentner, and A. Werner, J. Phys. C: Solid State Phys. **11** 3125 (1978)

[72] W. T. Elam, J. P. Kirkland, R. A. Neiser, and P. D. Wolf, Phy. Rev. B **38** 26 (1988)

[73] P. Bandyopadhyay and B. A. Bunker, Physica B (Proc. of 5th Int. Conf. on X-ray Absorption Fine Structure, Seattle, Washington 1988), in press